STARS

Electronic Theses and Dissertations, 2004-2019

2018

Generation and Characterization of Isolated Attosecond Pulse in the Soft X-ray Regime

Jie Li
University of Central Florida

University of Central Florida

STARS
Showcase of Text, Archives, Research & Scholarship

GENERATION AND CHARACTERIZATION OF ISOLATED ATTOSECOND PULSE IN
THE SOFT X-RAY REGIME

by

JIE LI
B.S., University of Science and Technology of China, 2012

A dissertation submitted in partial fulfillment of the requirements
for the degree of Doctor of Philosophy
in the College of Optics and Photonics
at the University of Central Florida
Orlando, Florida

Spring Term
2018

Major Professor: Zenghu Chan

ABSTRACT

The observation of any atomic and molecular dynamics requires a probe that has a timescale comparable to the dynamics itself. Ever since the invention of laser, the temporal duration of the laser pulse has been incrementally reduced from several nanoseconds to just attoseconds. Picosecond and femtosecond laser pulses have been widely used to study molecular rotation and vibration.

In 2001, the first single isolated attosecond pulse (1 attosecond = 10^{-18} seconds.) was demonstrated. Since this breakthrough, "attoscience" has become a hot topic in ultrafast physics. Attosecond pulses typically have span between EUV to X-ray photon energies and sub-femtosecond pulse duration. It becomes an ideal tool for experimentalists to study ultrafast electron dynamics in atoms, molecules and condensed matter.

The conventional scheme for generating attosecond pulses is focusing an intense femtosecond laser pulse into inert gases. The bound electrons are ionized into continuum through tunneling ionization under the strong electrical field. After ionization, the free electron will be accelerated by the laser field away from the parent ion and then recombined with its parent ion and releases its kinetic energy as a photon burst that lasts for a few hundred attoseconds. According to the classical "three-step model", high order harmonic will have a higher cutoff photon energy when driven by a longer wavelength laser field. Compared to Ti:sapphire lasers center at a wavelength of 800 nm, an optical parametric amplifier could offer a broad bandwidth at infrared range, which could support few cycle pulses for driving high harmonic generation in the X-ray spectrum range.

In this work, an optical parametric chirped-pulse amplification system was developed to deliver CEP-stable 3-mJ, 12-fs pulses centered at 1.7 micron. We implement a chirped-pump technique to phase match the board parametric amplification bandwidth with high conversion efficiency. Using such a laser source, isolated attosecond pulses with photon exceeding 300 eV are achieved by applying the polarization gating technique at 1.7 micron. The intrinsic positive chirp of the attosecond pulses is measured by the attosecond streak camera and retrieved with our PROOF technique. Sn metal filters with negative dispersion were chosen to compensate the intrinsic attochirp. As a result, isolated 53-attosecond soft x-ray pulses are achieved. Such water window attosecond source will be a powerful tool for studying charge distribution/migration in bio-molecules and will bring opportunities to study high field physics or attochemistry.

ACKNOWLEDGEMENTS

Zeldovich, Dr. Eric Van Stryland, Dr. Bo Chen and Dr. Michael Chini for being my committee members.

I also would like to thank my girlfriend Xiaoyun Li for her support and encouragement. Meeting her in Orlando was the most important and wonderful moment in my life.

Finally, I want to thank my parents: Xiaoping Li and Fang Li. I have not been spending much time with them since high school and I have been spending even less time with them when I was pursuing a higher degree. However, they have always supported and encouraged me as if they were never far from me. The past several years have not been an easy journey. My parents are truly my spiritual support. There are no words to convey how important they are and how much I love them.

TABLE OF CONTENTS

LIST OF FIGURES

LIST OF TABLES

CHAPTER 1 - INTRODUCTION

Since the laser was invented in year 1960 [1, 2], people have, for the first time, access to a stable electromagnetic source, which is coherent in both space and time. The first laser pulses have a pulse duration of 10 μs. It was not long later that scientist invented Q-switch [3] and mode locking techniques[4] which have shorted the pulse duration to nanoseconds (10^{-9} s), picoseconds (10^{-12} s) and even femtoseconds (10^{-15} s). Various laser amplification technologies, especially the chirped pulse amplification technique[5], allowed one to achieve high power short pulse without damaging the optics duration amplification process.

The improvement in laser technologies have given people new tools for scientific study, especially in the field of ultrafast science. As the laser pulse durations get shorter in time, one can use such source to excited or probe dynamics that occur on a comparable time scale. Figure 1.1 shows the typical time scale for certain atomic and molecular dynamics [6-9].
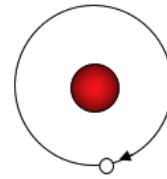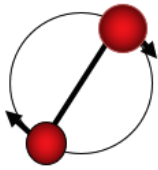
Figure 1.1 Time scales for different dynamics in atoms and molecules. (a) Molecule rotational motion period is in the time scale of picoseconds. (b) Molecule vibration period is in the time scale of femtosecond. (c) Electron dynamics inside an atom is in an even shorter time scale of attosecond.

Unlike picosecond or femtosecond laser pulses which are generated using mode-locking technique in optical gain media. The generation of attosecond pulses is based on an extreme nonlinear process. The observation of the first attosecond pulses was in 2001[10], when researchers detected a train of 250 as pulses resulting from the superposition of a few adjacent high harmonics. Since then, attosecond science has progressed substantially. To produce attosecond pulses, a typical driving laser intensity of 10^{14} W/cm^2 is required for interaction with gas media and attoseond pulses could be achieved through a process called high harmonic generation (HHG)[11]. For the past decade. Ti:sapphire lasers centered at 800 nm with femtoseconds pulse duration were widely used as the driving source for HHG and attosecond science[5, 12]. However, the HHG process will repeat itself every half-optical cycle, and hence,

a train of attosecond pulses will be generated when using few-cycle driving laser. From

application point of view, to reach attosecond time resolution, an isolated attosecond pulse is

preferred for experiments, such as attosecond transient absorption using pump-probe technique.

This leads on to another topic of isolating a single attosecond from each laser driving pulse.

Several attosecond gating methods have been proposed and proven reliable [13-19].

In this dissertation, Chapter 2 introduces the HHG principle and compares different

gating methods for generating an isolated attosecond pulse. Chapter 3 introduces the IR OPCPA

laser system in iFAST lab. Chapter 4 focus on the polarization gating (PG) technique we use

with 1.7 μm laser to generate soft X-ray attoseond pulses. Chapter 5 introduces the attosecond

streak camera setup for characterizing the isolated attosecond pulse and the PROOF method for

retrieving the attosecond pulse. Finally, in Chapter 6, a summary of the entire thesis is given and

an outlook for future progress is discussed.

CHAPTER 2 - HIGH HARMONIC GENERATION

2.1 The principle of high harmonic generation (HHG)

The first high harmonics were observed in the late 1980s [20, 21]. By focusing a 1067 nm 50 picosecond laser into an argon gas target, odd-ordered harmonics of the fundamental 1067 nm were observed. It was not until 1993 that the well-known "three step model" was proposed by Corkum [11]. This model gives a semi-classical picture of how the HHG results from the recombination of a photo-ionized electron with its parent ion.

In order to generate high-order harmonics, an intense laser pulse is first focused into a noble gas. When the driving electric field reaches one of its maximum amplitudes, the Coulomb barrier of the laser-dressed parent atom is greatly reduced. (Figure 2.1) As a result, a bound electron is able to tunnel-ionize through the potential barrier I_p and reach the continuum stage. This process – ionization – is the first step of the three-step model, and is typically treated using quantum mechanical methods.
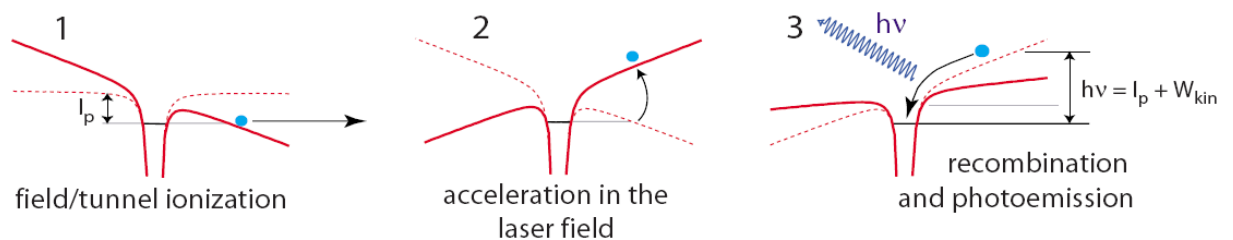
Figure 2.1 The Three Step Model of HHG

To determine if the bound electron is ionized preferably through perturbative multiphoton ionization process or tunnel ionization proess, the Keldysh parameter γ [22] was introduced to distinguish the two process, and is defined as:

$$\gamma = \sqrt{\frac{I_p}{2U_p}} \tag{2.1}$$

Where I_p is the ionization potential of the target atoms, U_p is the ponderomotive energy that indicate the average quiver energy of free electron in a laser field:

$$U_p = \frac{e^2 E_0^2}{4m_e \omega^2} \tag{2.2}$$

Where e and m_e are the electron charge and mass, E_0 and ω are the driving laser amplitude and angular frequency. When the laser intensity is small ($< 10^{13}$ W/cm^2), $\gamma \gg 1$ and multi-photon ionization is dominant. When the laser intensity increases, $\gamma \ll 1$ and tunnel ionization process starts to be dominant. For a Ti:sapphire laser centered at 800 nm and a noble gas target with $I_p =$ 10~20 eV, a focus intensity of 10^{14} W/cm^2 will ensure that the tunnel ionization is the dominant process.
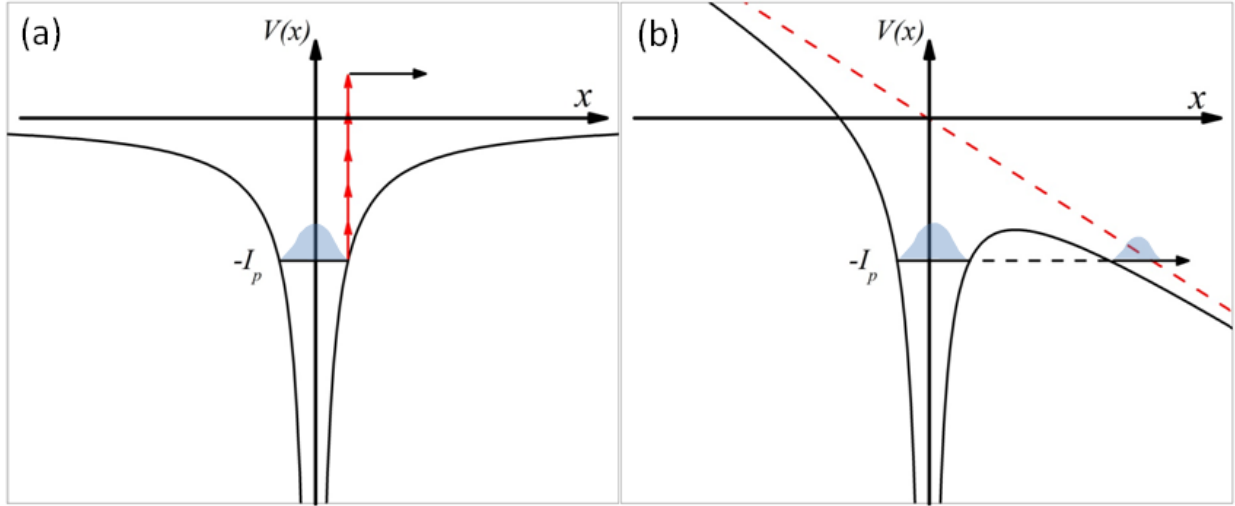
Figure 2.2 Atomic ionization under different laser intensity. (a) Multi-photon ionization: at a moderate laser intensity. The atomic Coulomb potential is unperturbed by the external electrical field. The ground-state electron is ionized by absorb multiple photons. (b) Tunnel ionization: the external electric field is strong enough to affect the Coulomb potential and potential barrier is formed for tunneling effect.

Once the electron tunnels out of the binding potential, the Coulomb force from the parent ion can be neglected, and the electron can be treated as a free particle. The motion of the electron is modelled classically using Newton's laws of motion:

$$a(t) = \ddot{x}(t) = \frac{eE_0}{m_e} \cos(\omega t) \qquad (2.3)$$

$$v(t) = \dot{x}(t) = \frac{eE_0}{m_e \omega} [\sin(\omega t) - \sin(\omega t_0)] \qquad (2.4)$$

$$x(t) = \frac{eE_o}{m_e \omega^2} [[\cos(\omega t) - \cos(\omega t_0)] + \omega \sin(\omega t_0)(t - t_0)] \qquad (2.5)$$

Where t_0 is the birth time of the electron.

One can simply treat the electron as a point-like particle under the influence of a strong laser field. The electron is initially accelerated away from the atom as the electric field remains pointing in the same direction during ionization. After roughly one quarter of a laser cycle, the diving pulse's electric field changes sign and the electron may accelerate back towards its parent ion. Whether or not the electron could recombine with its parent ion depends on the time of ionization. The recombination event can be solved by using $x(t) = 0$ for equation 2.5. Therefore, for a given ionization time t_0 ($0 < t_0 < 0.25\ T_0$, T_0 is the laser cycle), there is a corresponding recombination t. The relationship of t and t_0 do not have an analytical expression but can be fitted with:

$$\sin(\omega t_0) = \cos\left[\frac{\pi}{2}\sin\left(\frac{1}{3}\omega t - \frac{\pi}{6}\right)\right] \qquad (\,2.6\,)$$

The fitting result is plotted in Figure 2.3 (a).
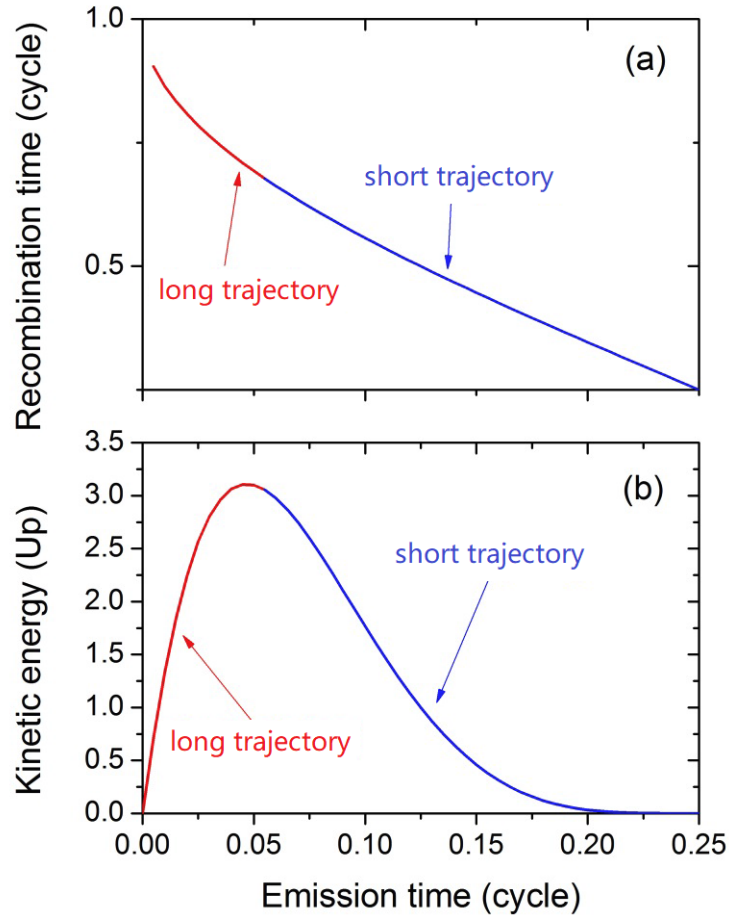
Figure 2.3 (a) Relationship between electron emission time and recombination time. (b) Final kinetic energy of recombined electron as a function of the emission time.

The emitted HHG photon energy, typically in the extreme ultra violet regime (XUV),

equals to the sum of ionization potential and returning kinetic energy:

$$hv_{XUV}(t) = I_p + \frac{1}{2}m_e v^2(t) = I_p + 2U_p \left[\sin(\omega t) - \sin(\omega t_0)\right]^2 \qquad (2.7)$$

Since the relationship between t and t_0 is known, the relationship between recombination energy and emission time can be calculated. The result is plotted in Figure 2.3 (b). Notice that for a certain kinetic energy at recombination, there are two corresponding emission times [23, 24], the electron emitted during $0 < t_0 < 0.05\ T_0$ will recombine during $T_0 > t > 0.7\ T_0$. This branch is called the "long trajectory" because the electron will travel further away from its parent ion compared to the "short trajectory", where the electron was emitted during $0.05\ T_0 < t_0 < 0.25\ T_0$ and recombine during $0.7\ T_0 > t > 0.25\ T_0$. From Figure 2.3 (b), the highest return energy is $3.17U_p$, which corresponds to a emission time $t_0 = 0.05\ T_0$ and a recombination time $t = 0.7\ T_0$. The highest HHG cutoff photon energy is:

$$h\nu_{XUV\_cutoff} = I_p + 3.17U_p \tag{2.8}$$

where the ponderomotive energy U_p can be rewritten as:

$$U_p[\text{eV}] = 9.33 \times 10^{-14} I_0 \lambda_0^2 \tag{2.9}$$

where I_0 is the laser intensity in W/cm^2 and λ_0 is the driving filed wavelength in μm. Equation 2.8 provides a very straight forward calculation of the cutoff photon energy. For example, using 800 nm Ti:sapphire with a focus intensity of 1×10^{15} W/cm^2 in the neon gas ($I_p = 21.5$ eV), the corresponding cutoff photon energy equals to 211 eV.

Since the returning electron kinetic energy various with the recombination time, the emitted attosecond pulse has an intrinsic chirp called attochirp [25]. Figure 2.4 shows the relation

between returned kinetic energy versus recombination time base on equation 2.6 and equation

2.7.
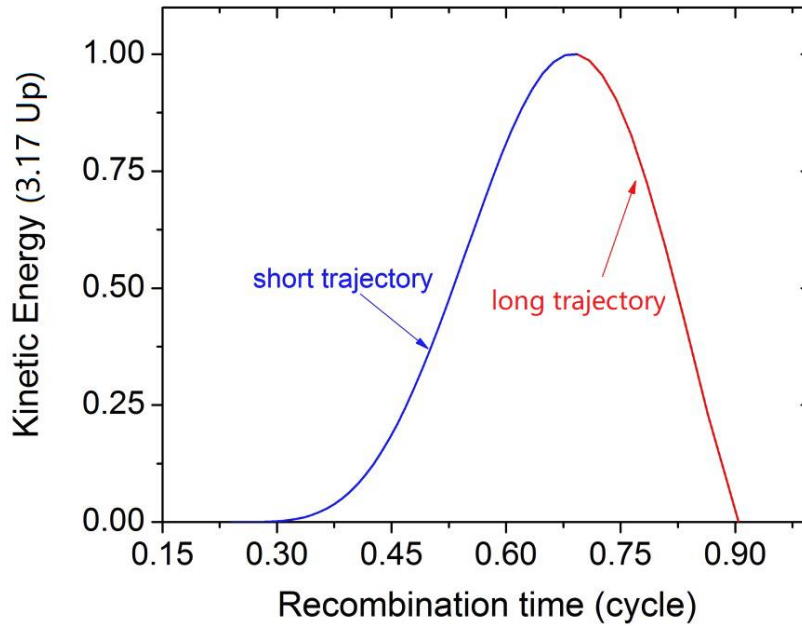
Figure 2.4 Returning electron kinetic energy versus electron recombination time. The XUV emission from the short trajectory have an increasing photon energy by time.

Notice that in the short trajectory has the kinetic energy of the electron increases with

recombination time, which indicates that the emitted XUV pulse have lower photon energy at the

leading edge and higher photon energy at the trailing edge, creating a positively chirped XUV

pulse. The condition is reversed for the long trajectory emission. The long and short trajectory

photons have different divergence angles and phase matching conditions [23, 24] and the long

trajectory emission can often be suppressed in experiment. This generally leaves the short

trajectory photon emissions to be the dominant one and often resulting in an attosecond pulse with positive chirp.

Figure 2.5 show the intrinsic attochirp in terms of group delay dispersion (GDD, in the unit of as^2) from the short trajectory using 800 nm driving laser with a focus intensity of 1×10^{15} W/cm^2 inside neon gas target. The positive attochirp will lead to a non-transform-limited attosecond pulses, limiting the temporal resolution for applications. Fortunately, this positive attochirp can be compensated using thin metal filters with a negative dispersion [26]. This will be discussed in detail in Chapter 5.
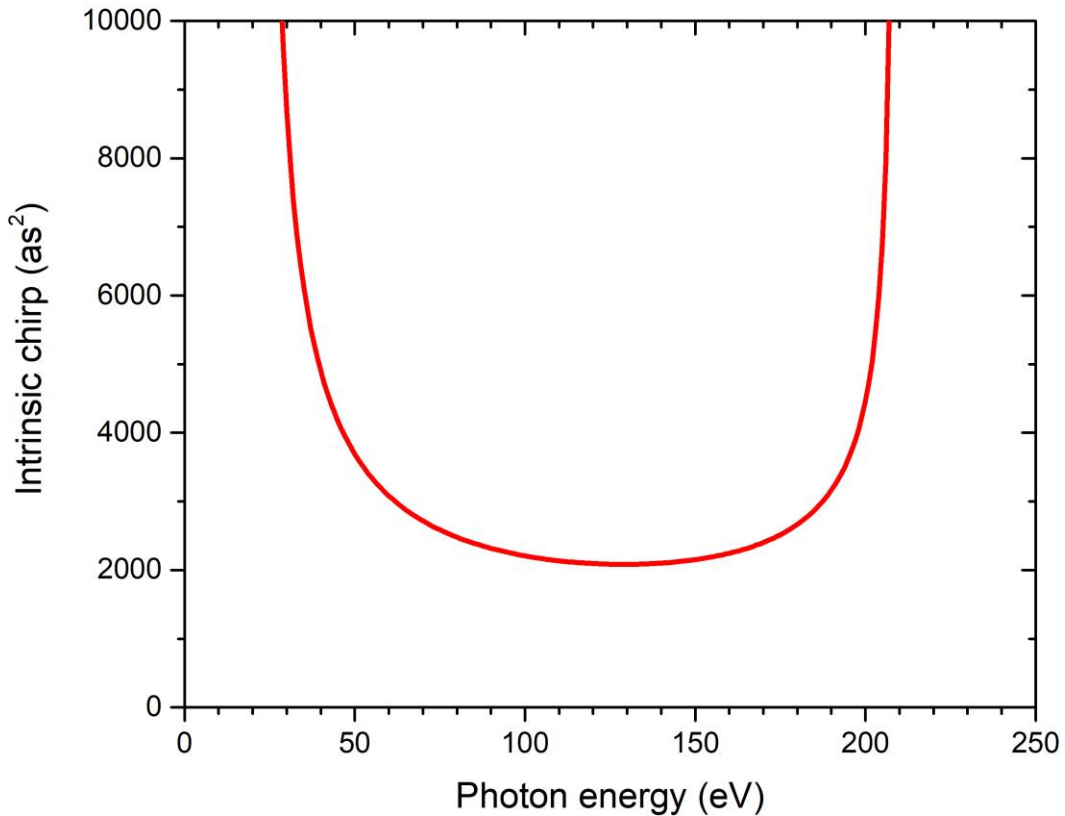
Figure 2.5 The intrinsic attochirp for the short trajectory emission. The driving field wavelength is 800 nm with an interaction intensity of 1×10^{15} W/cm^2 in neon gas target.

2.2 Isolated attosecond pulses

During each laser cycle, the three-step process is twice repeated. This means a typical linearly polarized laser pulse generates a train of attosecond pulses with half-cycle spacing. (Figure 2.6) The interference between each attosecond pulse will lead to spectrum modulation in the frequency domain.
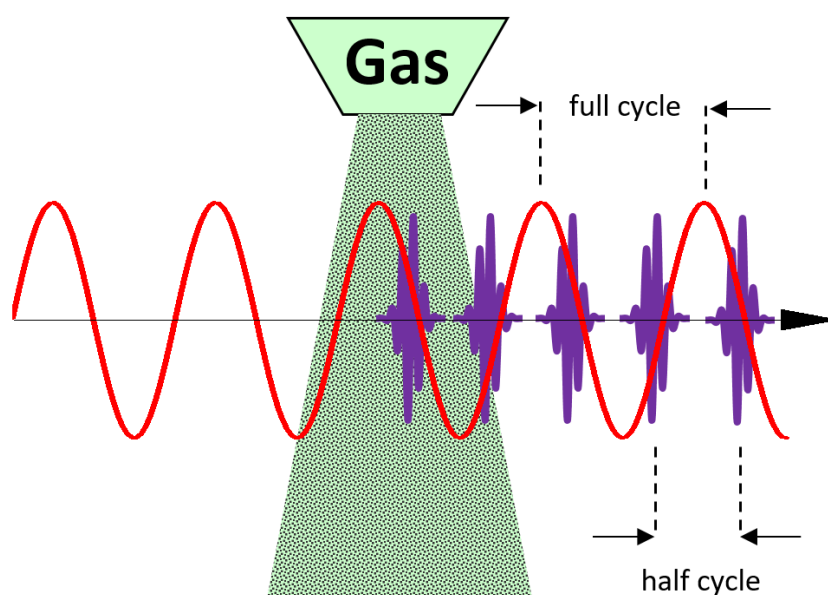
Figure 2.6 Generation of an attosecond pulse train with a linearly polarized field.

An attosecond pulse train is not very useful when compared to an isolated attosecond pulses (IAP). To achieve IAP, the traditional method is to limit the occurrence of the three-step process to only once per driving pulse. The alternative method is to isolate the attosecond pulse train in space. The first method relies on introducing a narrow time window, or a time "gate", within the driving field pulse where a single attosecond pulse is generated. Such methods are thus categorized as attosecond gating. A schematic illustration of different methods is presented in Figure 2.7.

12

2.2.1 Amplitude gating

The most straightforward gating method is reducing the driving pulse duration to few-cycles. Thus, the strongest half-cycle of the driving pulse will produce highest energy photons through the three-step recombination process where they will contribute to the highest energy part of the HHG spectrum. However, weaker half-cycle of the driving field will still result in the emission of HHG with lower photon energy and thus produce an attosecond pulse train, albeit with lower cutoff energy than the attosecond pulse produced by the strongest laser half-cycle. Harmonic peaks will still be observed at the lower energy side of the harmonic spectrum. Proper filters are needed to select the higher energy spectrum that is produced within the strongest half-cycle of the driving pulse.

With the amplitude gating method, 80 as pulses were reported [13] in 2008 using a single-cycle driving pulse. The advantage of amplitude gating is the high usage of the driving pulse energy to produce the wide bandwidth harmonic spectrum. The drawback is only the cutoff spectrum region contributes to the IAP and producing a single-cycle pulse is also a technically difficult challenge. Octave spanning spectrum is required as well as good phase compensation over the entire spectrum [27]. To reach a high energy single-cycle driving pulse, octave span spectrum is usually divided into different section for amplification. This will further complicate the laser system design.

A schematic illustration of amplitude gating is shown in Figure 2.7 (a). The HHG spectrum contributed by each half-cycle is compared in Figure 2.8 (e). Only the strongest half-cycle in the peak of the driving field contribute to the cutoff spectrum region highlighted in yellow in Figure 2.7 (e).

13

2.2.2 Ionization gating

Similar to the amplitude gating, the ionization gating can be achieved by directly focus a linearly polarized pulse into the target gas. With a high peak intensity, the gas media is usually full ionized within the leading edge of the pulse [28]. The highest cutoff photon energy is achieved before or at the middle strong cycle of pulse, leaves the result of the pulse useless. Like amplitude gating, the ionization gating also produce multiple HHG pulses, with a strongest one that has the highest cutoff. Thus, proper filter is also need to isolate the cutoff spectrum region. A schematic illustration of ionization gating is showed in Figure 2.7 (b). Each half-cycle contribute to the total HHG yield until the target gas is fully ionized.
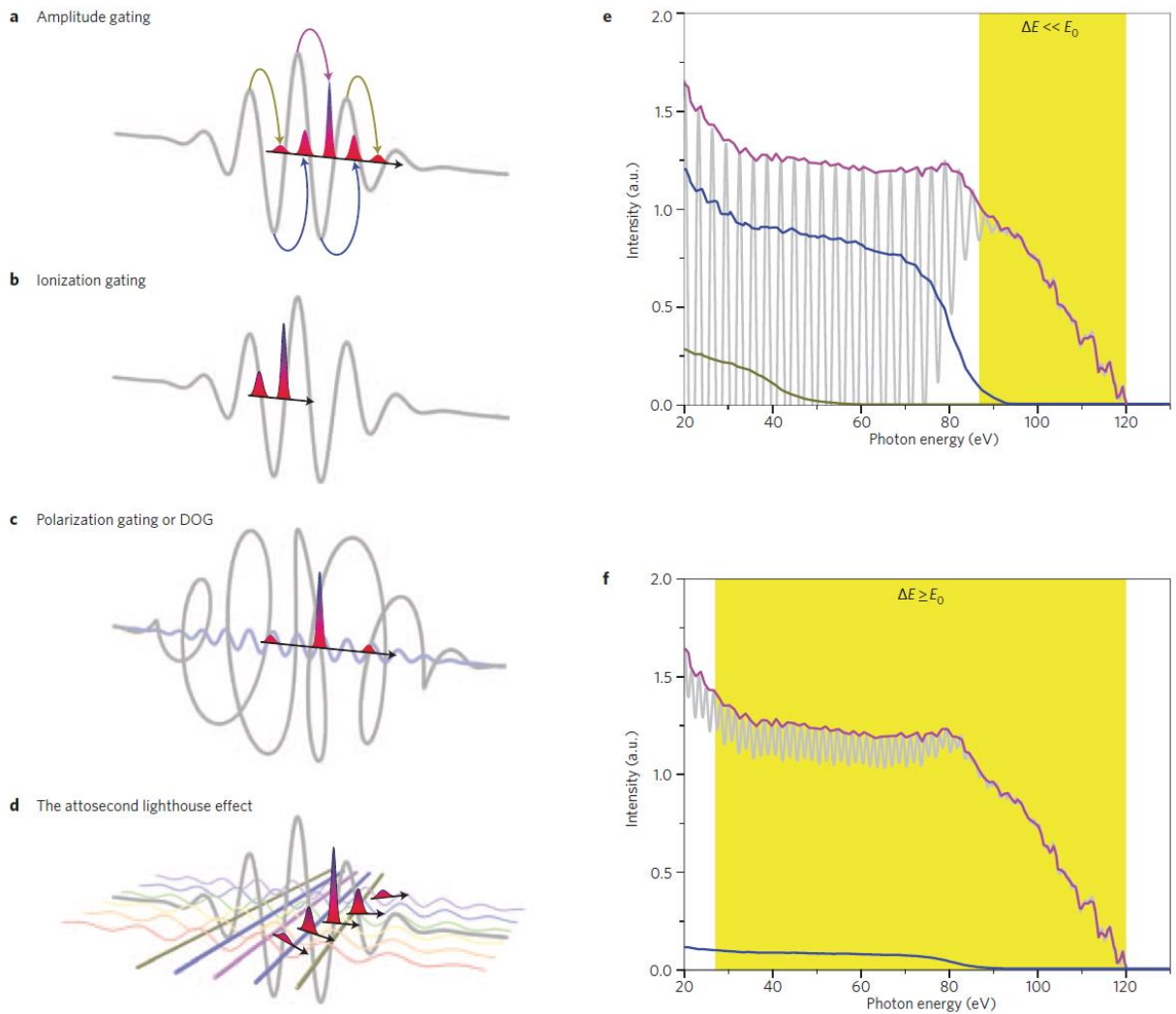
Figure 2.7 (a) Amplitude gating; (b) ionization gating; (c) polarization gating or DOG; (d) the attosecond lighthouse effect. (e),(f) Only the cutoff spectrum is usable with amplitude gating or ionization gating (e); polarization gating, DOG and the attosecond lighthouse effect can produce ultrabroadband attosecond pulses with a continuum spectrum covering the plateau and cutoff (f). The magenta, blue, and green lines indicate the contributions of different half cycles to the total attosecond spectrum. Figure adopted from ref [29]

15

2.2.3 Polarization gating

Polarization gating [14, 30-37] restricts attosecond pulse generation to a single half-cycle of the laser field by manipulating the second step of the three-step process. In a linearly polarized field, the free electron accelerated forward and backward in the same path and recombined with its parent ion. If a circularly-polarized electric field is used to accelerate the electrons, then a transverse displacement will appear and the electron is driven away from its parent ion. As a result, the recombination is impossible or probabilistically reduced substantially. Therefore, the HHG yield shows a strong dependence on the driving field ellipticity [38]. Since the field ellipticity would affect the HHG yield, it can be used to limit the HHG birth to only a half-cycle of the driving. The polarization gating is based on this idea. Figure 2.7 (c) shows an electric field with time-varying ellipticity. The leading and trailing part of the electric field is elliptically polarized. Only the middle part is close to linearly polarized. Therefore, HHG recombination process happens only in the middle of the pulse. Figure 2.8 shows a collinear scheme for generating electric field with time-varying ellipticity.
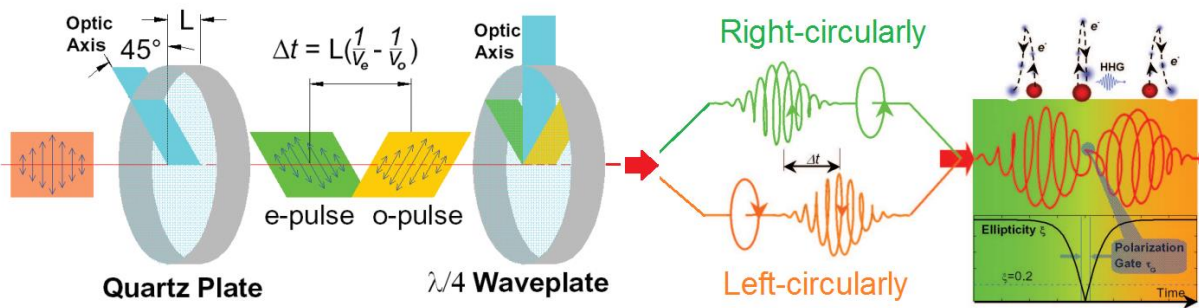
Figure 2.8 The collinear scheme for generating electric field with time-varying ellipticity from a linearly polarized field. Figure adopt from ref [39].

To fully understand the gating optics in Figure 2.8, it is necessary to give a full analytical explanation. Assume the incoming linearly polarized field has a Gaussian shape:

$$E(t) = E_0 e^{-2In(2)\frac{(t)^2}{\tau_p^2}} cos(\omega_0 t + \varphi_{CE})$$ (2.10)

Where E_0 is the peak electric field, τ_p is the FWHM pulse duration, ω_0 is the center frequency and φ_{CE} is the carrier envelope phase (CEP). After propagating through the first quartz plate (set at 45^0 with respect to the input field polarization), the refractive index difference between the e- and o-axis will introduce a group delay T_{Gd} between the e- and o-pulse:

$$T_{Gd} = L(\frac{1}{v_{Go}} - \frac{1}{v_{Ge}})$$ (2.11)

Where v_{Ge} and v_{Go} is the group velocity of the e- and o-pulse and L is the thickness of the quartz plate. To ensure the driving field is parallel to the input field polarization, the thickness of the first quartz plate should introduce integer cycle of phase delay:

$$T_{Pd} = L \left(\frac{1}{v_{Po}} - \frac{1}{v_{Pe}}\right) = T_0, 2T_0, 3T_0 ...$$ (2.12)

where T_0 equals to one optical cycle. v_{Pe} and v_{Po} are the phase velocity of the e- and o-ray. Typically, the first wave plate is thin in thickness to introduce only few cycle delay. The relative difference between T_{Pd} and T_{Gd} are usually small enough to be neglected. The e- and o-field after the first quartz plate can be expressed as:

$$E_o(t) = \frac{\sqrt{2}}{2} E_0 \left[\left(e^{-2In(2)\frac{(t-\frac{T_d}{2})^2}{\tau_p^2}} \right) cos(\omega_0 t + \varphi_{CE}) \right] \qquad (2.13)$$

$$E_e(t) = \frac{\sqrt{2}}{2} E_0 \left[\left(e^{-2In(2)\frac{(t+\frac{T_d}{2})^2}{\tau_p^2}} \right) cos(\omega_0 t + \varphi_{CE}) \right] \qquad (2.14)$$

Where $E_o(t)$ and $E_e(t)$ are the o- and e-field, they have the same φ_{CE} because an integer phase

delay is introduced. The group delay dispersion difference between o- and e-field is small

enough to be neglected. Therefore, the second order dispersion effect can be neglected. After the

zero-order quarter wave plate, the o- and e-field becomes a circle polarized filed and the final

electric field can be expressed as:

$$\vec{E}(t) = E_{drive}(t)\vec{x} + E_{gate}(t)\vec{y} \qquad (2.15)$$

Where $\vec{x}$ and $\vec{y}$ are the unit vectors that are perpendicular to the propagation direction. And $\vec{x}$ is

parallel to the polarization direction of the incident pulse. The driving and gating filed is given

by:

$$E_{drive}(t) = E_0 \left[\left(e^{-2In(2)\frac{(t+\frac{T_d}{2})^2}{\tau_p^2}} + e^{-2In(2)\frac{(t-\frac{T_d}{2})^2}{\tau_p^2}} \right) cos(\omega_0 t + \varphi_{CE}) \right] \qquad (2.16)$$

$$E_{gate}(t) = E_0 \left[\left(e^{-2In(2)\frac{(t+\frac{T_d}{2})^2}{\tau_p^2}} - e^{-2In(2)\frac{(t-\frac{T_d}{2})^2}{\tau_p^2}} \right) sin(\omega_0 t + \varphi_{CE}) \right] \qquad (2.17)$$

Figure 2.9 shows the polarization gated electric field. The parameter is τ_p=7 fs, T_d=11.76

fs, ω_0 corresponds to 800 nm and φ_{CE}=0 rad. The red line is the driving field for generated

HHG, the green line is the gating field to introduce non-zero elliptically to suppress the HHG

wield. Notice that the gating field drops to zero at the middle, where the total field is nearly

linearly polarized and thus providing a time window for effective HHG emisson.
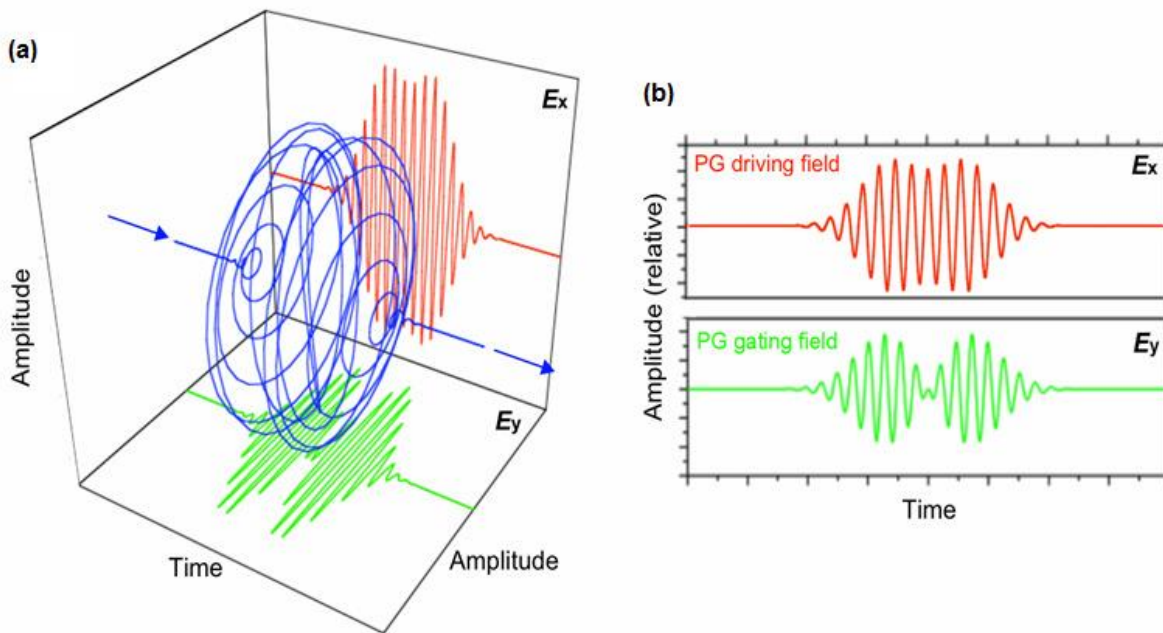
Figure 2.9 The final electric field (blue) for polarization gating in 3D. The red line is the driving field for generated HHG, the greed line is the gating field for introduce non-zero elliptically to suppress the HHG wield.

To qualitative characterize the gating effect caused by an elliptical field, the time-dependent filed

ellipticity is defined as:

$$\xi(t) = \frac{|E_{gate}|}{|E_{drive}|} = \left| \frac{1-e^{\frac{-4In(2)T_d t}{\tau_p^2}}}{1+e^{\frac{-4In(2)T_d t}{\tau_p^2}}} \right| \qquad (2.18)$$

19

For the middle portion where the e- and o-field are well overlapped ($4 In(2)T_d t\tau_p^{-2} \ll 1$), the ellipticity can be approximated by:

$$\xi(t) = \left| 2In(2)\frac{T_d}{\tau_p^2}t \right|$$ (2.19)

Let ξ_{th} be the threshold ellipticity where the harmonic yield can be effectively suppressed (for example drop by 90%). For an 800 nm driving field, the required threshold ellipticity is $\xi_{th} = 0.2$ for the suppression 90% of the HHG yield [40]. Therefore, a finite time window δt_G can be defined such that inside this time window, $-\frac{1}{2}\delta t_G < t < \frac{1}{2}\delta t_G$, the ellipticity of the total field is smaller than the threshold ellipticity ξ_{th} so that HHG can be effectively generated. The time window δt_G is named as polarization gating width[32]:

$$\delta t_G = \frac{\xi_{th}}{In(2)}\frac{\tau_p^2}{T_d}$$ (2.20)

Usually, the polarization gating width should be less that half-cycle $\delta t_G < \frac{1}{2}T_0$ for the effective isolation of the attosecond pulse. Therefore, the group delay T_d should be chosen carefully based on the input pulse duration τ_p.

2.2.4 Two color gating

The ionization rate of bound electrons depends on the driving field strength. By adding an additional field to the main driving field, the ionization rate in each half-cycle will be modulated since the tunnel ionization process depends nonlinearly on the field strength. A special case is when the wavelength of second field is only half of the main driving field with

20

their relative phase being $\varphi_{12} = 0\ or\ \pi$ (Figure 2.10 (a)). The total field is the linear superposition of the two fields (Figure 2.10 (b) purple line), which is no longer symmetric. The tunnel ionization process is suppressed where the driving field peak is weakened at the negative amplitude. Therefore, the harmonic generation reduced from every half cycle to every full cycle of the driving filed. Notice that two color gating itself could not produce isolated attosecond pulse. It has to work with other gating techniques to produce isolated attosecond pulses.
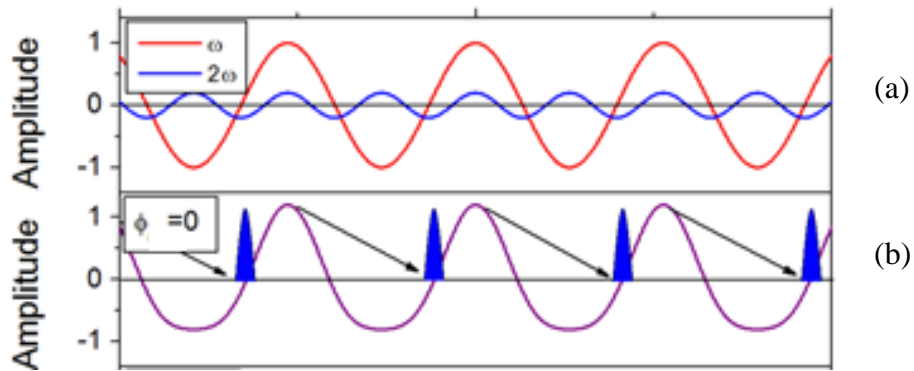
Figure 2.10 Two color gating

2.2.5 Double optical gating

The double optical gating (DOG) [15-17] scheme comes from the combination of polarization gating (PG) and two color gating. The PG gate width (equation 2.20) needs to be less than half optical cycle to isolate an attosecond pulse because the HHG process repeats every half optical cycle. By adding a *2ω* field, the two color gating could reduce the harmonic generation to every optical cycle, which will loosen the requirement of gate width from half optical cycle to one optical cycle. This is the basic idea of DOG.

21
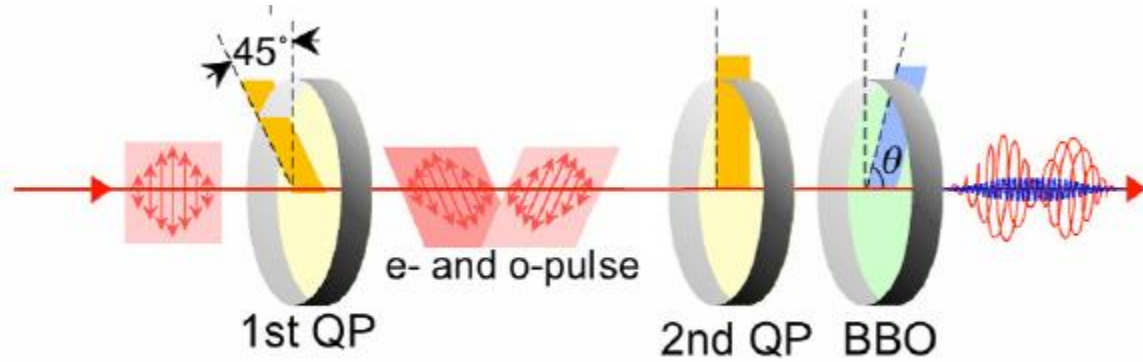
Figure 2.11 Collinear setup for double optical gating

Figure 2.11 shows a collinear setup for DOG. The difference between DOG and polarization gating (PG) is the quarter wave plate in PG is changed to a combination of a second quartz plate (QP) and a thin BBO crystal. Since the second QP and BBO are birefringence crystals, their optical axis orientation and thickness are design that their total birefringence effects equals to a zero-order quarter wave plate like the case of PG. The BBO crystal can also generate a second harmonics field whose polarization direction is same as the driving field in PG case. The BBO crystal needs to be thick enough (~ 100 µm) for up converting adequate second harmonics flux for two-color gating to work. However, a 100 µm BBO will typically introduce more than quarter cycle of phase delay between e- and o-field. That is way a second birefringence plate (2nd QP in this case) is required to counteract the BBO birefringence effect so that the total phase delay (introduced by 2nd QP + BBO) between e- and o-field equals to a quarter optical cycle.

To give a more intuitive comparison between DOG and PG, the electric field components are plotted in Figure 2.12. The major difference is DOG has a weak second harmonic field that was added to the PG driving field to form the DOG driving field (red line), which is similar to the two-color gating technique. The gating field (green) is polarized in the orthogonal direction to produce elliptical field component for suppress the HHG except the center. The advantage of DOG over PG is DOG would loosen the requirement of gate width from half optical cycle to one optical cycle.
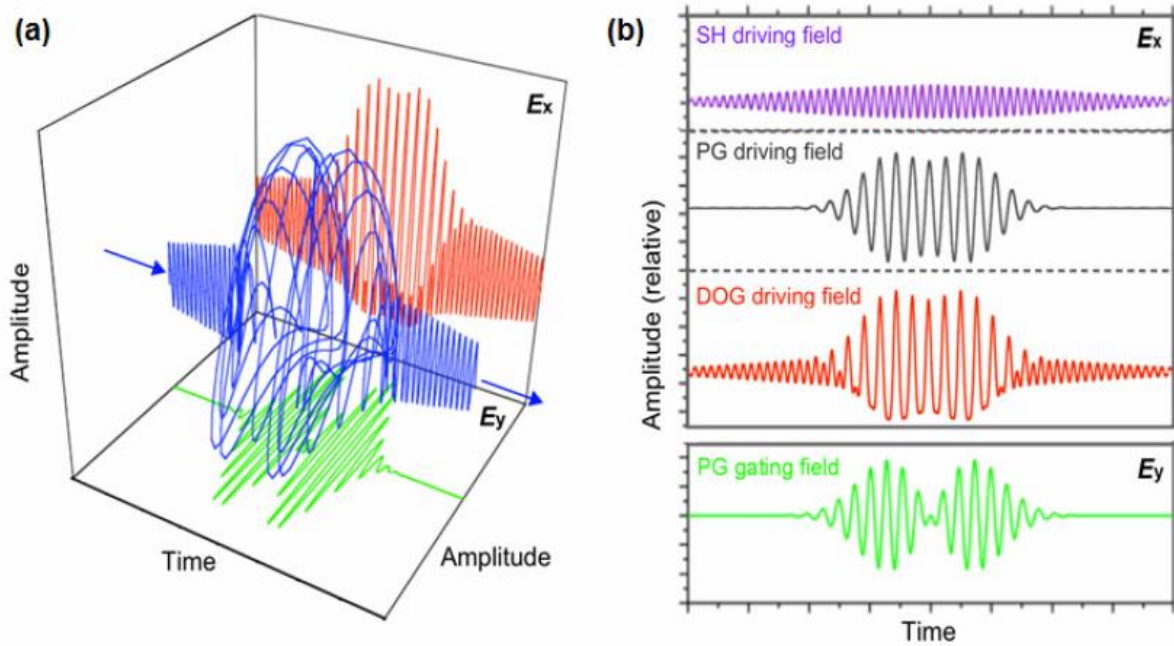
Figure 2.12 (a) The 3D image of total electric field of DOG (blue line); (b) Individual field component of DOG.

2.2.6 Attosecond lighthouse

The attosecond pulse isolating methods mention in section 2.2.1-2.2.6 are based on a time-dependent electric field or field-induced change of the media (ionization gating). Therefore, effective HHG is only allowed within a temporally opened gate time. Another way to isolate the attosecond pulse is to isolate the attosecond burst in space. The idea of attosecond lighthouse [18] technique is based on spatial isolation of each attosecond burst in different direction with a rotated wave front of the driving filed.
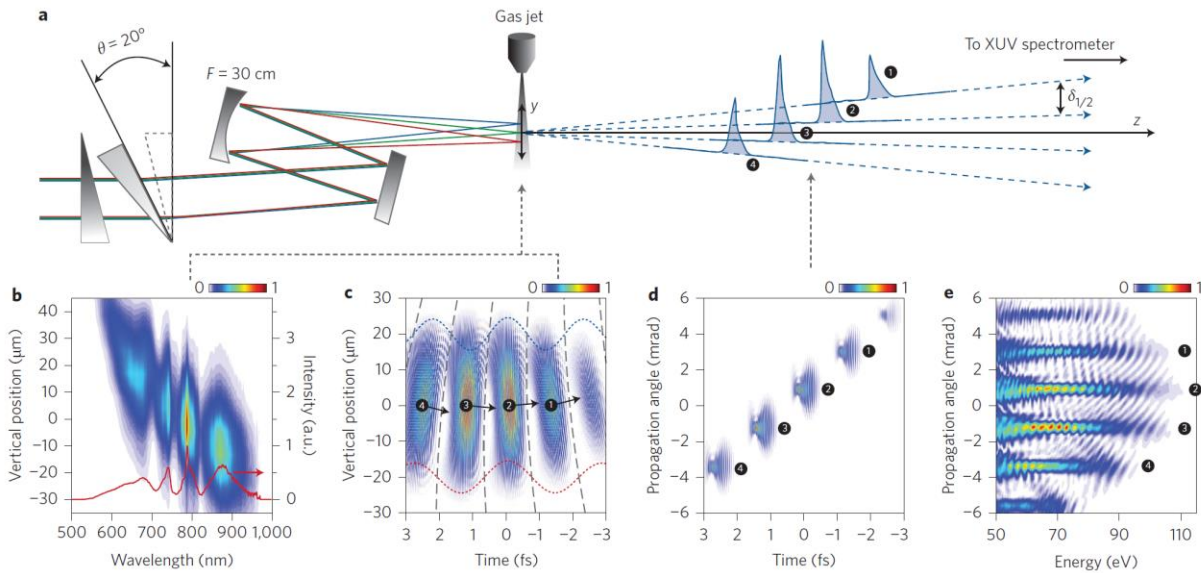
Figure 2.13 (a) Schematic of attosecond lighthouse setup. The angular dispersion of laser beam is introduced by a misaligned pair of wedge. (b) The spatial chirped laser spectrum at the laser focus. (c)-(e) calculated XUV radiation based on the chirp in (b).

Figure 2.13 (c) shows the two electric field (blue dot and red dot) with different frequency are positioned across a $\pm$ 20 μm. the zero crossing times of the electric field (dashed lines) indicates that the wavefront is tilted when comparing the leading and the trailing part of the driving pulse. When such a waveform propagates through the gas media, the harmonic burst generated by each half-cycle field will have a different emission angle — perpendicular to the

24

wave front of the driving field. If the angular separation from nearby half cycle is large such that there is a distinct angular divergence of each harmonic burst, the attosecond pulses can be spatially well separated in the far field. (Figure 2.13 (e))

CHAPTER 3 - FEW CYCLE MID-INFRARED OPCPA LASER

3.1 Extend the HHG cutoff energy

As mentioned in the chapter 2, the HHG cutoff photon energy is given by equation 2.8 and 2.9. The ionization potential I_p is typically less than 30 eV and the ponderomotive energy $U_p \propto I_0 \lambda_0^2$. To increase the HHG cutoff photon energy, an easy way is to increase the laser intensity I_0 by either increasing the driving pulse energy or using a tighter focus. The cutoff photon energies can be extended and reach as high as 460 eV [41] in helium with Ti:sapphire lasers. However, the equation 2.8 and 2.9 discussed here only considers the single atom responds. The HHG signal strength achieved in experiment is the derived from the contributions from all atoms inside the interaction volume. Therefore, HHG signal strength is a coherent buildup of the single atom response which depends on microscopic phase match — the driving field and the HHG field need to propagate at the same phase velocity (speed of light) to ensure the HHG field emitted from different atoms buildup coherently [42, 43]. While the high frequency HHG field rarely interacts with the media and its phase velocity equals to the speed of light, the propagation of driving field is affected by the neutral gas density, free-electron plasma as well as laser focus geometry. Therefore, a balance between the neutral gas density and the plasma density is required and an optimal ionization level can be achieved by controlling the driving field intensity. Using a Ti:sapphire laser centered at 800 nm, the phase matched HHG photon energy is typically limited to 150 eV by with a suitable laser intensity.

With limited intensity for HHG, the alternative way is to increase the driving laser wavelength λ_0. Figure 3.1 shows the experimental demonstration of extend HHG cutoff by increase the driving laser wavelength with constant laser intensity [44].

Figure 3.1 depicting intensity (a.u.) vs. photon energy (eV) with the following annotations:
- (a) $\lambda = 0.8\,\mu m$ — HHG order = 21
- (d) $\lambda = 1.22\,\mu m$ — HHG order = 47, HHG order = 37
- (c) $\lambda = 1.37\,\mu m$ — HHG order = 75, HHG order = 37
- (b) $\lambda = 1.51\,\mu m$ — HHG order = 91, HHG order = 37
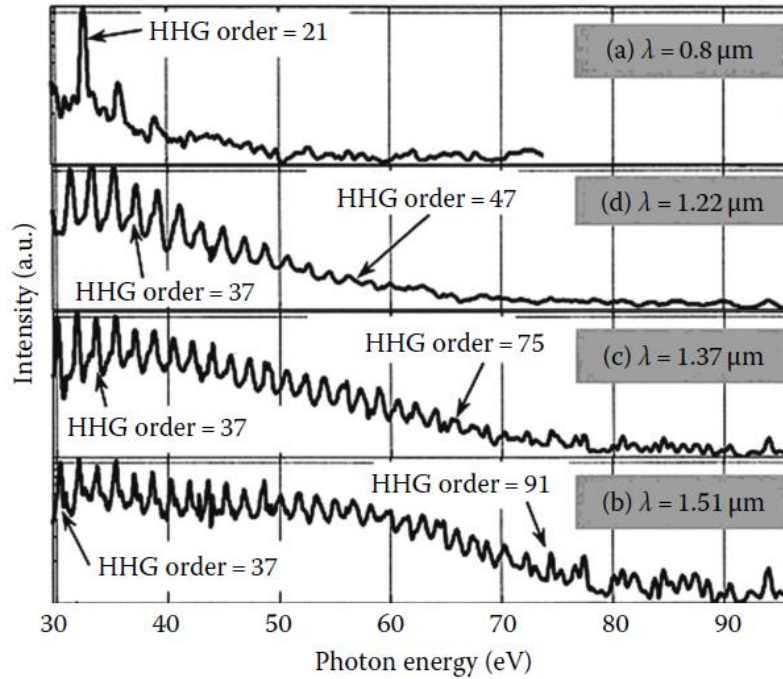
Figure 3.1 Extension of HHG cutoff by increase driving laser wavelength. Figure adopted from ref [44] with modification.

Thanks to the matured technologies of Ti:sapphire laser and chirped pulse amplification, the past decades have witnessed the fast development in generation and control of ultrashort pulses. For the field of attosecond science, a Ti:sapphire laser operating at 800 nm is limited to produce HHG spectrum with photon energy up to 100 eV using neon gas as a target for most applications. Figure 3.2 shows a theoretical prediction of the phase-matched cutoffs as a function of driving field wavelength with various target gas. The predicted HHG cutoffs could reach the water window using three cycle pulses centered at 2 μm using neon gas. However, to produce a

few a cycle pulse in mid-IR range requires a bandwidth over few hundreds nm. Few optical gain mediums could fulfill this requirement.
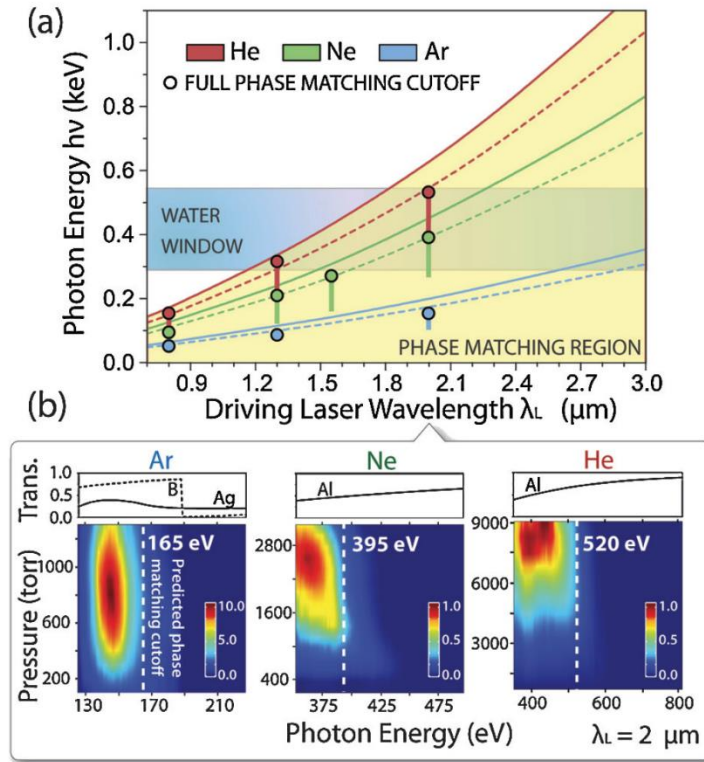
Figure 3.2 Solid (dash) color lines shows the predicted HHG full phase-matching cutoff energy as a function of the driving laser wavelength, for a pulse duration of three (eight) optical cycle. Solid circle shows the observed full phase matching cutoff at 1.3 μm, 1.55 μm and 2.0 μm. Vertical stripes show the observed phase-matching bandwidths. (b) Experimental pressure-tune HHG spectra as a function of press using 2 μm driving pulse. (ref[45])

There are few gain media that could support a broad amplification bandwidth at long wavelength like Ti:sapphire could offer at 800 nm to produce octave spanning spectra. To achieve few cycle pulses at long wavelength, optical parametric processes become a suitable

alternative to traditional gain media based on invertion. Unlike the Ti:sapphire amplifier which relies on an external green laser source to pump the crystal and amplifies the seed pulse through population inversion, in a optical parametric process, the light field does not change the quantum state of the material. As a direct consequence of this, there is no net transfer of energy, momentum, or angular momentum between the optical field and the physical system. The energy transfers from one field to the other depends on the nonlinear polarization of the media.

3.2 Principle of second order nonlinear process.

3.2.1 Principle of optical parametric process

Nonlinear optics is the study of modification of optical property of a material in the presence of light. Shortly after the invention of first laser in 1960 [1], the discovery of second harmonic generation by Franken in 1961 [46] started the field of nonlinear optics. Nonlinear optical phenomena are phenomena that occur when the material response to the applied light field $\vec{E}(t)$ is "nonlinear". The dipole moment per unit volume or polarization $\vec{P}(t)$, of a material determines the material response.

In the case of linear optics, the field introduced polarization depends linearly on the electric field:

$$\vec{P}(t) = \varepsilon_0 \chi^{(1)} \vec{E}(t) \qquad\qquad (3.1)$$

where ε_0 is the permittivity of free space and $\chi^{(1)}$ is known as the linear susceptibility. For nonlinear optics, the polarization $\vec{P}(t)$ could be expressed as a power series in the electric field strength:

$$\vec{P}(t) = \varepsilon_0 \left[\chi^{(1)} \vec{E}(t) + \chi^{(2)} \vec{E}^2(t) + \chi^{(3)} \vec{E}^3(t) + \cdots \right]$$

$$= \vec{P}^{(1)}(t) + \vec{P}^{(2)}(t) + \vec{P}^{(3)}(t) + \cdots \qquad (3.2)$$

Where the $\chi^{(2)}$ and $\chi^{(3)}$ are known as the second- and third-order nonlinear optical susceptibility. Notice that for the vector nature of field $\vec{E}(t)$ and $\vec{P}(t)$. the $\chi^{(1)}$ and $\chi^{(2)}$ are second- and third-rank tensors. $\vec{P}^{(2)}(t) = \varepsilon_0 \chi^{(2)} \vec{E}(t)$ refers to the second order nonlinear polarizability which governs processes such as sum frequency generation (SFG), difference frequency generation (DFG), optical parametric amplification (OPA) and optical rectification (OR). $\vec{P}^{(3)}(t) = \varepsilon_0 \chi^{(3)} \vec{E}(t)$ refers to third order nonlinear polarizability which governs processes such as self-phase modulation (SPM), third harmonic generation (THG) and cross polarized wave generation (XPM). For the second order nonlinearity, assume the optical field (scalar) consists of two distinct frequency components:

$$E(t) = E_1 e^{-i\omega_1 t} + E_2 e^{-i\omega_2 t} + \text{c.c.} \qquad (3.3)$$

The second order nonlinear polarization based on equation 3.2 can then be expressed as:

$$P^{(2)}(t) = \varepsilon_0 \chi^{(2)} \left[E_1^2 e^{-2i\omega_1 t} + E_2^2 e^{-2i\omega_2 t} + 2E_1 E_2 e^{-i(\omega_1+\omega_2)t} + 2E_1 E_2^* e^{-i(\omega_1-\omega_2)t} + \text{c.c.} \right] +$$
$$2\varepsilon_0 \chi^{(2)} [E_1 E_1^* + E_2 E_2^*] \qquad (3.4)$$

It is simpler to express equation 3.4 in the form of:

$$P^{(2)}(t) = \sum_n P(\omega_n) e^{-i\omega_n t} \qquad (3.5)$$

where the summation extends over the positive and negative frequency ω_n. Table 3.1 lists all the various frequency coefficients of $P^{(2)}(\omega_n)$ of the different frequencies ω_n:

Table 3.1 Second order nonlinear polarization

Frequency coefficients	Amplitude	Name of physical process
$P(2\omega_1)$	$\varepsilon_0\chi^{(2)}E_1^2$	SHG
$P(2\omega_2)$	$\varepsilon_0\chi^{(2)}E_2^2$	SHG
$P(\omega_1 + \omega_2)$	$2\varepsilon_0\chi^{(2)}E_1E_2$	SFG
$P(\omega_1 - \omega_2)$	$2\varepsilon_0\chi^{(2)}E_1E_2^*$	DFG/OPA
$P(0)$	$2\varepsilon_0\chi^{(2)}(E_1E_1^* + E_2E_2^*)$	OR

3.2.2 Couple wave equation for difference frequency generation and parametric amplification

Let us consider the $\omega_1 - \omega_2$ frequency component. Two optical waves, the pump and signal with different frequencies interact in a lossless media to generate a new optical wave, the idler wave. To make the subscripts more intuitive, we use ω_p, ω_s, ω_i to denote the pump, signal and idler waves respectively. A key condition for difference frequency generation is showed in figure 3.3. The pump ω_p wave has the highest optical frequency and the relative larger pump photon is split into two smaller photons: $\omega_s < \omega_p$ and $\omega_i = \omega_p - \omega_s$. [47] Through this process, the energy of pump wave is transferred to the signal and idler waves and thus the input signal wave is amplified.
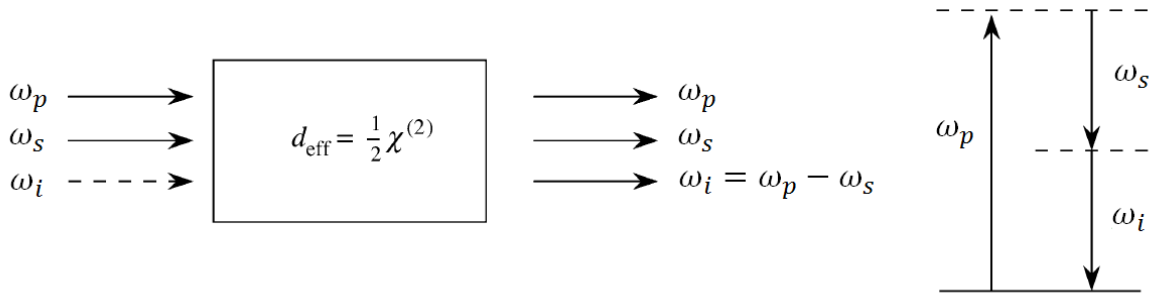
Figure 3.3 Difference frequency generation or parametric amplification. Typically, no input field is applied at frequency ω_i.

To understand the mechanism of the three wave interaction process, we need to derive the coupled wave equations for ω_p, ω_s and ω_i. Let us begin with Maxwell's equation:

$$\nabla \cdot \boldsymbol{D} = \rho = 0 \qquad (3.6)$$

$$\nabla \cdot \boldsymbol{B} = 0 \qquad (3.7)$$

$$\nabla \times \boldsymbol{E} = -\frac{\partial \boldsymbol{B}}{\partial t} \qquad (3.8)$$

$$\nabla \times \boldsymbol{H} = \frac{\partial \boldsymbol{D}}{\partial t} + \boldsymbol{J} = \frac{\partial \boldsymbol{D}}{\partial t} \qquad (3.9)$$

Here we assume the region of interest have no free charge ($\rho = 0$) for free current ($\boldsymbol{J} = 0$). Where $\boldsymbol{D}$ is the electric displacement field, E is the electric field. $\boldsymbol{B}$ is the magnetic field and $\boldsymbol{H}$ is called magnetic intensity. We also assume the material is nonmagnetic

$$\boldsymbol{B} = \boldsymbol{\mu_0}\boldsymbol{H} \qquad (3.10)$$

and allow the media to have a nonlinear in response to the electric field such that the relationship of $\boldsymbol{E}, \boldsymbol{D}$ and polarization vector $\boldsymbol{P}$ is given by

$$\boldsymbol{D} = \varepsilon_0\boldsymbol{E} + \boldsymbol{P} \qquad (3.11)$$

Notice that the polarization vector $\boldsymbol{P}$ depends nonlinearly upon the electric field $\boldsymbol{E}$.

32

We now take curl of $\nabla \times E$ from equation 3.8 and using equation 3.9 and 3.10 to obtain

$$\nabla \times \nabla \times E + \mu_0 \frac{\partial^2}{\partial t^2} D = 0 \qquad (3.12)$$

Add equation 3.11 to 3.12 to eliminate D and using $c^{-2} = \mu_0 \varepsilon_0$ to obtain

$$\nabla \times \nabla \times E + \frac{1}{c^2} \frac{\partial^2}{\partial t^2} E = -\frac{1}{\varepsilon_0 c^2} \frac{\partial^2}{\partial t^2} P \qquad (3.13)$$

The first term of left side of equation can be rewritten using the vector calculus identity

$$\nabla \times \nabla \times E = \nabla(\nabla \cdot E) - \nabla^2 E \qquad (3.14)$$

Under the certain condition, (i.e. if E is a transverse infinite plane wave (see reference [47] chapter 2.1) the contribution from $\nabla(\nabla \cdot E)$ can often be neglected. The equation 3.13 can be rewritten as

$$\nabla^2 E - \frac{1}{c^2} \frac{\partial^2}{\partial t^2} E = \frac{1}{\varepsilon_0 c^2} \frac{\partial^2}{\partial t^2} P \qquad (3.15)$$

By splitting the polarization into linear and nonlinear parts

$$P = P^{(1)} + P^{NL} \qquad (3.16)$$

The equation 3.15 can be rewritten as

$$\nabla^2 E - \frac{\varepsilon^{(1)}}{c^2} \frac{\partial^2}{\partial t^2} E = \frac{1}{\varepsilon_0 c^2} \frac{\partial^2}{\partial t^2} P^{NL} \qquad (3.17)$$

Equation 3.17 has the form of the driven wave equation. The nonlinear response of the medium $\frac{1}{\varepsilon_0 c^2} \frac{\partial^2}{\partial t^2} P^{NL}$ which act as a source term, appears at the right side of equation. Without the source term, the equation 3.17 simplifies itself to the free wave equation of electric field (electric-magnetic field) with velocity $\frac{c}{n}$ where the index of refraction n satisfies $n^2 = \varepsilon^{(1)}$.

To study the electric field in a dispersive media, notice that the linear response for each frequency is different. Therefore, we will consider each frequency component separately. The total electric field is the sums of their various frequency components:

$$E(r,t) = \sum_n E_n(r,t)$$

$$P^{NL}(r,t) = \sum_n P_n^{NL}(r,t) \qquad (3.18)$$

Where each frequency component $E_n(r,t)$, $P^{NL}(r,t)$ is given by

$$E_n(r,t) = E_n(r)e^{-i\omega_n t} + c.c.$$

$$P^{NL}(r,t) = P_n^{NL}(r)e^{-i\omega_n t} + c.c. \qquad (3.19)$$

Inserting equation 3.19 into 3.17, we then have, for each frequency, the following wave equation

$$\nabla^2 E_n(r) + \frac{\omega_n^2}{c^2}\varepsilon^{(1)}(\omega_n)E_n(r) = -\frac{\omega_n^2}{\varepsilon_0 c^2}P_n^{NL}(r) \qquad (3.20)$$

Notice here that $\varepsilon^{(1)}(\omega_n)$ is a frequency dependent dielectric tensor, which is real for lossless medium. To solve equation 3.20 we assume a plane wave solution which propagates in the positive z direction with frequency $\omega_n = \omega_i = \omega_p - \omega_s$:

$$E_i(z,t) = A_i(z)e^{i(k_i z - \omega_i t)} + c.c. \qquad (3.21)$$

Where $k_i = \frac{n_i \omega_i}{c}$ is the wave vector for the idler and $A_i(z)$ is slow varying envelope function of the idler z.

The nonlinear source term in 3.20 is represented as:

$$P_i(z,t) = P_i e^{i\omega_i t} + c.c. \qquad (3.22)$$

Where P_i is obtained from table 3.1 using $\chi^{(2)} = 2d_{eff}$. [47]

$$P_i = 2\varepsilon_0 \chi^{(2)} E_p E_s^* = 4\varepsilon_0 d_{eff} E_p E_s^* \qquad (3.23)$$

By substituting equation 3.21, 3.22 and 3.23 into 3.20, we obtain the simplified wave equation

for the idler wave:

$$\frac{d^2 A_i}{dz^2} + 2ik_i \frac{dA_i}{dz} = -\frac{4d_{eff}\omega_i^2}{c^2} A_p A_s^* e^{i(k_p - k_i - k_s)z} \qquad (3.24)$$

We assume the field amplitude varies slowly: (known as slow varying amplitude approximation)

$$\left| \frac{d^2 A_i}{dz^2} \right| \ll \left| k_i \frac{dA_i}{dz} \right| \qquad (3.25)$$

Which will simplify the wave equations to

$$\frac{dA_i}{dz} = i \frac{2d_{eff}\omega_i}{k_i c \, n_i} A_p A_s^* e^{-i\Delta kz} \qquad (3.26)$$

$$\frac{dA_s}{dz} = i \frac{2d_{eff}\omega_s}{k_s c \, n_s} A_p A_i^* e^{-i\Delta kz} \qquad (3.27)$$

$$\frac{dA_p}{dz} = i \frac{2d_{eff}\omega_p}{k_p c \, n_p} A_s A_i e^{i\Delta kz} \qquad (3.28)$$

Where $\Delta k = k_i + k_s - k_p$ is called wave vector phase mismatch. To solve these equations, we

first assume perfect phase matching $\Delta k = 0$. and also that the pump is undepleted in the small

signal gain limit, i.e. $A_p = constant$, We also assume there is no idler field at the input, i.e.

$A_i(0) = 0$, and a finite amount of signal wave at input $A_s(0) \neq 0$. This is true for the case of

optical parametric amplification or differenc frequency generation. The solution to 3.26 and 3.27

with $A_i(0) = 0$ is found to be ([47] chapter 2.8)

$$A_s(z) = A_s(0)\cosh(\kappa z) \qquad (3.29)$$

$$A_i(z) = i\left(\frac{\omega_i n_s}{\omega_s n_i}\right)^{1/2} \frac{A_p}{|A_p|} A_s^*(0)\sinh(\kappa z) \qquad (3.30)$$

Where

$$\kappa^2 = \frac{4d_{eff}^2 \omega_i^2 \omega_s^2}{k_i k_s c^4} |A_p|^2 \qquad (3.31)$$

The evolution of signal and idler field is shown in figure 3.4 with the assumption of perfect phase match and undepleted pump. We can see from 3.29 that the signal wave ω_s still maintains its initial phase during amplification and the phase of idler wave ω_i depends on both the of the signal wave ω_s and pump wave ω_p.
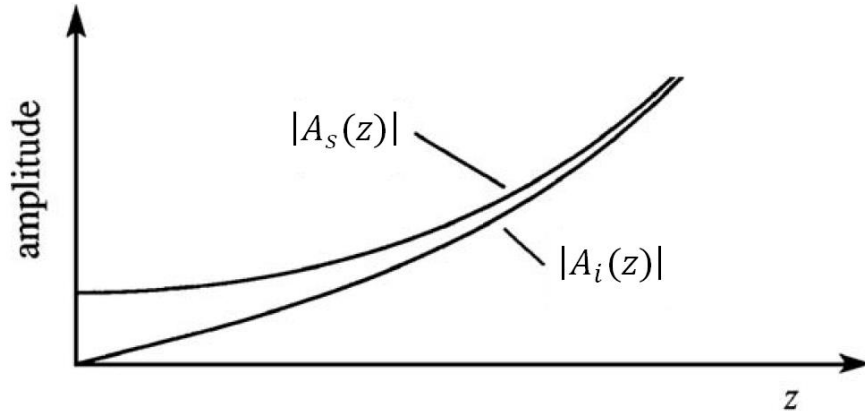
Figure 3.4 Spatial increasing of A_s and A_i for the process of DFG (OPA) for the case of perfect phase match and undepleted pump approximation.

3.2.3 Collinear phase matching

In the coupled wave equation 3.26-3.28, the evolution of A_i, A_s and A_p depend on the phase factor $e^{-i\Delta k z}$ where the wave vector mismatch Δk is could be non-zero. This will lead to poor or even backward conversion in certain cases. Therefore, it is important to maintain Δk small enough so that $\Delta k z < 2\pi$ such that backward conversion is minimized. To achieve that, the wave vector mismatch Δk is given by

$$\Delta k = k_i + k_s - k_p = \frac{n_i \omega_i}{c} + \frac{n_s \omega_s}{c} - \frac{n_p \omega_p}{c} \qquad (3.32)$$

In addition, we must also take into account the conservation of photon energy, i.e. $\omega_i + \omega_s = \omega_p$, Furthermore, for normal dispersion, higher frequency wave will have higher refractive index, therefore $n_p > n_i$, $n_p > n_s$. Under these conditions, $\Delta k \neq 0$. It is also not realistic to achieve perfect phase match using anomalous dispersion since decrease of refractive index with increasing frequency usually occurs near strong absorption. The common way to achieve perfect phase match is by using the birefringent property of crystal. Which means the polarizations of A_i, A_s and A_p are not in the same plane.

A uniaxial birefringent crystal could be positive ($n_e > n_o$) or negative ($n_e < n_o$). A biaxial crystal could also be applied for phase matching. Therefore, different configurations with respect to polarization orientations are possible for perfect phase match. Type I phase match is defined such that the two low frequency component ω_i and ω_s are polarized in the same direction, and type II phase match happens when the two low frequency component ω_i and ω_s are polarized perpendicular to each other. To give a more intuitive picture of phase matching in a birefringent crystal, let us study how phase matvhing is done using a BIBO crystal. Figure 3.5 shows the refractive index of BiB_3O_6 (BIBO) [48]. Three frequency components fulfilling the relation 3.32 are indicated by the solid dotted line. The polarization for the pump wave ω_p (~ 0.588 μm) and signal wave ω_s (~ 0.93 μm) is along the one of the principle (optical) axis: Y-axis of biaxial crystal. Therefore, the Sellmeier equation for calculating refractive index n_y [48] is chosen for pump and signal field. The generated idler field (ω_i near 1.6 μm) is polarized in the X-Z plane. The phase match angle θ between wave vector direction (k_i in this case) and Z-axis

37

is optimized at 57 degree to fulfill equation 3.32, the refractive index n_i should be replaced by an

effective refractive index n_{eff} for the idler field, whose value is in between n_x and n_z. Given by

equation:

$$n_{eff}^2 = \frac{n_x^2 \times n_z^2}{\sin^2\theta \times n_x^2 + \cos^2\theta \times n_z^2}$$

(3.33)
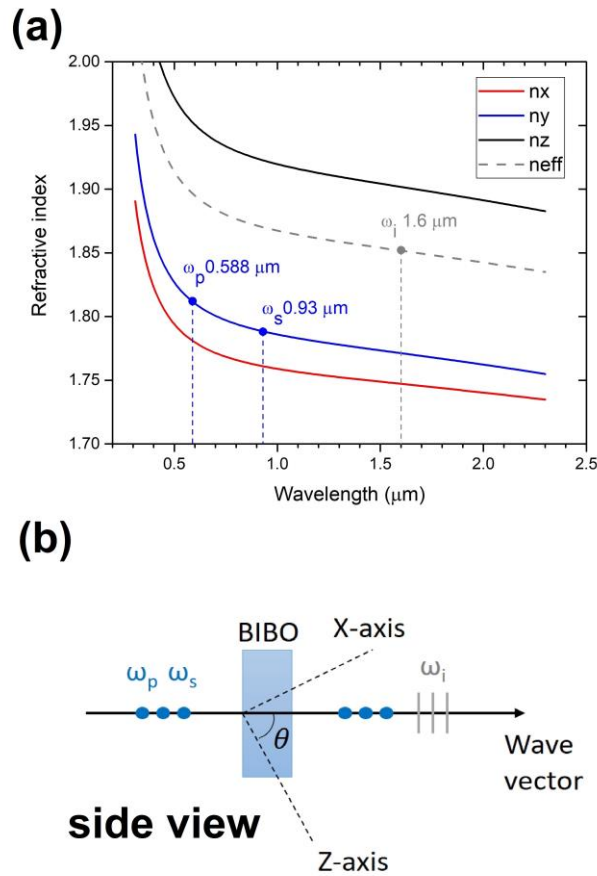
Figure 3.5 (a) Optical refractive index of BIBO crystal for type II interaction (0.588 µm(o) → 0.93 µm(o) +1.6 µm(e)) (top). Refractive index for X, Y and Z-axis is plotted in red, blue and black line. Refractive index for idler wave is plotted in dashed gray line with a phase matching angle of θ=57 degree. (b) Side view of crystal oriental with respect to the input field polarization.

The wave mixing configuration in Figure 3.5 shows the current generating idler wavelength (1.2 - 2.3 μm) in the author's lab. The 0.5-0.9 μm broadband white light pulse, which serves as both the pump and signal field, is focused intoa BIBO crystal to produce the OPCPA seed pulse through a process called intra-pulse DFG. Intra pulse DFG has a unique passive CEP stabilization feature such that the CEP of the idler is insensitive to the CEP of the input pulse [49, 50]. The phase (CEP) of the idler field dependent on the phase difference between the pump and signal field (based on equation 3.26). The pump and signal field are both from the same white light pulse and thus have the same phase (CEP) value. Therefore, the generated idler field has a constant phase (CEP) for each laser shot.

One can figure out the correct polarization scheme for achieve type I or II phase matching (equation 3.32) after determining the refractive index for each input field. The phase matching efficiency ([47] chapter 2.3) is proportional to $sinc^2(\Delta kL/2)$, where Δk is given by equation 3.32 and L is the propagation distance inside the birefringent crystal. Figure 3.6 shows the influence of wave vector mismatch on the efficiency of SFG process ([47] chapter 2.3).
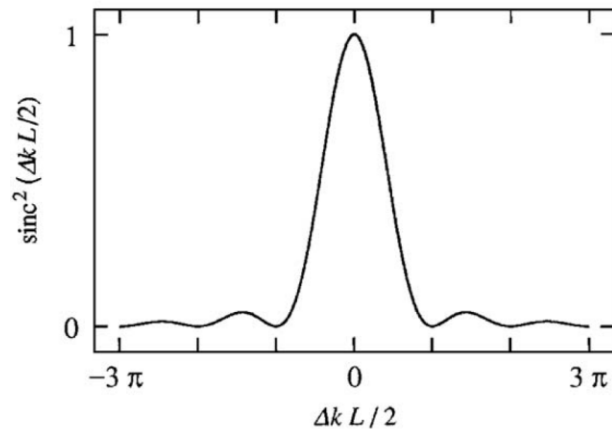
Figure 3.6 Effect of wave vector mismatch on the efficiency of SFG.

Since Δk can be calculated using equation 3.32 and 3.33, one can calculate the efficiency of any wave mixing process (SFG, SHG and DFG etc.). Figure 3.7 shows the calculated phase matching efficiency for the intra-pulse DFG process illustrated in the figure 3.5. Each coordinate in figure 3.7 corresponds to a wavelength combination of λ_p (horizontal), λ_s (vertical) and λ_i (given by $\omega_p - \omega_s$). The location of the red strip indicates the area that will have a good phase match. By plotting the phase matching efficiency in figure 3.7, we can intuitively find the idler wavelength range that can be phase matched (1.1-2.3 μm in figure 3.7). The detailed experiment result will be discussed in section 3.3.
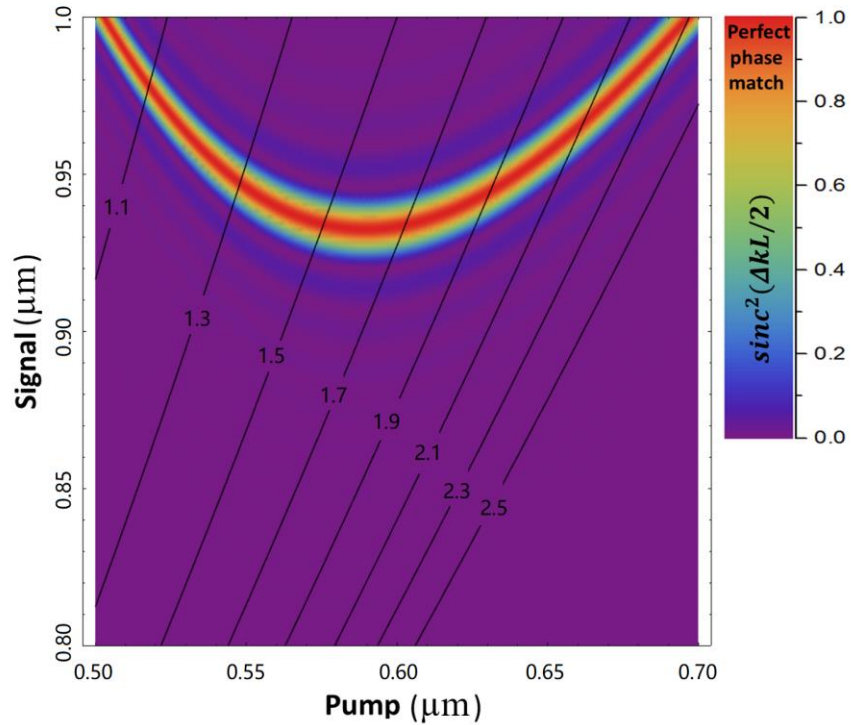
Figure 3.7 Efficiency of a type II phase matching for intra-pulse DFG process in a 1 mm thick BIBO crystal cutting at θ=57. The solid black lines indicate the location of constant wavelength (in μm) for the idler wave.

3.2.4 Non-collinear phase match

The intra-pulse DFG example discussed in 3.2.3 is a collinear case that fulfills equation 3.32. All three fields have the same propagation direction shown in figure 3.8 (a) and the wave vector mismatch Δk (for the case in figure 3.5) is eliminated by tuning the phase match angle θ ($\theta = 57$ for the case in figure 3.5).

In the case of non-collinear geometry, a small non-collinear angle α is introduced between the pump and the signal field. The angle α allows for a greater selection of frequency combinations (ω_p, ω_s and ω_i) to achieve a small mismatch, which implies a broader phase match bandwidth can be achieved.

collinear phase match   non-collinear phase match
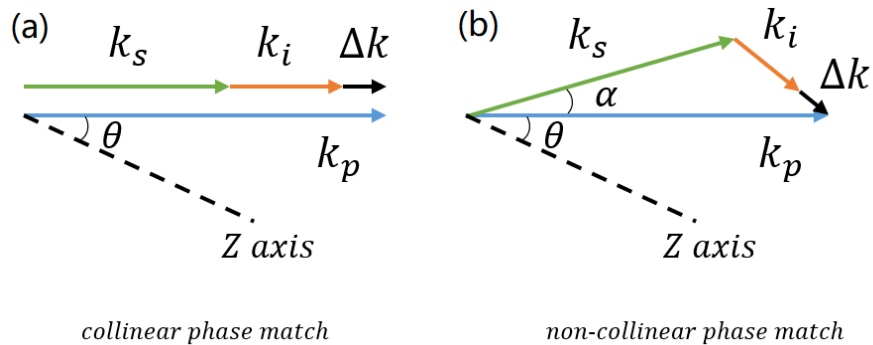
Figure 3.8 Two geometries used for achieving angle phase match. (a) collinear case: all three wave vectors are parallel and only phase match angle θ is optimized to achieve minimal mismatch. (b) non-collinear case: a non-collinear angle α is introduced between two non-zero input field (signal and pump in this case). The wave vector direction of the third filed (idler in this case) is determined by the vector difference ($k_p - k_s$). Both θ and α can be optimized to achieve broadband phase match.

To calculate the wave vector mismatch $\Delta \boldsymbol{k}$ for non-collinear geometry, note first that the absolute value of $\Delta k = |\Delta \boldsymbol{k}|$ is still subjected to the vector difference between $\boldsymbol{k}_i$ and $\boldsymbol{k}_p - \boldsymbol{k}_s$. The value of wave vector mismatch Δk is can be calculated by:

$$\Delta k = \sqrt{k_p^2 + k_s^2 - 2k_p k_s cos\alpha} - k_i \qquad (3.34)$$

One can easily find that equation 3.32 is the simplified case of equation 3.34 with $\alpha = 0°$.

An example of non-collinear OPA phase match is shown in figure 3.9. An output from a Ti:shapphire amplifier centered near 0.8 μm is used as the pump field. The signal wave is the DFG (centered at 1.6 μm) generated using the scheme illustrated in figure 3.6.
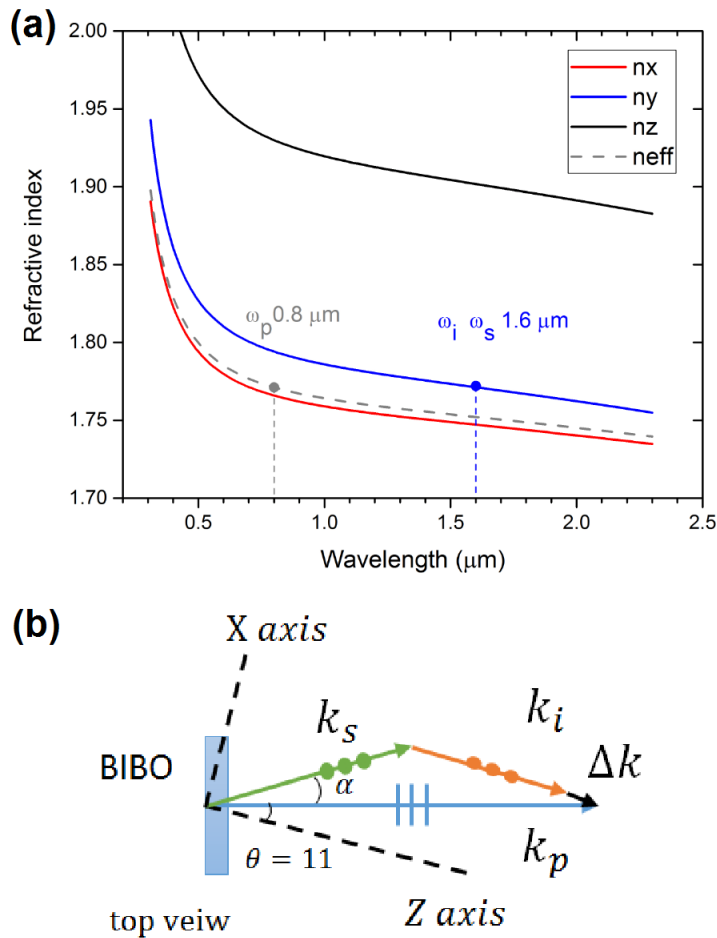
Figure 3.9 (a) Optical refractive index of BIBO crystal for type I interaction (0.8 μm(e) → 1.6 μm(o) +1.6 μm(o)). Refractive index for X, Y and Z-axis is plotted in red, blue and black line. Refractive index for pump wave is plotted in dashed gray line with a phase matching angle of θ=11 degree. (b) Top view of crystal oriental with respect to the input field polarization.

The polarization of the pump field is in the X-Z plane, while the signal and idler field is polarized along the Y-axis. Notice that the signal and idler field are both centered at 1.6 μm with the same polarization. Therefore, it is impossible to separate them in a collinear geometry. The non-collinear α not only separates the three wave spatially in the far field, but also adds another degree of freedom to allow for the modification of the phase matching conditions for the different frequency combinations (ω_p, ω_s and ω_i). The wave vector mismatch Δk in this case can be calculated using equation 3.34. According to figure 3.9 (a) n_y, n_y and n_{eff} should be used for ω_p, ω_s and ω_i to calculate k_p, k_s and k_i. The result will be discussed in next section.

3.3 A 3 mJ, 12 fs, OPCPA laser system at 1KHz

To extend the HHG cutoff photon energy, a long wavelength driving source is to take advantage of the λ^2 scaling of the cutoff energy. However, the single atom HHG efficiency falls dramatically with unfavorable $\lambda^{-5} \sim \lambda^{-6}$ scaling [51]. Phase matching for HHG must be optimized to overcome this drawback [42, 45]. A high energy driving pulse with a loose focus geometry will increase the interaction volume and minimize the phase shift introduced by the geometric focusing. Therefore, a high energy ultra-short pulse with long wavelength is desired for producing high cutoff energy photon with high flux.

A 3 mJ, 12 fs, OPCPA laser system has been developed in author's lab. The OPCPA have an output spectrum centered at 1.6 μm. The nonlinear BIBO crystal is working near degenerate condition ($\omega_i \approx \omega_s = 1.6$ μm, $\omega_p = 0.8$ μm), the group delay dispersion inside BIBO is close to zero for the signal and idler wave near 1.6 μm. These conditions allow for a

broadband phase match bandwidth required to preserve the board seed spectrum in the amplification process [52].

3.3.1 Ti:sapphire pump laser system
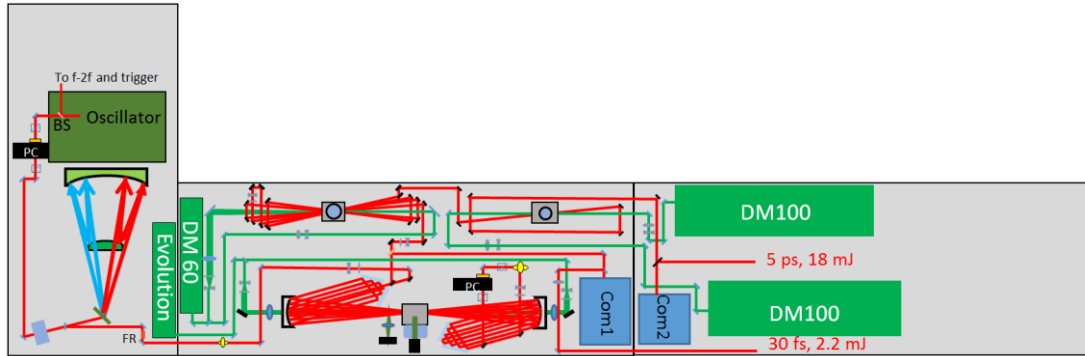
Figure 3.10 Schematic setup of Ti:sapphire laser system for pumping OPCPA.

To meet the requirements for pumping the OPCPA laser, a powerful front end pump laser operating near 0.8 μm has been developed based on the Ti:sapphire CPA technology. Figure 3.10 shows a schematic illustration of our front end Ti:sapphire pump laser system. The laser system starts from a mode-locking oscillator (Thorlabs, OCTAVIUS, 85 MHz). A pockel cell is used to reduce the repetition rate to 1/80000 of 85 MHz. The near 1KHz nanojoule-level output pulse is stretched to 360 ps (730-830 nm) using an Offner-type stretcher [53, 54] consisting of a 1400 lines/mm transmission grating (LightSmyth) working in littrow configuration with a high diffraction efficiency (92% for single pass). The seed pulse is then amplified to 4 mJ after the first stage 14-pass amplifier which consists of a Ti:sapphire crystal that is cooled to 173 K by the cold finger of a liquid immersion chiller. After the first stage, the beam is split into two parts, 2.6 mJ of the 4 mJ is send to a grating pair for pulse compression. The compressed 30 fs, 2.2 mJ pulse is then used for generating the seed for OPCPA laser. The remaining 1.4 mJ out of 4 mJ is

then sent to the second stage 6-pass amplifier to boost the pulse energy to 10 mJ, the crystal is

cooled to 50 K by Cryomech (PT60, 60W) to reduce the thermal issues. The final stage is a

single pass amplifier stage with an output pulse energy of 21 mJ when using with 532 nm, 80 mJ

of pump energy. The final stage is also cooled to 50 K with 200 W of cooling power (Cryomech

AL300). The amplified pulse is then compressed by a second grating pair to 18 mJ, 5 ps with

negative chirp. This pulse is later used for pumping the OPCPA laser. A typical output spectrum

from Ti:sapphire amplifier is showed with red line in figure 3.11.
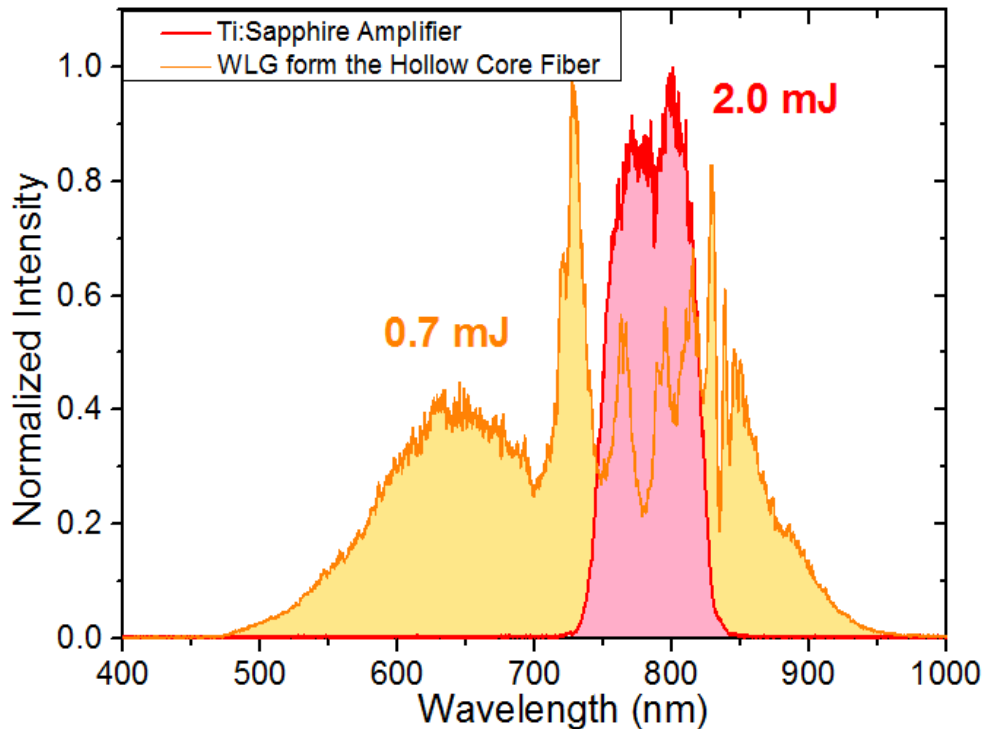
Figure 3.11 The Ti:sapphire amplifier output spectrum for seeding the hollow core fiber (red); White light spectrum after hollow core fiber (yellow).

3.3.2 BIBO crystal based OPCPA

To achieve a seed spectrum from 1.2 to 2.3 μm, we applied the intra-pulse DFG technique as discussed in chapter 3.2.1. Figure 3.12 show a schematic drawing of OPCPA laser system in author's lab. The 30 fs, 2.2 mJ pulse centered near 0.8 μm is loosely focused into a hollow core fiber (350 μm in diameter) filled with 30 psi of neon gas. The self-phase modulation (SPM) effect accumulated during pulse propagation inside the neon gas will broaden the spectrum [47]. Figure 3.11 compares the spectra before and after SPM. The white light pulse produced by the SPM is positively chirped. Pairs of chirp mirrors are used to compensate the positive chirp of pulse from SPM and positive material dispersion (exit window, focus lens etc.) to achieve a 7 fs pulse before being focused into a 0.5 mm BIBO to generate the OPCPA seed usingintra-pulse DFG as discussed in chapter 3.2.2. The frequency mixing process produces a seed spectrum from1.2 to 2.3 μm (figure 3.13). Since the polarization of DFG field is orthogonal to the white light field. A silicon window is oriented at the Brewster angle for the white light field (75°). Therefore, the white light field is transmitted into the silicon window and gets absorbed while the DFG pulse is partially (~75%) reflected. The typical DFG energy after silicon reflection is 1 μJ. An acousto-optic programmable dispersive filter (AOPDF, purchased from FASTLITE) [55, 56] is used as a stretcher to positively chirp the DFG pulse to 4.4 ps with ~ 5% diffractive efficiency. The remaining energy for seeding the first parametric amplifier stage is about 50 nJ.
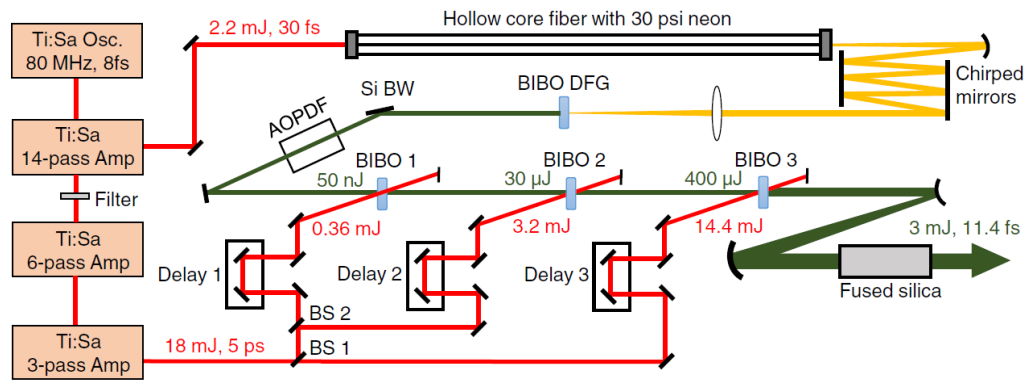
Figure 3.12 Schematic setup of the OPCPA system. BS1, 20% reflection beam splitter; BS2, 10% reflection beam splitter; Si BW, silicon window at Brewster's angle. Figure adopted from ref [57]

The 50 nJ seed pulse is then amplified by 3 stages. Each BIBO is working at a phase matching angle of $\theta = 10.8°$. A small noncollinear angle of $\alpha = 0.6°$ is introduced to separate the signal beam from pump and idler as discussed in chapter 3.2.4. The first and second BIBO in amplifier stage are 5 mm in thickness. They are pumped by 0.36 mJ and 3.2 mJ energy respectively. The amplified signal pulse energy is 30 uJ (gain of 600) and 400 uJ (gain of 13) respectively. The gain in the first stage can be kept low thanks to our high energy seed (50 nJ). Therefore, the parametric fluorescence is low in first stage OPCPA. In the third stage, a pump power of 14.4 mJ is used to achieve 3 mJ output energy for the signal field.
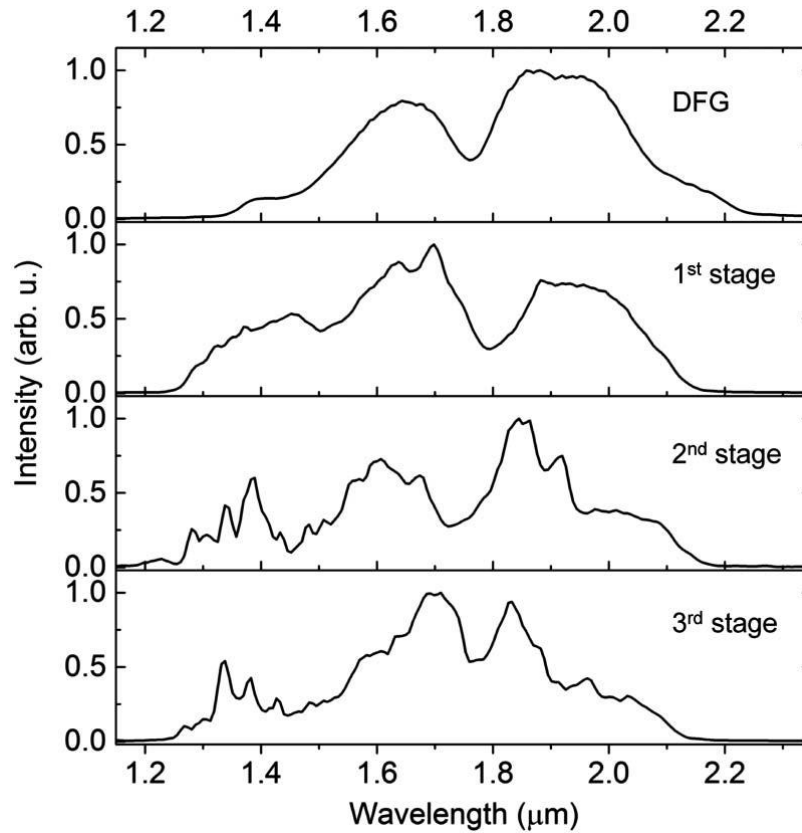
Figure 3.13 Spectra taken at different stages of OPCPA laser system.

The spectra of the signal wave at seeding and three amplification stages are compared in figure 3.13. All spectrum components from 1.2 to 2.3 μm are well preserved during amplification due to our broad phase-matching bandwidth. Equation 3.34 is used to calculate the phase-matching bandwidth in our 3-stage parametric amplifier using BIBO crystal (described in figure 3.9). The calculated phase-matching efficiency between the signal and pump wavelength is plotted in figure 3.14 (b). Only the signal wavelength is plotted versus pump wavelength as the idler field is spatially chirped for non-collinear geometry and is hence not useful in our case. Each coordinate in figure 3.14 (b) correspond to a combinations of wavelengths from pump (x-axis), signal (y-axis) and idler (calculated using $\omega_i = \omega_p - \omega_s$). An optimized phase matching

condition, $\theta = 10.8°$ and $\alpha = 0.6°$, is used when calculating the phase-matching efficiency. The

result ($sinc^2(\Delta kL/2)$) is color plotted. The areas of perfect phase match are denoted by red

color. The Mathematica code for calculating noncollinear phase matching is attached in

Appendix B.

Unlike conventional OPA where is the signal and pump pulses are close to transform

limited. Our signal and pump pulses are both chirped to near 5 ps. The chirp for the pump pulse

is controlled by varying the distance of a grating pair [58]. A dominating second order dispersion

from grating pair chirped the pump pulse almost linearly. The chirp of the signal pulse is decided

by the amount of dispersion in the stretcher (Dazzler in our case), which should match with the

dispersion of the 150 mm bulk fused silica compressor. Therefore, the chirp of signal pulse

inside the amplifier is opposite to the material dispersion from the bulk compressor.

In the time domain, the signal or pump field's instantaneous frequency varies from

leading edge to trailing edge. The black dots in figure 3.14 (b) indicates the phase-matched

wavelengths from signal and pump in time domain. The coordinates of the black dots fall within

the red region with good phase matching.
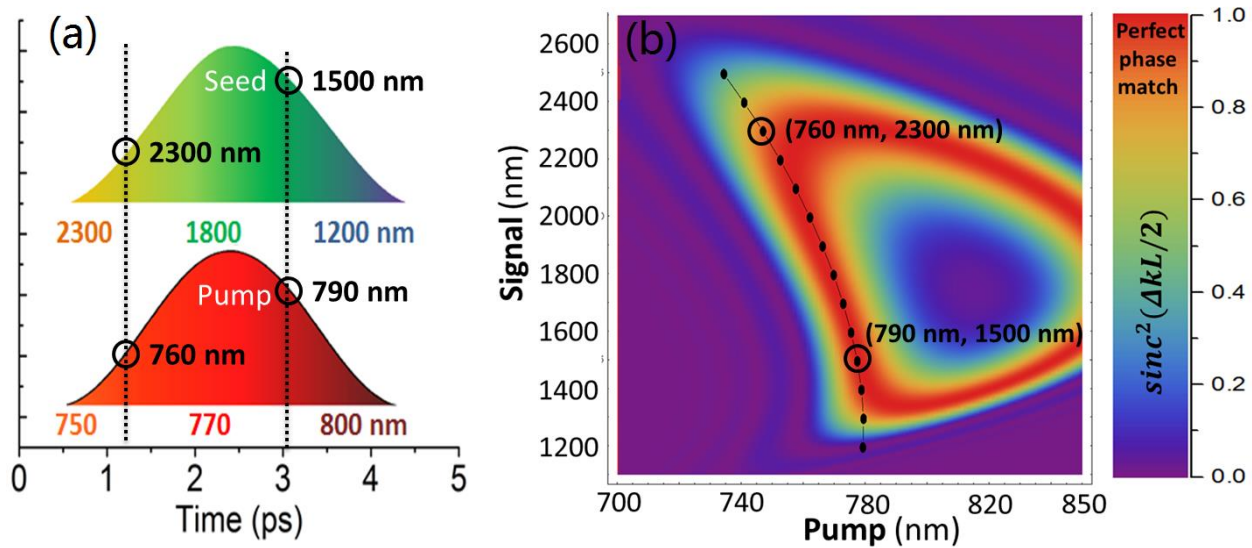
Figure 3.14 Time domain phase match in OPCPA system. (a) A schematic illustration of a positively chirped seed (signal) and a negatively chirped pump pulse overlap in time domain. The dashed lines indicate the matched two wavelengths in time. (b) Calculated phase match efficiency ($sinc^2(\Delta kL/2)$) as a function of pump and signal wavelength in BIBO crystal using the condition θ =10.8° and $\alpha = 0.6°$. The black dots indicate the time-domain matched wavelength pairs from signal and pump pulse obtained from (a). The chirp of the signal and pump pulse during three OPCPA stage is determined by fused silica compressor (in figure 3.12) and second grating pair (in figure 3.10) respectively.

3.3.3 Dispersion control

Since the seed pulse (1.2-2.3 μm) is generated by intra-pulse DFG inside the first BIBO crystal, the signal pulse goes though many dispersive optical components inside the OPCPA system. These dispersion components include dazzler, lens, BIBO crystals, air, 150-mm bulk compressor and even gating optics for HHG/attosecond experiments. To achieve near Fourier transform limited pulse duration, the dispersion introduced by the dazzler should be opposite to sum of dispersion from the rest of system, which can be calculated using material dispersion equation. For a simple estimation, let us consider only the dispersion from 150 mm of fused silica and ignore the dispersion from lens, BIBO crystals, air and gating optics, since their

50

cumulative GDD is small compared to 150 mm fused silica, and determine how much dispersion

compensation must be applied using the Dazzler. The phase shift introduced by 150 mm fused

silica is given by:

$$\boldsymbol{\varphi}(\boldsymbol{\omega}) = \boldsymbol{\omega} \times \boldsymbol{L} \times \boldsymbol{n}(\boldsymbol{\omega})/\boldsymbol{c_0} \qquad (3.35)$$

where $L = 150\ mm$, $n(\omega)$ is the frequency dependent refractive index for IR fused silica that

can be calculated using Sellmeier coefficients. The total phase shift can also be approximated

using Tylor expansion with central angular frequency ω_o ($\omega_o \sim 1.7\ \mu m$) :

$$\boldsymbol{\varphi}(\boldsymbol{\omega}) = \boldsymbol{\varphi_o} + \left(\frac{\partial \varphi}{\partial \omega}\right)(\boldsymbol{\omega} - \boldsymbol{\omega_o}) + \frac{1}{2!}\left(\frac{\partial^2 \varphi}{\partial \omega^2}\right)(\boldsymbol{\omega} - \boldsymbol{\omega_o})^2 + \frac{1}{3!}\left(\frac{\partial^3 \varphi}{\partial \omega^3}\right)(\boldsymbol{\omega} - \boldsymbol{\omega_o})^3 + \frac{1}{4!}\left(\frac{\partial^4 \varphi}{\partial \omega^4}\right)(\boldsymbol{\omega} -$$
$$\boldsymbol{\omega_o})^4 + \frac{1}{5!}\left(\frac{\partial^5 \varphi}{\partial \omega^5}\right)(\boldsymbol{\omega} - \boldsymbol{\omega_o})^5\dots \qquad (3.36\ )$$

The first, second, third, fourth and fifth order coefficients correspond to the dispersion terms

group delay (GD), group delay dispersion (GDD), third order dispersion (TOD), fourth order

dispersion (FOD) and fifth order dispersion (FID) respectively.

Table 3.2 Taylor series of dispersion terms from a 150 mm fused silica.

Spectrum phase series	formula	Value for 150 mm fused silica ($\omega_o \sim 1.7\ \mu m$)
GD	$\partial \varphi\ /\ \partial \omega$	$732402\ fs$
GDD	$\partial^2 \varphi\ /\ \partial \omega^2$	$-7137\ fs^2$
TOD	$\partial^3 \varphi\ /\ \partial \omega^3$	$33164\ fs^3$
FOD	$\partial^4 \varphi\ /\ \partial \omega^4$	$-126633\ fs^4$
FID	$\partial^5 \varphi\ /\ \partial \omega^5$	$-669086\ fs^5$

The first order GD only delays the pulse in time which does not change the shape of the pulse. The other high order terms will change the pulse shape in time domain. In figure 3.15, gives readers an idea of how compensating each term would affect the pulse shape in time domain. Figure 3.15 (a) shows the simulated spectrum centered at 1.7 μm wavelength. Figure 3.15 (b) shows the corresponding Fourier transform-limited electric field in the time domain. Figure 3.15 (c) is the calculated GDD by assuming that only the second order dispersion from 150 mm FS is compensated. In other words, only TOD, FOD, FID etc. from a 150 mm fused silica is applied to the spectrum phase in Figure 3.15 (a) and the corresponding electric field is showed in Figure 3.15 (d). One can easily see from figure 3.15 (d) that to achieve a near transform limited pulse, second order dispersion compensation alone is not enough. Similarly, in figure 3.15 (e), (g) and (i), up to TOD, FOD and FID dispersion are compensated respectively and their corresponding Fourier transformed E-fields are plotted in (f), (h) and (j). One can see in figure 3.15 (g) that a minimum of phase compensation up to FOD is necessary to achieve a pulse that is approximately close to transform limited. To achieve a near transform-limited pulse in figure 3.15 (j), the FID would also need to be compensated as well.
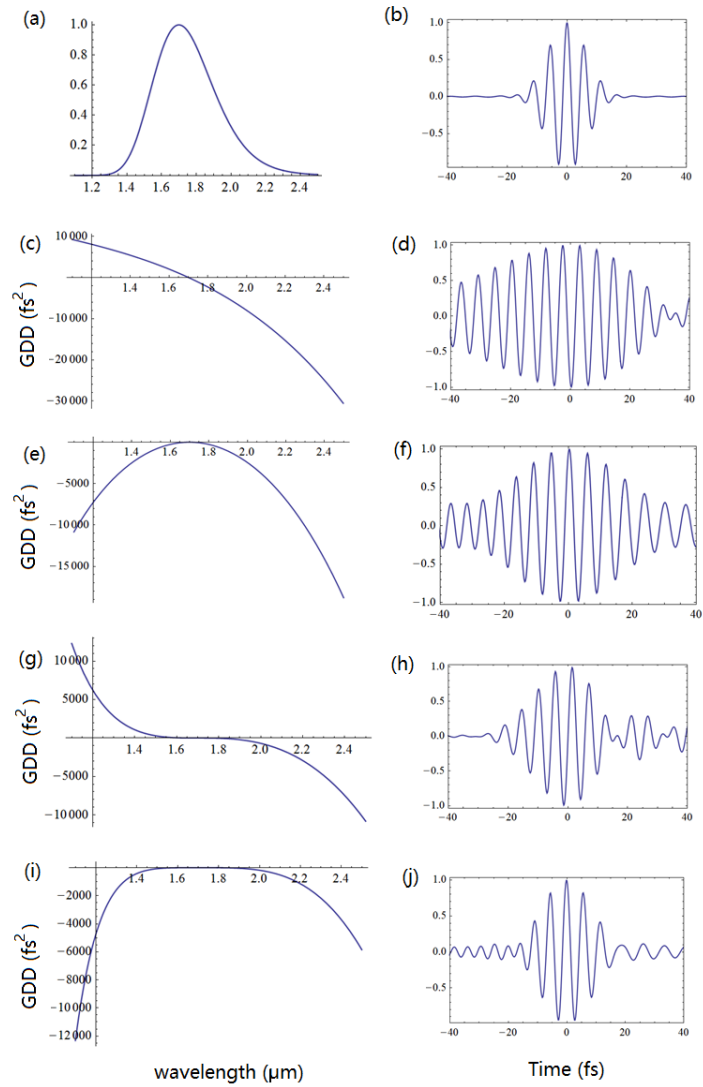
Figure 3.15 the influence of GDD, TOD, FOD and FID on the optical pulse compression of a broad spectral pulse. (a) the simulated spectrum; (b) the Fourier transform-limited e-field from (a). (c), (e), (g) and (i) calculated GDD with phase compensation up to 2nd, 3rd, 4th and 5th order respectively and their corresponding time domain E-field in (d), (f), (h) and (j).

In the experiment, the pulse duration after compression is measured by a home-made second harmonic generation frequency resolved optical gating (SHG-FROG) [59]. Due to our high pulse energy, the laser field intensity is high enough to produce adequate SHG signal inside BIBO crystal without focusing. Therefore, a single-shot geometry is chosen for simplicity when combined with an image spectrometer (figure 3.16) [60]. The laser beam with good beam profile is split into left and right half circle by a pair of split mirrors. The reflected two beams with a small angle (~2°) overlap inside a 20 μm thick BBO crystal cutting at 22°. The temporal information is therefore encoded in the horizontal direction. The laser beam is then rotated by 90°. The fundamental driving field is filtered out in space by a slit near the image mirror, which image the SHG pattern (at BBO crystal) onto the entrance slit of image spectrometer. Since the laser beam is rotated by 90°. The temporal information of the SHG pattern is now in the vertical direction which is preserved inside the image spectrometer. The spectrum is spatially separated by image spectrometer in the horizontal direction. A CDD camera records the 2D FROG trace for retrieval. Figure 3.17 shows a 11.4 fs pulse measure by FROG. A typical pulse duration of 12 fs is expected for daily operation.
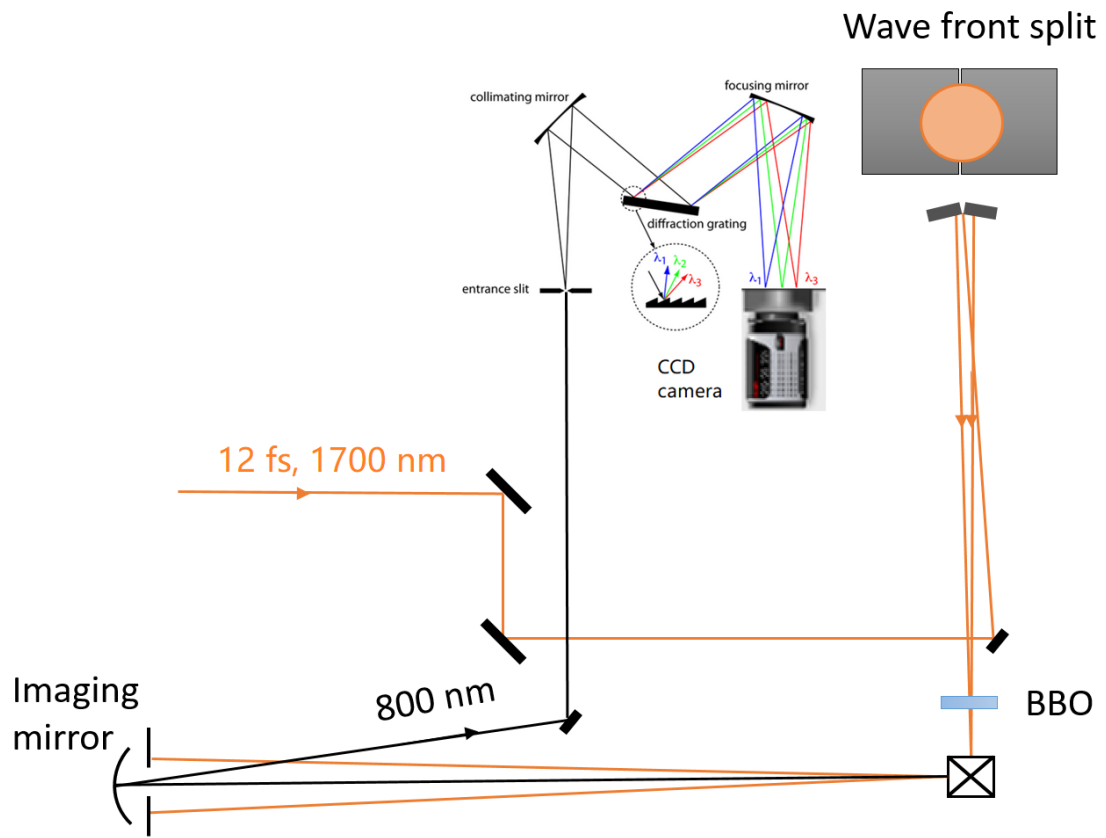
Figure 3.16 Setup for second harmonic generation frequency resolved optical gating (SHG-FROG). Laser beam is collimated into the BBO crystal.
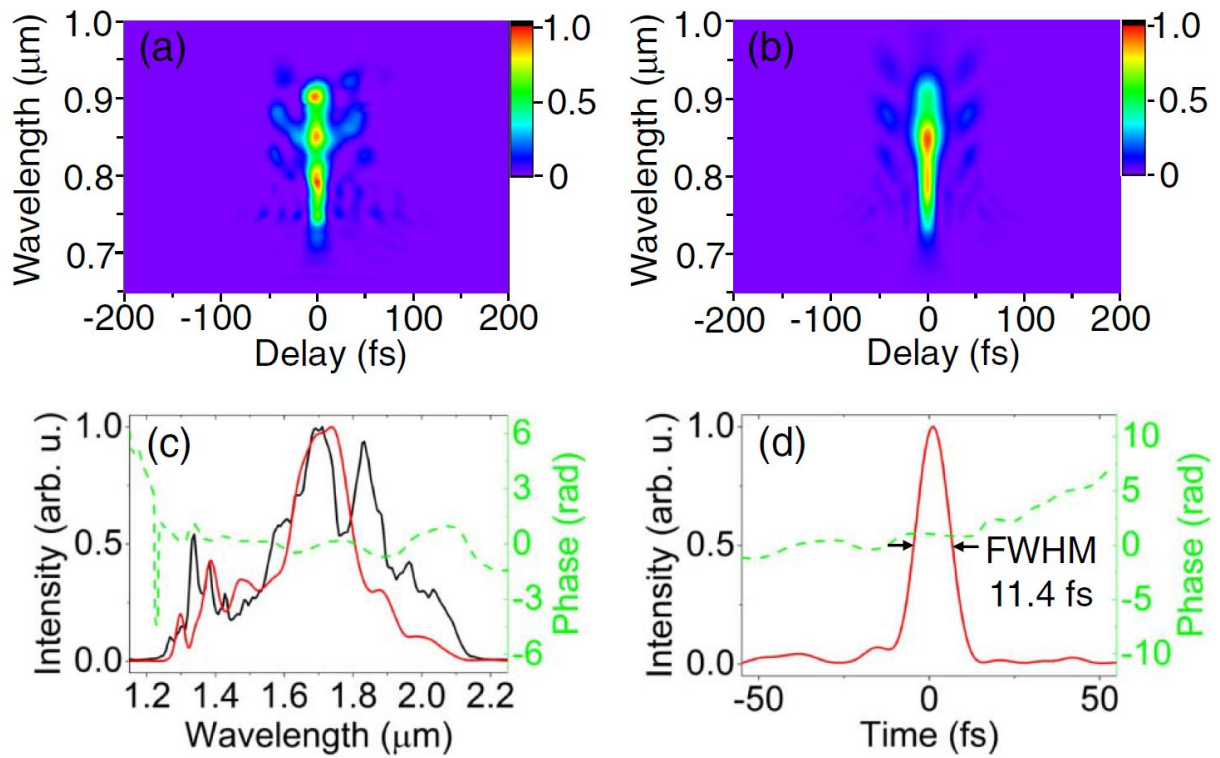
Figure 3.17 (a) Experimental SHG FROG trace; (b) retrieved SHG FROG trace; (c) independently measured spectrum (black), retrieved spectrum (red), and retrieved spectral phase (green); (d) retrieved pulse (red) and temporal phase (green).

3.3.4 CEP stability

As discuessed in chapter 3.2.3. the CEP of our seed pulse is passively stablized through the intra-pulse DFG process [49, 50]. The Dazzler with the jitter free feature can preserve the CEP value during pulse stretching. The material dispersion inside the laser system does not intraduce significant CEP fluctration. Therefore, the CEP of output pulse is also passively stablized. Figure 3.18 shows a single-shot f-to-2f measurement of the CEP fluctuation which is about 165 mrad for 1 hour.
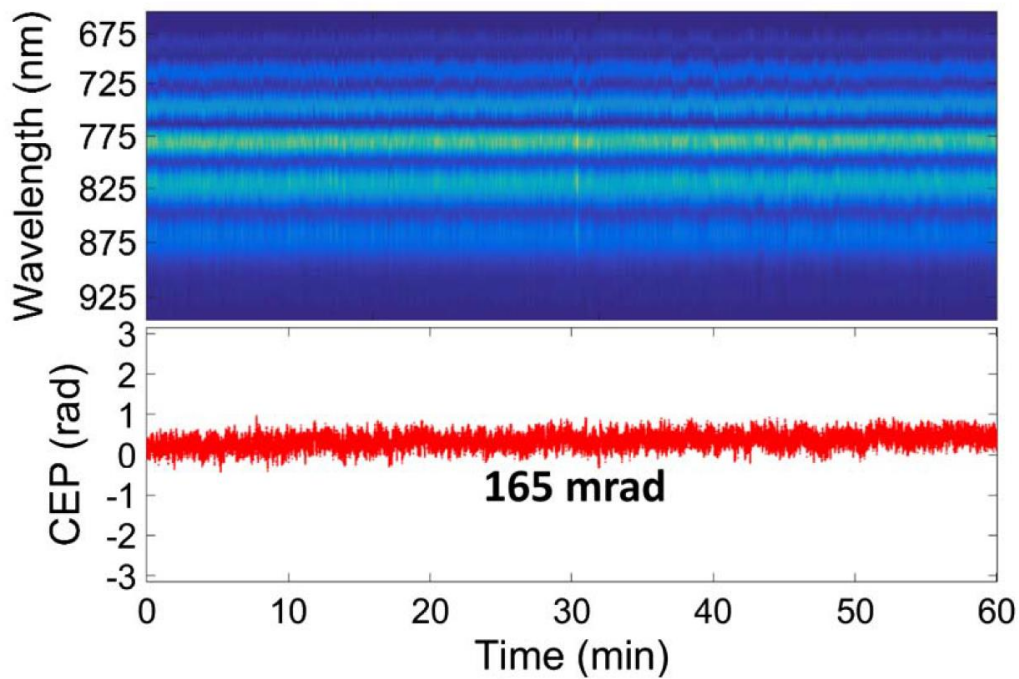
Figure 3.18 Top: f-to-2f interferograms collected for 1 h; bottom: CEP fluctuations (165 mrad RMS) in 1 hour.

CHAPTER 4 - GENERATION OF ISOLATED SOFT X-RAY
ATTOSECOND PULSES

The OPCPA laser system described in chapter 3.3 is capable to deliver 12 fs, 3 mJ pulses at 1 KHz repetition rate. Its bandwidth covers 1.2 to 2.3 μm, which is ideal for generating attosecond pulses with high photon energy. The 12 fs pulse duration correspond to about two optical cycles at 1.7 μm central wavelength. Such two-cycle pulses are not suitable for generating IAP. Proper gating method is required.

The different gating methods have been discussed and compared before in chapter 2.2. For our case, we choose the method based on polarization gating (PG) for 2 important reasons: First, PG works more efficiently when using a long wavelength driving laser. Second, PG can isolate the attosecond pulse in both the plateau and the cutoff spectrum region.

4.1 Parameter for polarization gating at 1.7 μm

The mechanism of polarization gating is discussed in detail in chapter 2.2.3. With a time varying ellipticity, HHG is only possible in a short time window where the E-field is linearly polarized. The time dependent ellipticity is given by equation 2.19. To evaluate quantitatively how the E-field ellipticity suppresses the HHG yield. an experiment (in chapter 4.1.1) is introduced to measure the threshold ellipticity that would suppress the HHG yield by 90%.

4.1.1 Ellipticity dependent HHG yield

Consider the three-step model for HHG process. In an elliptically polarized field, the tunneling ionized electron will be driven by the elliptically polarized filed. The transverse displacement introduced by the transverse E-field (equation 2.17, gating field for PG) will drive

the electron away from its parent ion and the electron does not recombine with the parent ion as a result. However, in quantum mechanics, the electron ionized from the atom should be treated as an electron wave packet rather than a single point charge [38]. The electric field accelerates the spreading electron wavepacket away from the parent ion and returns the wavepacket to the parent ion. Even if the field were elliptical, the returning spread electron wavepacket might spatially overlap with the parent ion and recombine with the parent ion and release a photon, albeit with yield corresponding to the degree of spatial overlap between the electron wavepacket and the parent ion.

Figure 4.1 shows an experiment to measure the ellipticity dependence of the HHG yield [37]. The 12 fs, 1.7 μm OPCPA pulse is focused (f=450 mm) into a neon gas cell to produce the high harmonic spectrum. The HHG signal is refocused by a nickel coated toroidal mirror with 86.5° incident angle. A 1200 line/mm soft x-ray diffraction grating (Shimadazu 03-005) is images the focus ontp the MCP phosphor screen and the soft X-ray spectrum on the MCP screen is recorded by an Andor sCOMS camera. An achromatic ¼ wave plate (Thorlabs AQWP10M-1600) is placed before the lens to control the field ellipticity. With the optical axis (fast or slow axis) parallel to the input polarization. The E-field after the ¼ wave plate is still linearly polarized. By rotating the ¼ plate with an small angle of θ, the resulted e-field became elliptically polarized with an ellipticity of tan(θ).
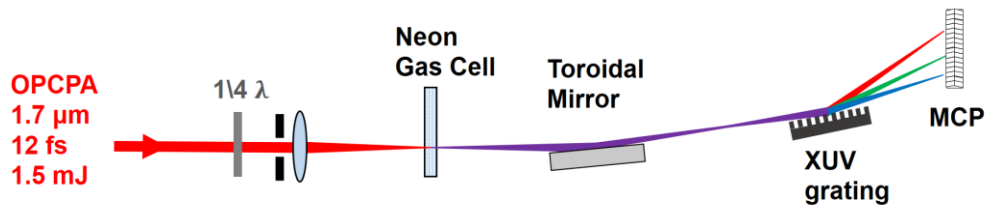
Figure 4.1 Experimental setup for measuring ellipticity dependent HHG yield.
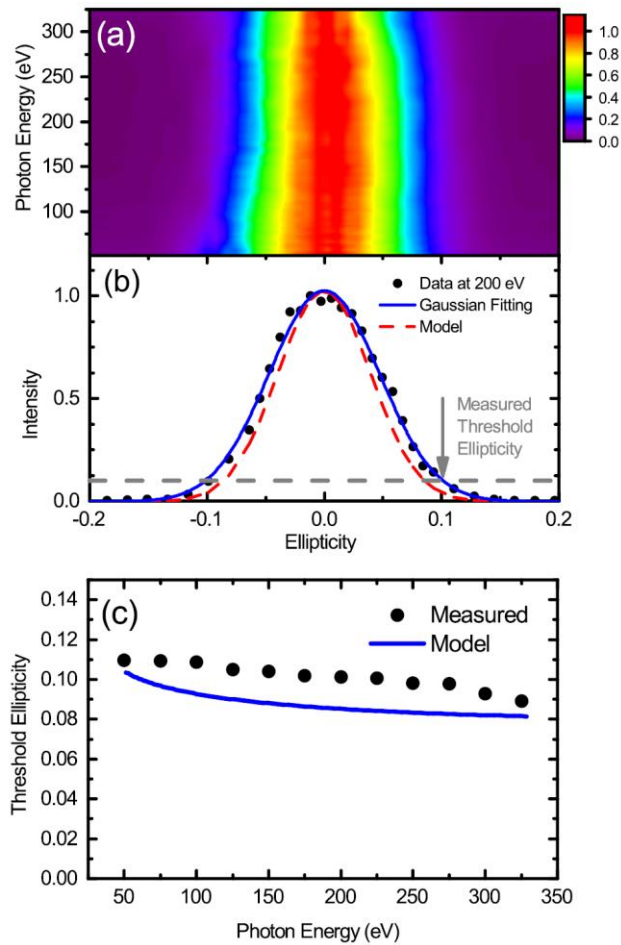
Figure 4.2 (a) Dependence of HHG yield on the driving laser ellipticity over the range of 50–325 eV; (b) dependence of HHG yield on the driving laser ellipticity at 200 eV (dot) with its Gaussian fitting (solid line); and (c) measured (dot) and calculated (solid line) threshold ellipticity at a field intensity of 5×10^{14}W/cm^2.

The experimental result is plotted in figure 4.2 (a). In this measurement, the difference between the p- and s-polarization grating efficiency is neglected because the rotation of the major axis of the driving field ellipticty is less than 10%, resulting in a relative error of only 3%. In figure 4.2 (a), the HHG yield reaches maximum when the field ellipticity of zero (linear polarized). The yield decrease with increase ellipticity. In order to determine the ellipticity adequate for suppressing the HHG yield. We define the threshold ellipticity ξ_{th} to be the ellipticity where the HHG yield decreases to 10%. In figure 4.2 (b), the data at 200 eV is plotted in black dots, since the ellipticity-dependent HHG yield follows a Gaussian shape in theory [38]. A Gaussin distribution curve is fitted to the 200 eV data. The calculated threshold ellipticity is $\xi = 0.1$ for 200 eV. Using the same method, we can calculate the experimental threshold ellipticity for other photon energies. The result is shown in figure 4.2 (c) with the theoretical prediction for comparison. The theoretical prediction is a semi-classical model that assumes that the HHG yield from an elliptical field is dominated by electrons with an initial transverse velocity that compensates for the transverse displacement introduced by elliptical field [40]. The theoretical prediction matchs with experimental result with about 20% difference. Both the experimental and theoretical result show a small variation of ξ_{th} over the 50-325 eV range. The value of ξ_{th} is mainly determined by driving field wavelength. For simplicity, $\xi_{th} = 0.1$ is used for calculating the polarization gating parameters at 1.7 μm central wavelength.

4.1.2 Polarization gate width using 1.7 μm field.

The time-dependent ellipticity for the polarization gating is given by equation 2.18 in chapter 2.2.3. At the middle of the polarization gating ($4In(2)T_d t\tau_p^{-2} \ll 1$), the field ellipticity can be approximated by equation 2.19:

$$\xi(t) = 2In(2)\frac{T_d}{\tau_p^2}|t|$$ (4.1)

$\xi(t) < \xi_{th}$ will ensure any eligible time t would allow HHG yield. The polarization gate width is therefore given by equation 2.20:

$$\delta t_G = \frac{\xi_{th}}{In(2)}\frac{\tau_p^2}{T_d}$$ (4.2)

where $\xi_{th} = 0.1$, and $\tau_p = 12$ fs. We ignore the difference between phase delay T_{Pd} and group delay T_{Gd} (equation 2.11 and 2.12) for small T_d, and the delay T_d can be simply set as $T_d = T_0, 2T_0, 3T_0$ .... The resulted polarization gate width $\delta t_{G1} = 3.6$ fs for one cycle delay ($T_d = T_0 = 5.6$ fs) and $\delta t_{G2} = 1.8$ fs for two cycle delay ($T_d = 2T_0 = 11.2$ fs). Since the HHG emits every half optical cycle, the polarization gate width should be less than half optical cycle $\delta t_G < \frac{T_0}{2} = 2.8$ fs to ensure that only efficient electron recombination happens inside the gate time ($-\frac{\delta t_G}{2} < t < \frac{\delta t_G}{2}$). It is then obvious that the two cycle delay case satisfy the requirement $t_{G2} = 1.8$ fs $< \frac{T_0}{2}$ while one cycle delay does not $t_{G1} = 3.6$ fs $> \frac{T_0}{2}$. This indicates that the one cycle delay PG will result in an incomplete gating.

4.2 Experiment comparison of PG gate width

To setup the PG experiment, a quartz plate is added into the beam path before the ¼ wave plate in figure 4.1. The quartz plate thickness is 180 μm (379 μm) for introducing one- (two-) cycle delay between o- and e-pulse. The optical axis of quartz plate is set at 45° for PG and 0° for linear polarization. The subsequent ¼ wave plate is set at 0°. The laser pulse energy and beam size is control simultaneously by an iris for maximizing the total HHG flux. The estimated laser

focus intensity is 5.5×10^{14} W/cm^2 for all cases. Figure 4.3 shows a comparison of the HHG

spectra produced using linearly polarized driving field and PG. Under linearly polarized field,

the HHG spectra are always discrete. This indicates that multiple attosecond pulses are generated

for each laser shot. For one cycle delay PG case, the spectra changes from continuous (CEP = -

0.05 π) to discrete-like (CEP = 0.45 π) in figure 4.3 (e). This indicates that the one cycle delay

PG gating has too large gate window and could result in double attosecond pulse with certain

CEP values. For the complete PG with two-cycle delay, the HHG spectra is always continuous

for all CEP values. This indicates that an IAP is generated for each laser shot. Another evidence

that an IAP is emitted per laser pulse is the large modulation in HHG spectra intensity as the

CEP is varied [35].
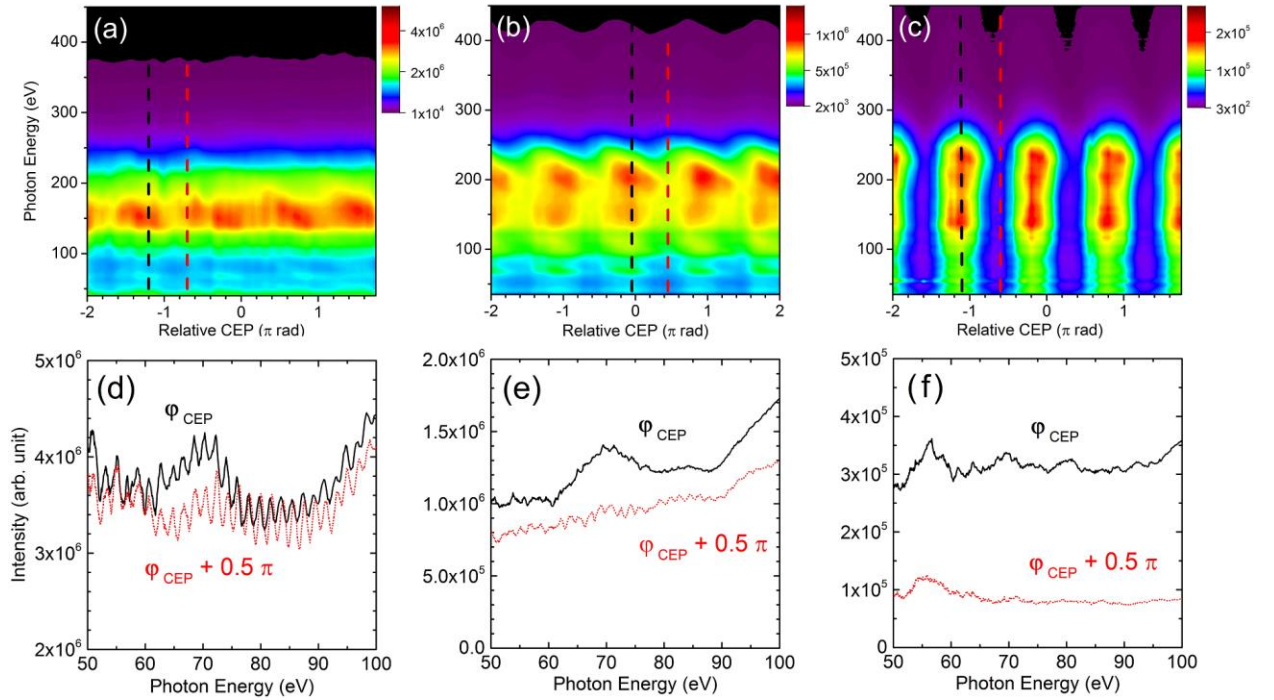
Figure 4.3 CEP influence on HHG spectra using (a) a linear driving pulse, (b) a PG pulse with one-cycle delay, and (c) a PG pulse with two-cycle delay; comparison of HHG spectra with CEP values differing by 0.5 π using (d) a linear driving pulse, (e) a PG pulse with one-cycle delay, and (f) a PG pulse with two-cycle delay. The spectra below 100 eV are shown where the resolution of spectrometer is sufficient to resolve harmonic peaks. The conditions of the MCP detector are kept the same so that the relative HHG flux in the three cases can be compared. Figure adopted from ref [37]

The two-cycle delay PG generates IAP at the cost of sacrificing a huge amount of photon flux. Figure 4.4 shows the relative photon flux for linear, one- and two-cycle delay PG. The number of x-ray photon in 100-400 eV range is measured with a XUV photodiode (IRD AXUV 100), which gives ~1.5×10^7 photons per laser shot after 100 nm Sn filter when using a linearly polarized driving field. The 100 nm Sn filter blocks the fundamental driving field.
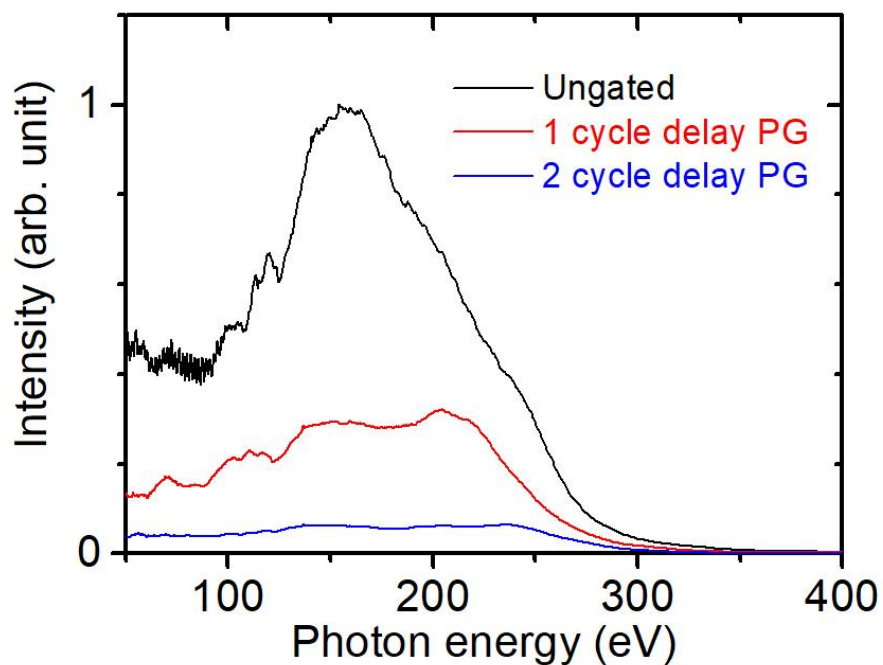
Figure 4.4 Photon flux compare between linearly polarized driving field and PG driving field. Iris size and gas cell position are re-optimized in each PG case for total flux.

The PG technique we introduced here for 1.7 μm wavelength driving field shows strong evidences (continuous spectrum & CEP dependent HHG yield) of generation IAP. To truly prove the generation of IAP and to fully characterize the IAP, attosecond streaking measurement is required. Which will be discussed in chapter 5.

CHAPTER 5 - CHARACTERIZATION OF SOFT X-RAY ATTOSECOND PULSES

To fully characterize an optical pulse, one wants to know the time domain electric field. However, it is technically difficult to measure the electric field directly since the electric field frequency ($\sim 10^{14}$ Hz) is too fast for any conventional detector to respond. By the principle of Fourier transform, one can also fully characterize the optical pulse in the frequency domain by knowing the spectrum and spectral phase. The FROG [59] technique is widely used to characterize femtosecond pulses. For the attosecond pulse discussed in chapter 4, it is difficult to characterize electric field using FROG technique since the flux of attoscond pulses is too low.

The technique used to characterize IAP is similarly based on the concept of measuring the spectrum in the frequency domain and its spectral phase. While the spectrum can be easily measured by XUV grating spectrometers, the spectral phase can be measured using attosecond streak camera technique [61]. In this chapter, the principle of attosecond streaking is discussed along with the corresponding experimental results. The Phase Retrieval by Omega Oscillation Filtering (PROOF) [62] algorithm for retrieving the phase is also discussed.

5.1 Principle of attosecond streak camera

The streak camera operates based on the idea of transforming a time varying signal into a spatial profile on a detector, by causing a time-varying deflection of the signal across the width of the detector [63]. Such an idea is similar to the operating principle of cathode ray oscilloscope. In a cathode ray oscilloscope, an unknown time varying electronic signal is applied to a vertical deflection plate where an electron beam passes through. The electron beam trajectory is deviated

by the time varyingelectric field applied in the vertical direction. A time synchronized sweep voltage is also applied to the horizontal deflection plates to resolve the time varying signal in the 2D. In this way, the unknown time varying electronic signal is mapped into vertical (signal strength) and horizontal (time) direction.

For measuring attosecond pulse, there is no electronic device that could provide sweep voltage in attosecond time scale. Instead, the fast oscillating electric field in an optical wave (phase locked with attosecond field) could be used as the sweep voltage for measuring the attosecond filed. This is the basic idea of attosecond streak camera [61].

In attosecond streaking, a weak attosecond pulse (XUV or x-ray) and a phase-locked IR pulse are focused together into the neutral gas. The relative delay τ_d between attosecond and IR pulse are well controlled. Figure 5.1 (a) shows a schematic drawing of attosecond and IR pulse overlapping in the neutral gas for attosecond streaking. The attosecond photons ionizes the ground state neutral gas to the continuum through single photon ionization. The IR field with a typically intensity of $\sim 10^{11}$-10^{13} W/cm^2 is relatively weak in field strength compared to the atomic Coulomb field. Since the IR field overlaps with the attosecond pulse, the free electrons generated at time t are streaked by the IR laser field. We assume the IR and attosecond field are both linearly polarized in the same direction and the measured electron kinetic energy spectrum is measured along the polarization direction. The IR field imparts a momentum $\Delta p(t)$ onto the free electron generated at time t_d have momentum change due to the IR streak field [61]:

$$\Delta p(\tau_d) = \int_{\tau_d}^{\infty} e\varepsilon_L(t')dt' = eA(\tau_d) \tag{5.1}$$

Where $\varepsilon_L(t)$ is the IR electric field, $A(t)$ is the vector potential of the IR filed and τ_d is the time delay between attosecond and IR pulse. Figure 5.1 (b) shows the attosecond streaking

photoelectron spectrogram as a function of the delay time τ_d. The spectrogram can be calculated quantum mechanically using strong field approximation (SFA)[64, 65]. In the SFA, the ground state electron is ionized directly promoted to the continuum states, bypassing all the excited states. Thus, the atomic resonance processes are ignored and only the ground state and the continuum states need to be considered.
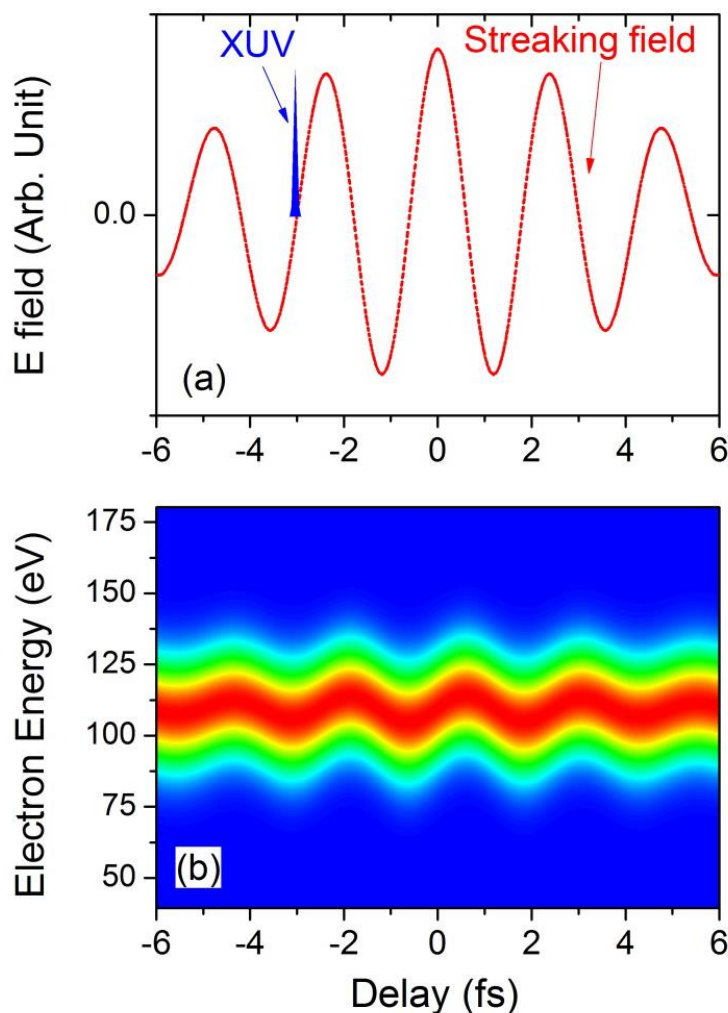
Figure 5.1 A schematic drawing depicting the principle of attosecond streaking (a) XUV (blue) and streaking field (red dashed) (b) The streaking photoelectron diagram obtained by scanning the delay between XUV and streaking field and recording photoelectron spectra at each delay.

When the neutral gas atom is placed in the field which is a sum of the attosecond $\varepsilon_X(t)$ and IR $\varepsilon_L(t)$. The time-dependent Schrödinger equation (TDSE) under the electric dipole approximation is:

$$i\frac{\partial}{\partial t}|\Psi(r,t)\rangle = [-\frac{1}{2}\nabla^2 + V(r) - \varepsilon_L(t)\cdot r - \varepsilon_X(t - \tau_d)\cdot r]|\Psi(r,t)\rangle \quad (5.2)$$

Where $|\Psi(r,t)\rangle$ is the electron wave function, $-\varepsilon_L(t)\cdot r$ and $-\varepsilon_X(t-\tau_d)\cdot r$ are the dipole moment of the electron in the IR and the attosecond field. The IR pulse is assumed to arrive at time zero and the attosecond pulse arrives with a time delay of τ_d.

After making the SFA, the solution to the equation 5.2 has an analytical solution:

$$|\Psi(r,t)\rangle = e^{-iI_pt}\left[|0\rangle + \int d^3\ b(v,t)|v\rangle\right] \quad (5.3)$$

Where $|0\rangle$ is the ground state wave function and $b(v,t)$ is the complex amplitude of momentum-space plane wave function $|v\rangle$ with electron momentum v. I_p is the ionization potential of the atom. The time dependent phase term e^{-iI_pt} is factored out of the continuum wave unction. The complex amplitude of continuum wave function at delay τ_d is given by [66]:

$$b(v,\tau_d) = -i\int_{-\infty}^{\infty} dt\ \varepsilon_X(t - \tau_d)d[v + A(t)]e^{i\varphi(v,t)}e^{-i(\frac{v^2}{2}+I_p)t} \quad (5.4)$$

$$\varphi(v,t) = -\int_t^{\infty} dt'[vA(t') + \frac{A^2(t')}{2}] \quad (5.5)$$

$d[v]$ is the complex dipole transition-matrix element from the ground state to the continuum state with momentum v. The energy and delay-dependent photoelectron spectrogram $S(v,\tau_d)$ in figure 5.1 (b) can be calculated from the amplitude of continuum wave function [65-67]:

$$S(v,\tau_d) = |b(v,\tau_d)|^2 \quad (5.6)$$

5.2 Attosecond streak camera Experiment

5.2.1 Experimental setup
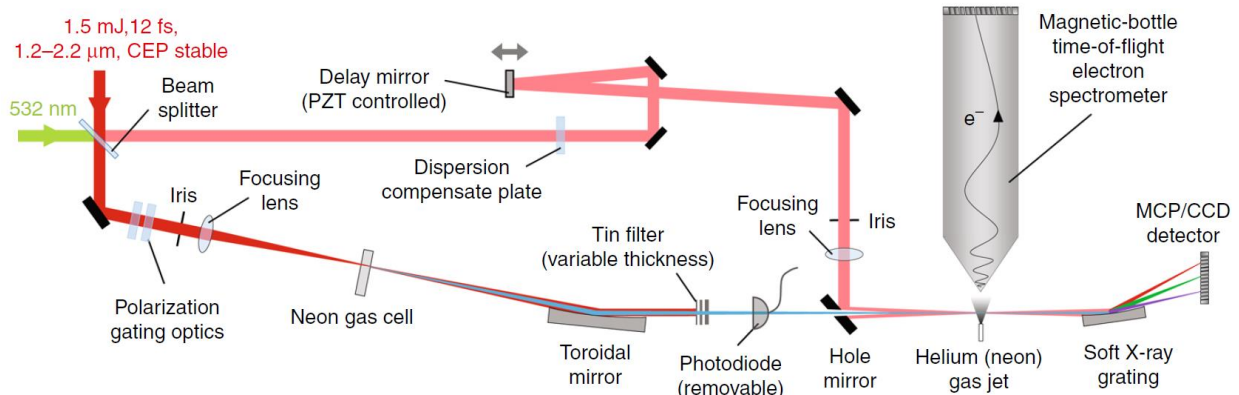
Figure 5.2 Experimental setup for attosecond streak camera. CCD: charge-coupled device; MCP: microchannel plate, PZT: piezo-electric transducer

A schematic illustration for the experiment setup for isolated attosecond pulse generation and characterization is shown in figure 5.2. The laser pulse energy available for this experiment is 1.5 mJ. The laser field is first split into two arms. The high energy (90% of the 1.5 mJ) arm passes through polarization optics. The pulse energy and beam size is controlled simultaneously by an iris placed right before a f=450 mm focus lens. The laser beam with a time dependent ellipticity is then loosely focused into a 1.5 mm long gas cell to generate isolated attosecond pulses in the soft x-ray region. The x-ray beam is then focused into a second gas jet by a nickel coated toroidal mirror with > 70% reflective efficiency for 100 -500 eV region using 86.5° incident angle. The fundamental driving field is filtered out by Tin filters. The negative dispersion from the Tin filters can partially compensate for the positive attochirp [68] in the X-ray region. The reflected streaking arm (10% of the 1.5 mJ) is recombined with the X-ray beam

by a hole drilled mirror and focused to the gas jet. A mirror mounted on a piezo-electric

transducer controls the relative time delay of the streaking arm. Helium gas is typically used to

suppress the background noise or multichannel contribution during the photon ionization [69].

The photoelectron spectrum is measured by a 3-meter-long magnetic-bottle electron time-of-

flight (TOF) spectrometer [70]. A soft X-ray grating spectrometer monitors the signal during our

experiment. For attosecond streaking, the delay τ_d between the attosecond and the streaking arm

need to controlled and stabled. A 532 nm CW beam is sent through from the other side of the

beam splitter. The reflected and transmitted 532 nm beams co-propagate with the attosecond and

streaking arm respectively. The interference fringes from the 532 nm beams after the hole mirror

are used to apply feedback to the delay mirror through the piezo-electric transducer to stabilize

the interferometer [71].

The PG technique mention in chapter 4.2 is a promising choice for generating IAP in X-

ray region. Both one and two-cycle delay PG produce HHG which have highly CEP dependent

HHG yield and have cutoff that is dependent on the CEP. These features strongly indicative of

the generation of IAP. With an attosecond streaking camera, we investigate the feasibility of

using one- and two-cycle delay PG.

5.2.2 One- and two-cycle delay PG comparison using attosecond streaking.

We first investigate one-cycle delay PG by using a 180 μm quartz plate. Figure 5.3 record

three streaking spectrograms using one-cycle delay PG with different CEP values. The streaked

photoelectron spectrogram in Figure 5.3 (a) shows a clear sinusoidal energy shift with a period of

T_0 caused by the streaking IR field. Upon changing the relative CEP value by only 0.2 π, half-

cycle streaking becomes obvious in the upward and downward side of the energy shift (Figure 5.3 (b)). Such a half-cycle energy shift is a signature of double attosecond pulses generated inside the polarization gate [72]. An even stronger half-cycle energy shift is observed when further changing the relative CEP value to $\Psi_{CEP} + 0.7\pi$. Therefore, one-cycle delay PG in our case can generate clean IAP in 100-300 eV region only with proper CEP values.
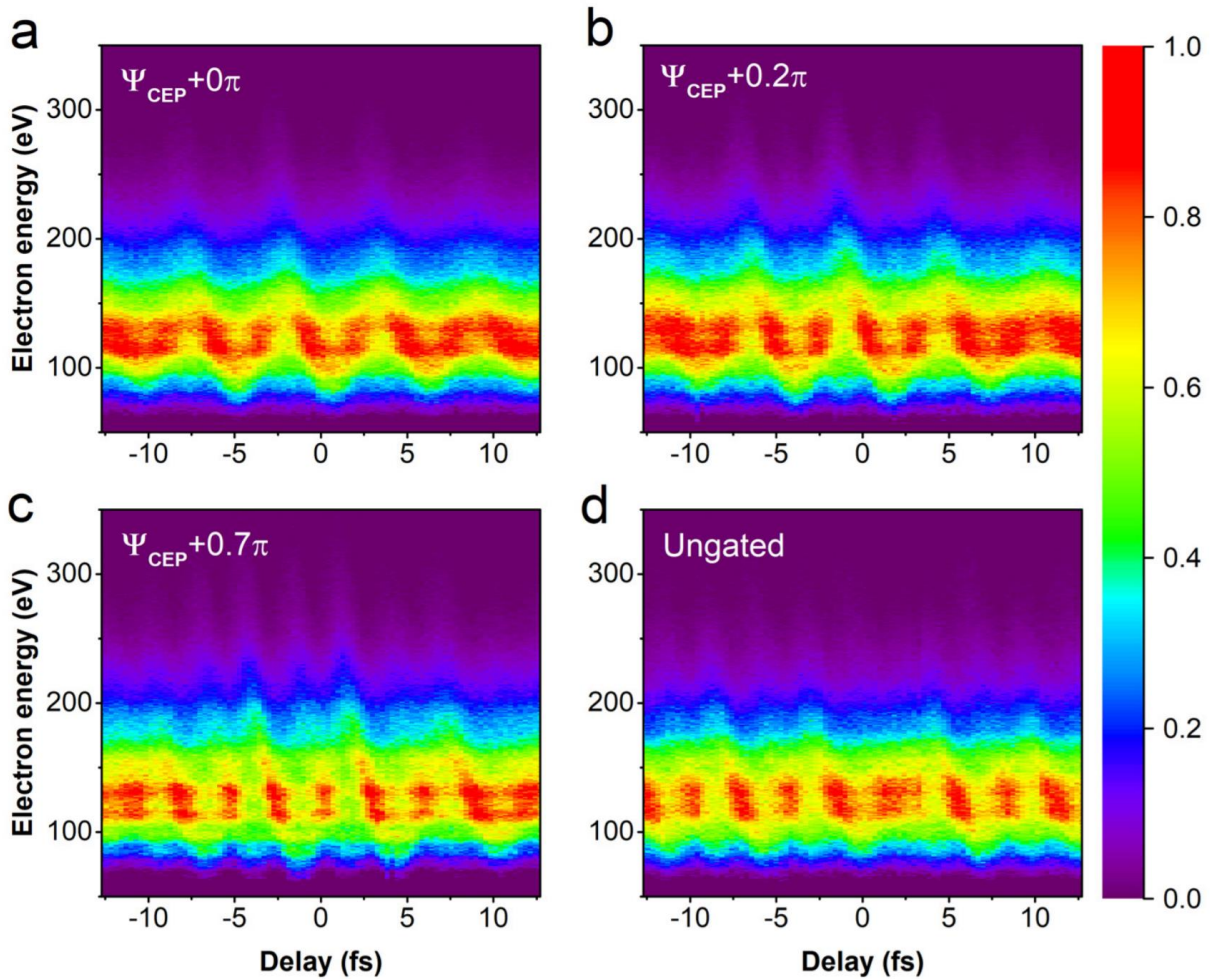
Figure 5.3 Carrier-envelope phase influence on PG. Experimental streaked photoelectron spectrograms using one-cycle delay PG (gate width δt_{G1}=3.6 fs) under different carrier-envelope phase (CEP) values (a to c), with the ungated case (d) shown for comparison. The fundamental IR field was filtered out using 100 nm tin filter for all cases. Neon is used here to generated photoelectron since Neon has a relatively high photoionization cross section [73].

We note that the photon flux with one-cycle delay PG (under proper CEP) is substantially higher than that with two-cycle delay (figure 4.4). The only drawback is the difficulty in finding an optimal CEP value for one-cycle delay PG since the CEP influence on HHG yield is weak compare when comparde to the two-cycle delay PG case (figure 4.3). Therefore, using one-cycle delay PG often results in a backward streaking with improper CEP value. Due to this reason, the two-cycle delay PG is preferred for our attosecond streaking experiment. Although the corresponding X-ray flux produced is three times lower than the flux produced using an one-cycle case, it is easier to find an optimal CEP value for achieving cleaner IAP. Figure 5.4 (a) shows the attosecond streaking spectrogram using Neon as detection gas. A 100 nm Tin filter is applied to block the IR field in the attosecond arm. The trace shows a clear sinusoidal energy oscillation. The backward streaking in the low energy side (near 80 eV) is barely noticeable in figure 5.4 (a), whereas backward streaking is much more obvious in figure 5.3 (a). This is further indication that two-cycle delay PG generates much cleaner IAP since the lower energy harmonics are far easier to generate with inadequate gating (see figure 2.7). Figure 5.4 (c) and (d) shows the attosecond pulse's spectral and temporal domain information retrieved from (a) using Phase Retrieval by Omega Oscillation Filtering (PROOF) [62] method, which is developed by our group. The principle of PROOF is discussed in the next section.
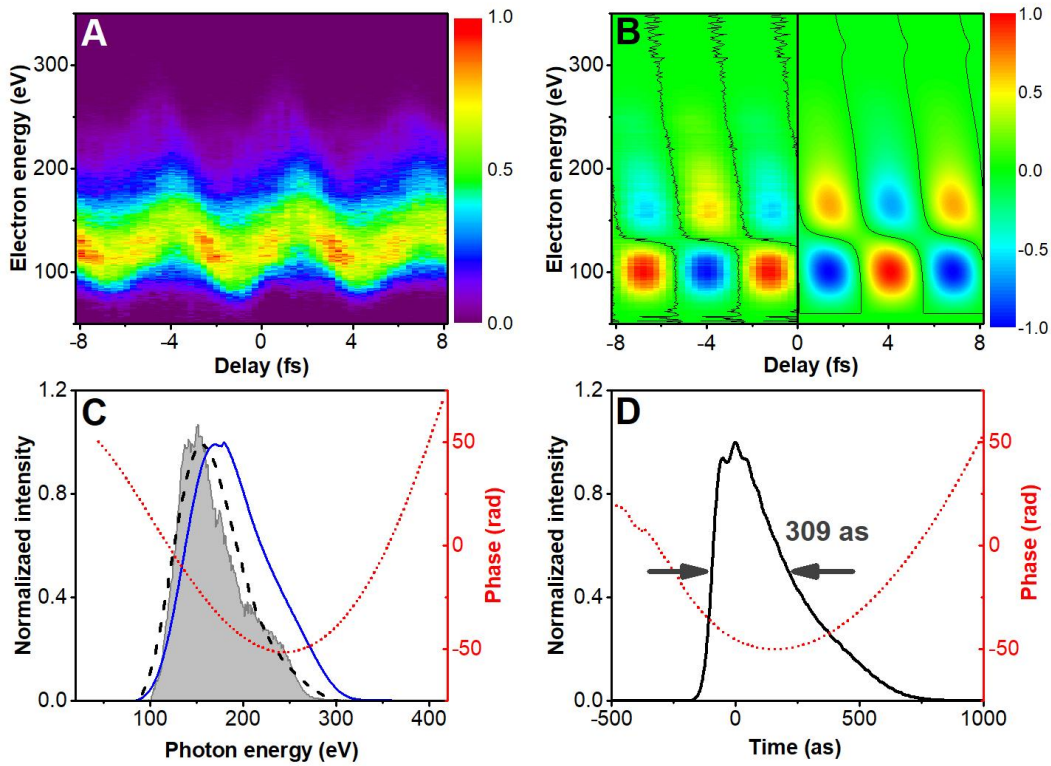
Figure 5.4 PROOF retrieved 309 as soft X-ray pulse. (a) Photoelectron spectrogram as a function of temporal delay between the soft X-ray and the streaking IR pulses in the case of a 100-nm-thick tin filter. A negative delay corresponds to an earlier IR pulse arrival. (b) Filter S_{ω_L} trace (−5 to 0 fs) from the spectrogram in (a) and the retrieved S_{ω_L} trace (0–5 fs). (c) Experimentally recorded (gray shade) and PROOF-retrieved spectra (black dash) by adding Neon photoionization potential (21.5 eV); corrected photon spectrum (blue solid), and spectrum phase (red dot) from PROOF. (d) Retrieved temporal intensity profile and phase of the 309 as pulses.

5.2.3 Phase Retrieval by Omega Oscillation Filtering (PROOF)

The technique we use to retrieve the attosecond field information from attosecond streak spectrogram is called PROOF technique [62]. PROOF technique requires only modest dressing laser intensity and can work with broadband spectrum.

The electric field of a linearly polarized isolated attosecond pulse can be described by the Fourier transform

74

$$\varepsilon_X(t) = \int_{-\infty}^{\infty} d\omega \ U(\omega)e^{i\varphi(\omega)}e^{i\omega t} \tag{5.7}$$

where the $U(\omega)$ and $\varphi(\omega)$ are the spectrum amplitude and spectrum phase respectively. It is easy to measure the power spectrum $I(\omega) = |U(\omega)|^2$, and only the spectrum phase $\varphi(\omega)$ is needed to fully describe the pulse. The spectral phase encoded in the streaking spectrogram can be determined using PROOF by utilizing the quantum interference of continuum states caused by the dress laser [65]. The interference between those states causes the electron signal at a given energy to oscillate with the delay between the attosecond and the IR field. Such sinusoidal oscillation is governed by the amplitude and phase of each of the interfering spectrum components. Figure 5.5 illustrate the principle of PROOF.

The amplitude of the electron wave function with momentum v and emitted at delay τ_d is given by equation 5.4 and 5.5. We assume the IR laser is close to monochromatic.

$$\varepsilon_L(t) = E_L \cos(\omega_L t) \tag{5.8}$$

The vector potential then becomes

$$A_L(t) = -\frac{E_L}{\omega_L}\sin(\omega_L t) \tag{5.9}$$

The phase modulation to the electron wave in equation 5.5 becomes

$$\varphi(v,t) = -\int_t^{\infty} dt' \left[vA(t') + \frac{A^2(t')}{2} \right] \approx \frac{vE_L}{\omega_L^2}\cos(\omega_L t) = \frac{vE_L}{2\omega_L^2}(e^{i\omega_L t} + e^{-i\omega_L t}) \tag{5.10}$$

Here we assume only the electron moving along the laser e-field direction are detected. And the IR filed intensity is low $\frac{vE_L}{\omega_L} << \omega_L$. We then use approximation: $e^{i\varphi(v,t)} \approx 1 + i\varphi(v,t)$, and the amplitude of electron wave packet from equation 5.4 becomes

$$b(v,\tau_d) \propto \int_{-\infty}^{\infty} dt \ \varepsilon_x(t-\tau)\left[1 + i\frac{vE_L}{2\omega_L^2}(e^{i\omega_L t} + e^{-i\omega_L t})\right]e^{-i(\frac{v^2}{2}+I_p)t} \tag{5.11}$$

Substituting equation 5.7 into the integral in equation 5.11 and using the property of delta function $\int_{-\infty}^{\infty} dt\, e^{i\omega t} = \delta(\omega)$, we have

$$b(v,\tau_d)e^{i\omega_v\tau_d} = U(\omega_v)e^{i\varphi(\omega_v)} + i\frac{vE_L}{2\omega_L{}^2}[U(\omega_v + \omega_L)e^{i\varphi(\omega_v+\omega_L)}e^{-i\omega_L\tau_d} +$$

$$U(\omega_v - \omega_L)e^{i\varphi(\omega_v-\omega_L)}e^{i\omega_L\tau_d}] \tag{5.12}$$

Where $\omega_v = \frac{v^2}{2} + I_p$ is the angular frequency of the attosecond photon. The streaking photoelectron spectrogram have three major components $S(v,\tau_d) = |b(v,\tau_d)|^2 \approx S_0 + S_{\omega_L} +$

$S_{2\omega_L}$ where S_0 is the DC components that did not change with the delay, $S_{2\omega_L}$ oscillates with

$2\omega_L$. We are interested in S_{ω_L} which oscillates with the IR laser frequency ω_L.

$$S_{\omega_L}(v,\tau_d) = \frac{vE_L}{\omega_L{}^2}\, U(\omega_v)[U(\omega_v + \omega_L)\sin(\omega_L\tau_d + \varphi(\omega_v) - \varphi(\omega_v + \omega_L)) -$$

$$U(\omega_v - \omega_L)\sin(\omega_L\tau_d - \varphi(\omega_v) + \varphi(\omega_v - \omega_L))] \tag{5.13}$$
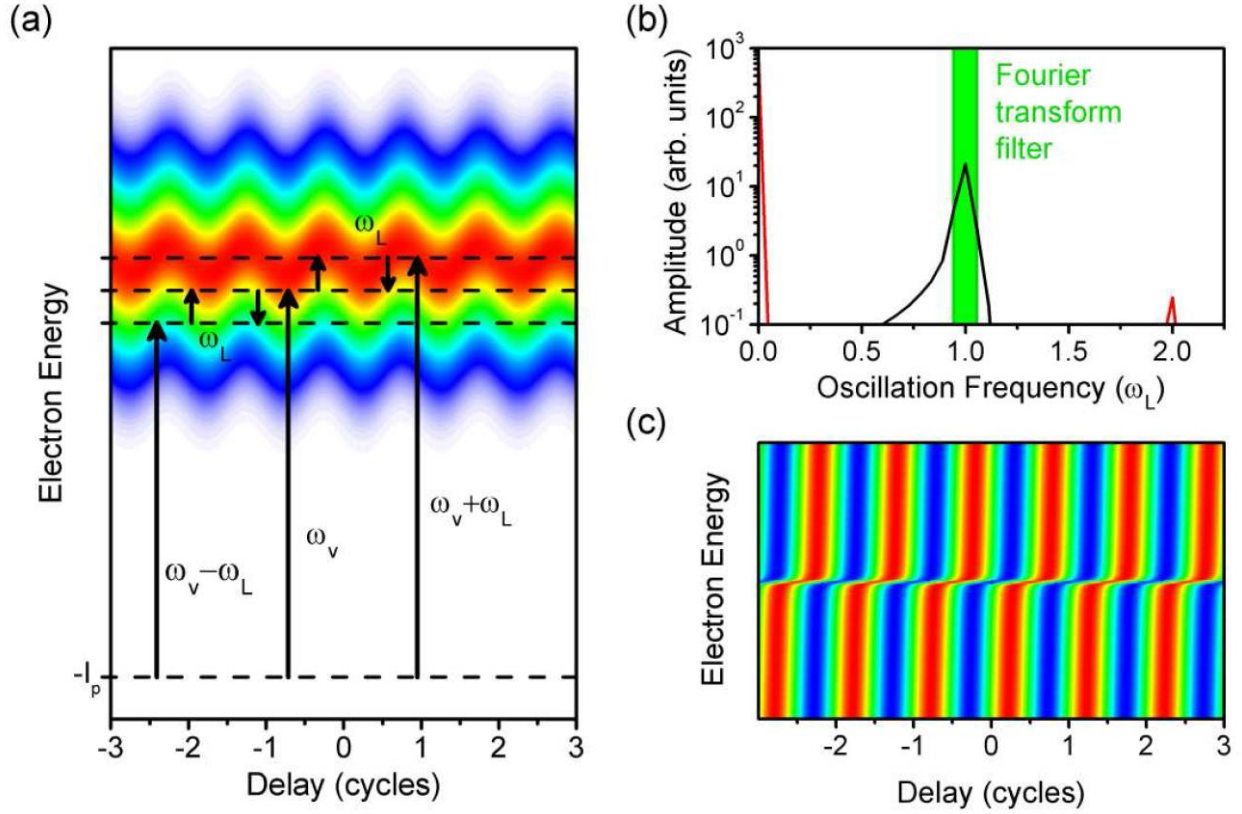
Figure 5.5 Principle of PROOF. (a) The isolated attosecond pulse photoionizes the electrons to continuum states. Those continuum states separated by the IR laser central frequency ω_L are coupled by the dress laser, leading to the characteristic oscillation of the photoelectron signal with delay. (b) Fourier transform amplitude of the signal from one electron energy in (a). Peaks are found at oscillation frequencies of zero (red line), ω_L (black line), and $2\omega_L$ (red line). The ω_L component is selected using a filter. (c) Spectrogram obtained by inverse Fourier transform of the filtered ω_L component of the oscillation, from which the phase angle $\alpha(v)$ can be extracted.

We can see more clearly that the laser frequency oscillation (LFO) component S_{ω_L}

indicates that the signal at momentum v is the result of interference between the two photon

transition pathway to the final state with momentum v. Equation 5.13 can be rewritten as:

$$S_{\omega_L} = |U(\omega_v)|^2 \frac{vE_L}{\omega_L{}^2} \gamma \sin(\omega_L \tau_d + \alpha) \qquad (5.14)$$

Where

$$\gamma^2 = \frac{1}{I(\omega_v)}\{I(\omega_v + \omega_L) + I(\omega_v - \omega_L) - 2\sqrt{I(\omega_v + \omega_L)I(\omega_v - \omega_L)}\cos[2\varphi(\omega_v) -$$

$$\varphi(\omega_v + \omega_L) - \varphi(\omega_v - \omega_L)]\} \tag{5.15}$$

The modulation depth of the oscillation is given by $\frac{vE_L}{\omega_L{}^2}\gamma$, and

$$\tan[\alpha] = \frac{\sin[\varphi(\omega_v)-\varphi(\omega_v+\omega_L)]-\frac{\sqrt{I(\omega_v-\omega_L)}}{\sqrt{I(\omega_v+\omega_L)}}\sin[\varphi(\omega_v-\omega_L)-\varphi(\omega_v)]}{\cos[\varphi(\omega_v)-\varphi(\omega_v+\omega_L)]-\frac{\sqrt{I(\omega_v-\omega_L)}}{\sqrt{I(\omega_v+\omega_L)}}\cos[\varphi(\omega_v-\omega_L)-\varphi(\omega_v)]} \tag{5.16}$$

is the tangent of the phase angle of the LFO. The spectrum phase is encoded in both the

modulation depth and phase angle. Figure 5.6 shows the modulation depth and phase angle

of the filtered spectrogram from two pulses with the same power spectrum but different

spectrum phases. The unknown spectrum phase can be obtained from the modulation

amplitude γ and phase angle α by solving coupled equation 5.15 and 5.16. However, for

experimental trace with low signal-to-noise ratio, it is more practical to retrieve the

spectrum phase numerically.
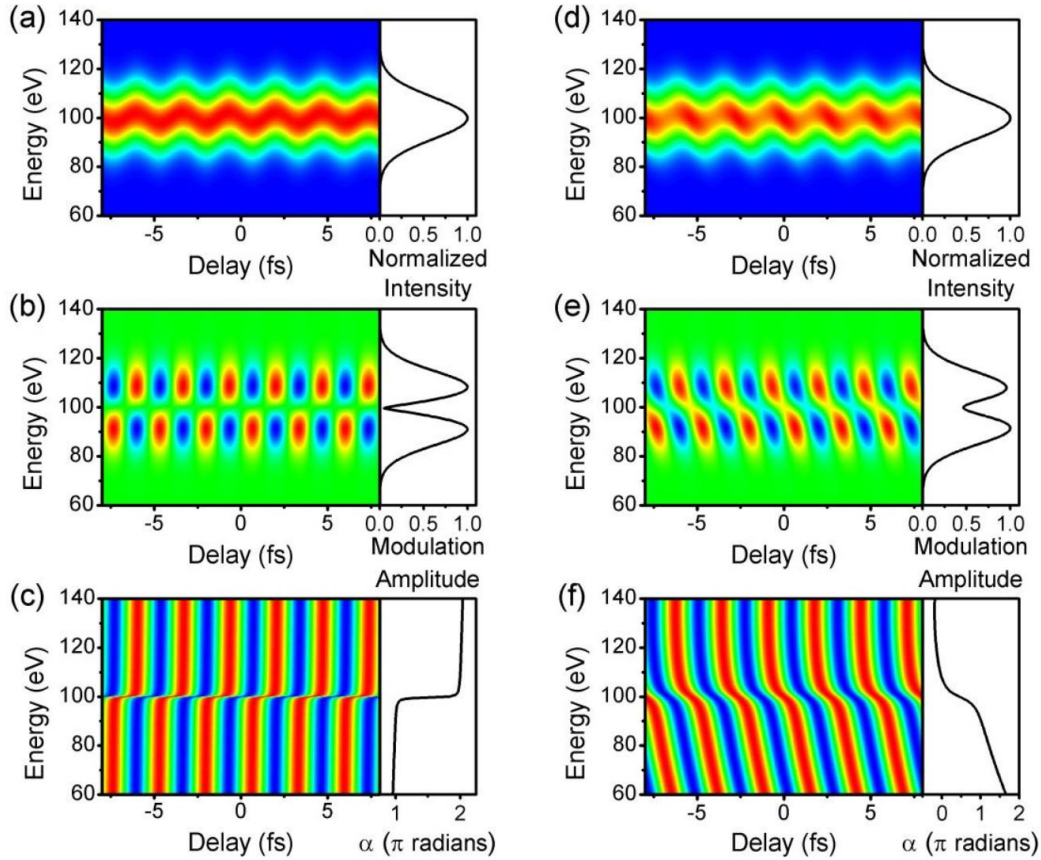
Figure 5.6 Extraction of the modulation amplitude and phase angle from the spectrogram for (a-c) a nearly transform-limited 95 as pulse and (d-f) a strongly-chirped 300 as pulse. (a, d) (left) Laser-dressed photoionization spectrogram and (right) attosecond pulse power spectrum. The two spectra are identical. (b, e) (left) Filtered LFO component and (right) extracted modulation amplitude. (c, f) Filtered LFO, normalized to the peak signal at each electron energy and (right) extracted phase angle.

5.2.4 Retrieval procedure in PROOF

In PROOF, the spectrum and phase of the attosecond photoelectron burst are retrieved using an iterative algorithm, the goal of which is to minimize the error between the component of the experimental spectrogram oscillating with the laser frequency S_{ω_L}, and a "guessed" trace, given by equation 5.14. $S_{\omega_L}(v, \tau_d)$ can be written as the product of two components: a modulation amplitude $\gamma(v)$ and the laser-frequency oscillation component $\sin(\omega_L \tau_d + \alpha)$, where $\alpha(v)$

79

describes the phase of the oscillation. Both $\gamma(v)$ and $\alpha(v)$ depend on (and can be calculated from) the spectral amplitude and phase of the attosecond burst. In the algorithm, the error between the experimental and "guessed" $\gamma(v)$ and $\alpha(v)$ are separately minimized, in an iterative fashion. The algorithm proceeds as follows:

1) Initialization: Let the spectral amplitude of the attosecond photoelectron burst be given by $U(v) = S_0^{1/2}$, where S_0 is the DC Fourier component of the experimental spectrogram. This is a very accurate guess when the streaking intensity is low. However, it must be refined by further iteration (step 3 below) under practical experimental conditions. To avoid introducing noise into the algorithm, the spectrum is smoothed using a cubic spline fitting function.

2) Phase optimization: Guess the spectral phase of the attosecond burst $\varphi(\omega_v)$ which minimizes the error function between the experimentally-obtained phase angle $\alpha(v)$ and that calculated from the guessed $U(v)$ and $\varphi(\omega_v)$. For this step, the value of the phase at each electron energy is allowed to vary between 0 and 2π, and the spectral phase function $\varphi(\omega_v)$ is obtained by unwrapping the phase and applying a cubic spline fitting before evaluating the error function, in order to avoid introducing noise into the algorithm.

3) Spectrum optimization: Guess the spectral amplitude of the attosecond burst $U(v)$ which minimizes the error function between the experimentally-obtained modulation amplitude $\gamma(v)$ and the calculated using the guessed $U(v)$ and $\gamma(v)$. For this step, the value of the amplitude is allowed to vary freely, and the spectral amplitude function $U(v)$ is obtained

by applying a cubic spline fitting before evaluating the error function, in order to avoid introducing noise into the algorithm.

4) Repeat steps 2 and 3 iteratively. After each iteration, evaluate the error function between the experimentally obtained laser-frequency filtered spectrogram $S_{\omega_L}(v, \tau_d)$ and the calculated one using the guessed $U(v)$ and $\varphi(\omega_v)$. Once the error has decreased to a suitable value, stop the loop and export the guessed $U(v)$ and $\varphi(\omega_v)$.

5) Apply the dipole correction to the guessed $U(v)$ and $\varphi(\omega_v)$ to obtain the attosecond photon pulse spectrum and phase.

The metrics used to evaluate the accuracy of the retrieval are therefore dependent on the degree of agreement between the filtered spectrogram $S_{\omega_L}(v, \tau_d)$ and that the calculated spectrogram using the guessed $U(v)$ and $\varphi(\omega_v)$, as well as the degree of agreement between the measured and guessed photoelectron spectrum. The PROOF technique and the iterative retrieval processes were applied to experiment data in figure 5.4 (a). The agreement between experimentally filtered and retrieved LFO in figure 5.4 (b) is excellent.

5.3 Compensating the attochirp

The retrieved attosecond pulse duration is 309 as (figure 5.4 (d)). A clear positive chirp can be found from the quadratic phase in figure 5.4 (c) and (d). The chirp comes from the intrinsic attochirp arising from the HHG process [68]. Usually, only the short trajectory HHG is phase-matched in the experiment. The chirp from short trajectory emission is positive, which can

be compensated by the negative dispersion of metallic filters. We choose tin filter to compensate the attochrip for 100-300 eV range. Figure 5.7 shows the transmission and GDD from 100 nm tin filter. We can find that the GDD of tin filter approaches zero at 300 eV. Which means effective attochirp compensation is only possible for photon energy < 200 eV. Our soft x-ray photon spectrum (100-300 eV) is peaked at 170 eV. The major attochirp component (GDD) can be effectively compensated by thicker filters.
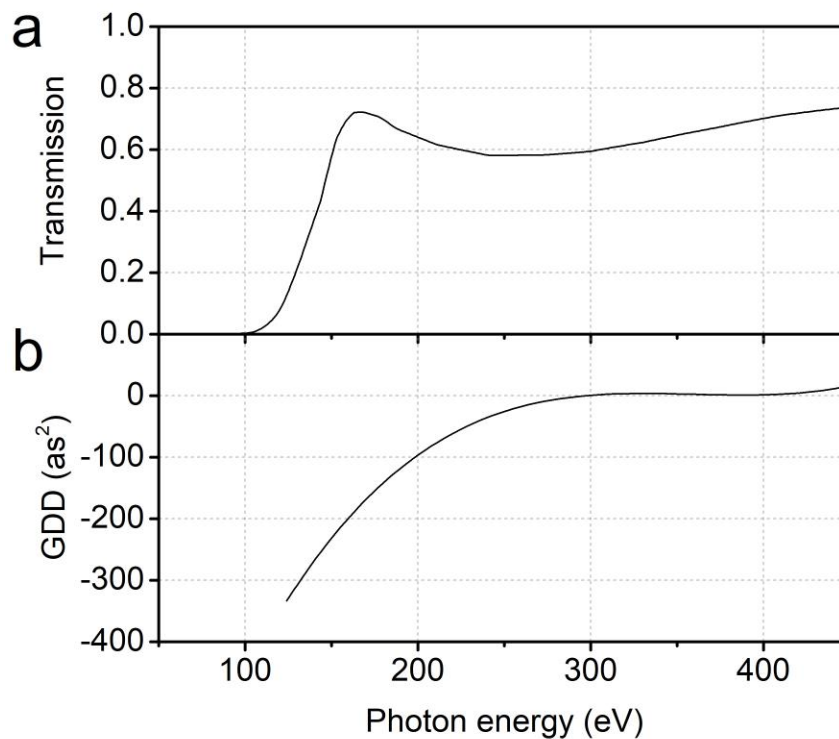
Figure 5.7 Calculated transmission (a) and group delay dispersion (GDD) (b) of 100 nm tin filter.

Neon gas was first used as a detection gas due to its relatively-large absorption cross-section when compared to helium. It should be note that the neon 2p and 2s orbitals will contribute to our photoelectron signal [73]. For our spectrum range, the cross section for neon 2p and 2s only differs by a factor of two near 300 eV (figure 5.8), which means our photoelectron

signal will have substantial amount of contribution from the 2s orbital. Moreover, previous

studies have suggested that the photon emission from neon 2p and 2s orbitals has a time delay in

the order of tens of as [74]. Such multichannel contribution will affect the spectrum

measurement and phase retrieval. However, the relative reduction of attochirp with thicker tin

filters can clearly be observed in our streaking experiment using neon gas (figure 5.9). More

accurate measurements of the pulse duration will require the use of helium gas at the cost of

reduction of photoionization cross section and thus poor signal to noise ratio.
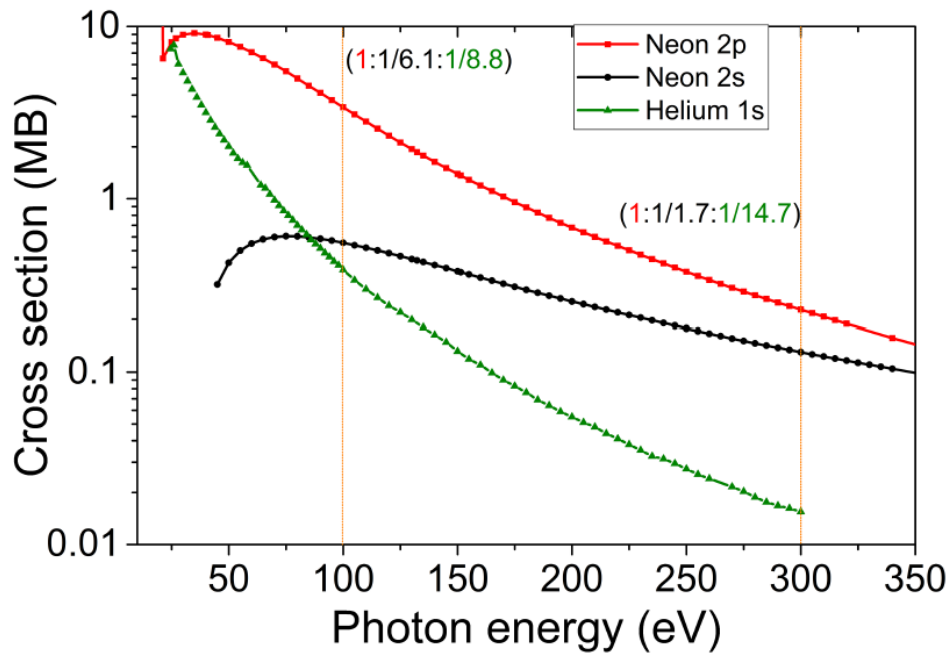
Figure 5.8 Photoionization cross section from Neon 2p, Neon 2s and Helium 1s orbitals in the experimental photon energy range. At 100 eV, the ratios of the cross section between these three orbitals are 1:1/6.1:1/8.8, at 300 eV, the ratio becomes 1:1/1.7:1/14.7.

The retrieved attosecond pulse durations versus tin filter thickness is shown in figure 5.9.

We tested several filter thickness to find the optimal filter thickness for attochirp compensation.

There is a clear trend of decreasing pulse duration with increasing the filter thickness as the

thickness of the filter rose from 100 nm to 400 nm. Increasing the thickness to 500 nm would instead lead to an overcompensated attochirp on the low energy side, resulting in a slightly increased pulse duration. To test the repeatability of our measurement, multiple measurements were performed at 400 nm, 450 nm and 500 nm and the results were in agreement with each other.
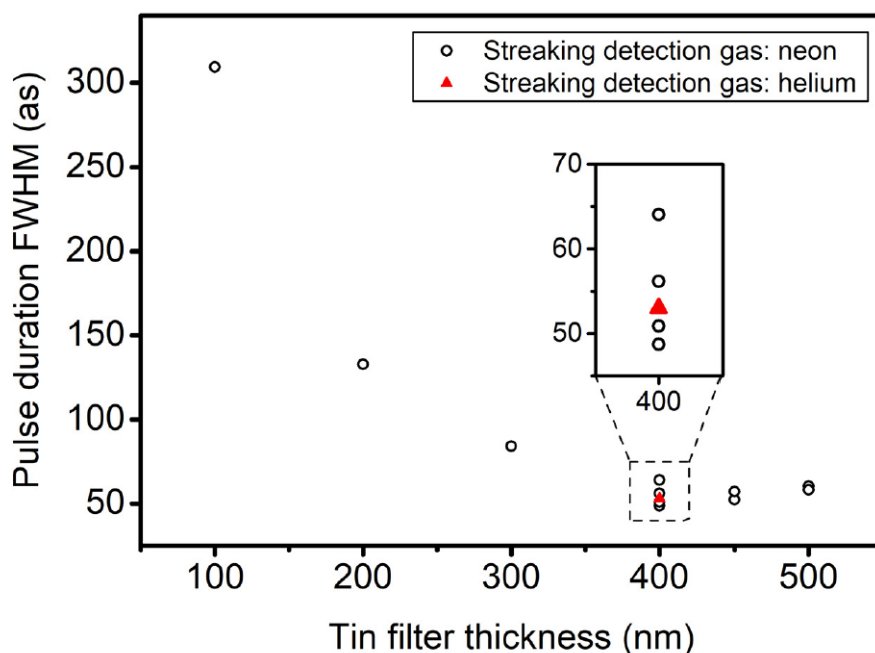
Figure 5.9 PROOF-retrieved attosecond pulse duration with dipole correction at different tin filter thickness.

As a result of using neon gas as the detection gas, the main error comes from 2s electron contribution which would mostly affect the electron spectrum lineshape. To avoid any multichannel contributions, we measured the photoelectron signal with helium detection gas. Figure 5.10 shows a PROOF retrieved pulse duration of 53 as, which agrees reasonably well with the results obtained using neon detection gas at 400 nm filter thickness. Since the attochirp

is above 200 eV is difficult to compensate (figure 5.7), the measured 53 as pulse has a residual

TOD. This can be evidently seen in figure 5.10 (c) where the spectrum phase has a cubic shape.

The transform limited pulse duration calculated from the corrected photon spectrum is 20 as.
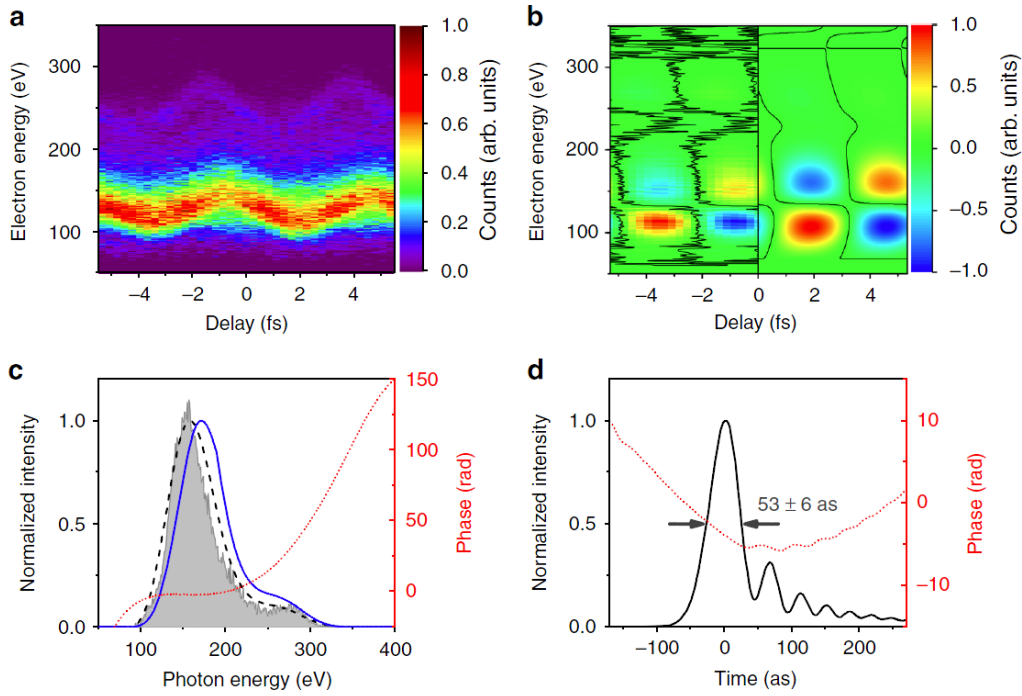
Figure 5.10 PROOF retrieved 53 as soft X-ray pulse. (a) Photoelectron spectrogram as a function of temporal delay between the soft X-ray and the streaking IR pulses in the case of a 400-nm-thick tin filter. A negative delay corresponds to an earlier IR pulse arrival. (b) Filter S_{ω_L} trace (−5 to 0 fs) from the spectrogram in (a) and the retrieved S_{ω_L} trace (0–5 fs). (c) Experimentally recorded (gray shade) and PROOF-retrieved spectra (black dash) by adding helium photoionization potential (24.6 eV); corrected photon spectrum (blue solid), and spectrum phase (red dot) from PROOF. (d) Retrieved temporal intensity profile and phase of the 53 as pulses.

CHAPTER 6 - CONCLUSIONS AND OUTLOOK

In my thesis, I mainly discussed the techniques to generate and characterize isolated attosecond pulses in the soft X-ray spectrum range.

In chapter 2, I presented the principle of high harmonic generation and different gating techniques to isolate the attosecond pulses. The advantages and limitations of each gating techniques were compared. Chapter 3 discussed the requirement of extension HHG cutoff by using longer wavelength diving field. An OPCPA laser system delivering 3-mJ, CEP-stabled, 2-cycle pulse at 1.7 micron wavelength was discussed in detail. A novel phase match method was proposed to ensure broad parametric amplification bandwidth with high pump-to-signal conversion efficiency. Because high harmonic generation is sensitive to driving field ellipticity. Polarization gating is more effective when using longer wavelength laser. In Chapter 4, a two-cycle delay polarization gating was chosen to generated clean isolated attosecond pulses in 50-350 eV range. The intrinsic chirp of the attosecond pulses was measured by attosecond streak camera and retrieved using PROOF technique. Sn metal filters were applied to compensate the attochirp and 53-attosecond pulses were achieved in 100-300 eV spectrum range. We also demonstrated that the 53-attosecond pulse duration was limited mainly by uncompensated third order dispersion.

As long wavelength femtosecond technology become more widespread, attosecond pulses with photon energy exceeding 300 eV become easier to access. Even KeV attosecond pulses are expected when using mid-IR driver. The intrinsic attochirp is inversely proportional to the driving wavelength. Combine with its broadband spectrum, shorter attosecond pulse duration can be expected with proper phase compensation.

86

APPENDIX A- CODE FOR CALCULATE DELAY IN POLARIZATION

GATING

```
$root = NotebookDirectory[]; (*same file directory for readin and write file*)
c = UnitConvert[Quantity["SpeedOfLight"]][[1]]; $TextStyle = {"Arial", 14};
fs = 10^-15; nm = 10^-9;
Time = 40; (*time plot range*)
LSiO2 = 379 / 10^6; (*thickness L of quartz in meter*)

no[ω_] :=
  Sqrt[1 + 0.28604141 + 1.07044083 / (1 - 0.0100585997 / (1 000 000 * (2 * Pi * c / ω))^2) +
    1.10202242 / (1 - 100 / (1 000 000 * (2 * Pi * c / ω))^2)];
ne[ω_] := Sqrt[1 + 0.28851804 + 1.09509924 /
      (1 - 0.0102101864 / (1 000 000 * (2 * Pi * c / ω))^2) +
    1.15662475 / (1 - 100 / (1 000 000 * (2 * Pi * c / ω))^2)];

φo[ω_] := LSiO2 * ω * no[ω] / c;
φe[ω_] := LSiO2 * ω * ne[ω] / c;

(* Import the data files and extract the relevant information *)
raw1 = Import[$root <> "spectrum.txt", "Table"];
(*ListPlot[raw1[[All,2]],PlotRange→All,Frame→True,Axes→False]*)
λ = raw1[[1 ;; Length[raw1], 1]] nm; Iλ0 = raw1[[1 ;; Length[raw1], 2]];
Iλ1 = Iλ0 - Min[Iλ0]; (*All spectrum value is positive,
subtract the minmun to reduce noise*)

(*ListPlot[Iλ1,PlotRange→All,Frame→True,Axes→False]*)
norm = Max[Iλ1]; Iλ1 = Iλ1 / norm; (* Nomalization *)
(*ListPlot[Iλ1,PlotRange→All,Frame→True,Axes→False]*)
(*ListPlot[Transpose[{λ/nm,Iλ1}],PlotRange→All,Frame→True,
 Axes→False,Joined→True,PlotStyle→{{PointSize[1],Red}},
 LabelStyle→$TextStyle,FrameLabel→{"λ (nm)", "I(λ) (a.u.)","Raw Data"}]*)

threshold = 0;
Iλ1 = Chop[Iλ1, threshold];

chopplot = ListPlot[Transpose[{λ / nm, Iλ1}], PlotRange → All, Frame → True,
   Axes → False, Joined → True, PlotStyle → {{PointSize[0.005], Red}},
   LabelStyle → $TextStyle, FrameLabel → {"λ (nm)", "I(λ) (a.u.)", "chopped"}]

(* Change from Wavelength to Frequency *)
ω = 2 π c / λ;
Aω1 = Transpose[{ω, Abs[Iλ1] - Min[Abs[Iλ1]]}];
(*OriginalPlot=ListPlot[{Aω1},PlotRange→{All,All},Frame→True,
   Axes→False,Joined→True,PlotStyle→{{Thickness[0.005],Blue}},
   LabelStyle→{FontFamily→"Arial",FontSize→14},FrameLabel→{"ω ","A(ω)"}]*)

(* Fit function A(ω) *)
Off[InterpolatingFunction::"dmval"];
Aωint1 = Interpolation[Aω1, InterpolationOrder → 1];

(* Resample from the interpolation function
```

```
 to obtain even spacing in ω for the FFT function *)
n = 2^14; (* must be even will define time step later*)
add = 0.01; (*define ω reading space*)
ω1 = Min[ω]; ω2 = Max[ω];
ωnew = Table[ω1 + (ω2 - ω1) * i, {i, 0, 1, add}];

(*Specplot=Table[Spectrum[ω1+(ω2-ω1)*m],{m,0,1,add}];*)
Aω1resample = Table[If[ωnew[[i]] ≤ Max[ω] && ωnew[[i]] ≥ Min[ω],
     Aωint1[ωnew[[i]]], 0], {i, 1, 1 / add}];
Specplot = Aω1resample;
Specplot = PadLeft[Specplot, Round[(1 / add) * ω2 / (ω2 - ω1)]];
(**** !!!very important!!! ****)

phaseploto = Table[ϕo[ω1 + (ω2 - ω1) * i], {i, 0, 1, add}];
phaseploto = PadLeft[phaseploto, Round[(1 / add) * ω2 / (ω2 - ω1)]];
phaseplote = Table[ϕe[ω1 + (ω2 - ω1) * i], {i, 0, 1, add}];
phaseplote = PadLeft[phaseplote, Round[(1 / add) * ω2 / (ω2 - ω1)]];

(* Specplot=Table[Spectrum[ω1+(ω2-ω1)*m],{m,0,1,add}]; *)
(* phaseplot=Table[ϕ[ω1+(ω2-ω1)*l],{l,0,1,add}];   *)
compo = Abs[Sqrt[Specplot]] * Exp[I * phaseploto];
(*spectrum intencity including phase*)
Tstep = 2 * Pi / ((ω2 - ω1) * add * (n - 1)); (*define time step*)
tim = Array[# * Tstep &, n] - Tstep * n / 2; (*ListPlot[tim]*)

junko = PadRight[compo, n]; (*add zero to rightside of data reaching n intotal*)
tampo = InverseFourier[junko];
i = Position[Abs[tampo], Max[Abs[tampo]]];
(*find peak E-field for moving to middle*)
tamp1o = RotateRight[tampo, Round[n / 2] - i[[1]]]; (*moving to middle*)
tamp2o = tamp1o / Max[Abs[tampo]]; (*normalize to 1*)

compe = Abs[Sqrt[Specplot]] * Exp[I * phaseplote];
(*spectrum intencity including phase*)
Tstep = 2 * Pi / ((ω2 - ω1) * add * (n - 1)); (*define time step*)
tim = Array[# * Tstep &, n] - Tstep * n / 2; (*ListPlot[tim]*)

junke = PadRight[compe, n]; (*add zero to rightside of data reaching n intotal*)
tampe = InverseFourier[junke];

tamp1e = RotateRight[tampe, Round[n / 2] - i[[1]]]; (*moving to middle*)
tamp2e = tamp1e / Max[Abs[tampe]]; (*normalize to 1*)

dat = ListPlot[Table[{tim[[i]] / fs, Re[tamp2o[[i]]]}, {i, n}],
   PlotRange → {{-Time, Time}, All}, Frame → True, Axes → False, Joined → True]

ListPlot[{Table[{tim[[i]] / fs, Abs[tamp2o[[i]]]^2}, {i, n}],
   Table[{tim[[i]] / fs, Re[tamp2o[[i]]]}, {i, n}]},
  PlotRange → {{-Time, Time}, All}, Frame → True, Axes → False, Joined → True]
```

```
dat = ListPlot[Table[{tim[[i]] / fs, Re[tamp2e[[i]]]}, {i, n}],
  PlotRange → {{-Time, Time}, All}, Frame → True, Axes → False, Joined → True]

ListPlot[{Table[{tim[[i]] / fs, Abs[tamp2e[[i]]]^2}, {i, n}],
  Table[{tim[[i]] / fs, Re[tamp2e[[i]]]}, {i, n}]},
 PlotRange → {{-Time, Time}, All}, Frame → True, Axes → False, Joined → True]

ListPlot[{Table[{tim[[i]] / fs, Re[tamp2e[[i]]]}, {i, n}],
  Table[{tim[[i]] / fs, Re[tamp2o[[i]]]}, {i, n}]},
 PlotRange → {{-Time, Time}, All}, Frame → True, Axes → False, Joined → True]

(*ListPlot[{Table[{tim[[i]]/fs,Sqrt[Abs[tamp2[[i]]]^2]},{i,n}],
  Table[{tim[[i]]/fs,-Sqrt[Abs[tamp2[[i]]]^2]},{i,n}],
  Table[{tim[[i]]/fs,Re[tamp2[[i]]]},{i,n}]},
 PlotRange→{{-Time,Time},All},Frame→True,Axes→False,Joined→True] *)

Export[$root <> "pulse1.dat", Table[{tim[[i]] / fs, Abs[tamp2o[[i]]]^2}, {i, n}]]
Export[$root <> "pulse2.dat", Table[{tim[[i]] / fs, Re[tamp2o[[i]]]}, {i, n}]]
```


Out[11]=

Out[28]=

91

Out[29]=

Out[30]=

Out[31]=

Out[32]=
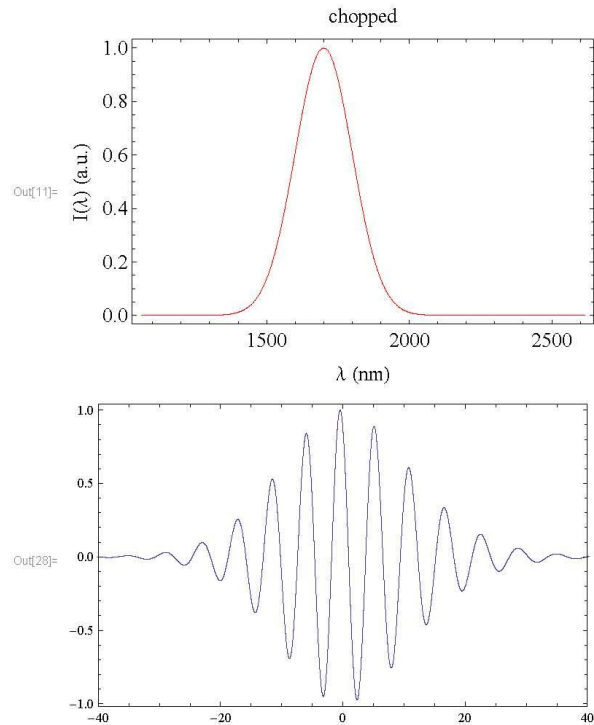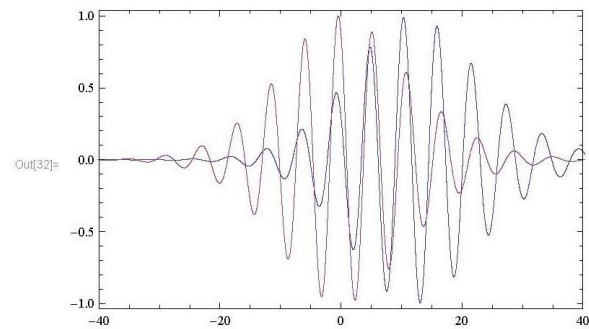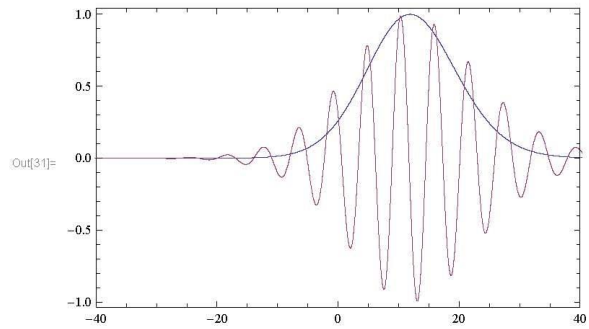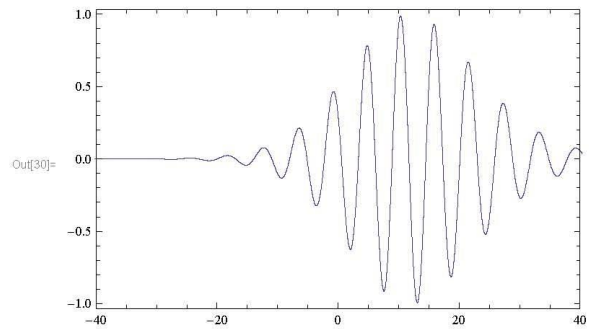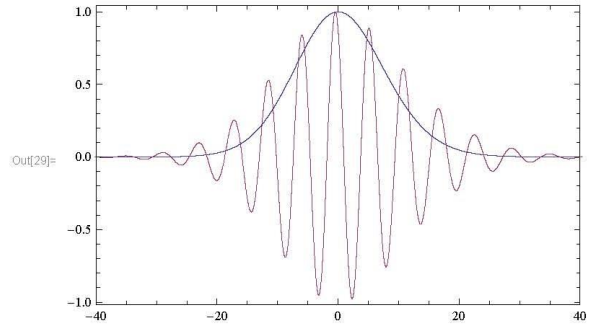

```
C:\Users\PP\Dropbox\Reasearch
  work\DFG&OPA birefringence\polarization gating\pulse1.dat

C:\Users\PP\Dropbox\Reasearch
  work\DFG&OPA birefringence\polarization gating\pulse2.dat
```

APPENDIX B- CODE FOR CALCULATE NONCOLLINEAR PHASE

MATCH IN BIBO CRYSTAL

```
(*follow the convention λ1(idler 1600)>λ2(signal 1600)>λ3(pump 800) *)
(*even the signal and idler wavelength is colse to degeneracy
 we still call the DFG λ2 signal *)
(*in our case: BIBO: signal θ=11 φ=0 L=5mm thickness;
the inside noncolinear angle is α(pump from signal),idler title angle is Ω with signal*)
(*angle phase match is only for pump beam, phase match angle is β *)
β = (10.88/180)*Pi;
α = (-0.5/180)*Pi;
SIN = Sin[α];
COS = Cos[α];
θ = β - α;
L = 0.005;


nx[λ_] := Sqrt[3.07403 + 0.03231/(λ^2 - 0.03163) - 0.013376*λ^2]
ny[λ_] := Sqrt[3.16940 + 0.03717/(λ^2 - 0.03483) - 0.01827*λ^2]
nz[λ_] := Sqrt[3.6545 + 0.05112/(λ^2 - 0.03713) - 0.02261*λ^2]
(*define idler wavelength for energy conservation*)
λ1[λ3_, λ2_] := (λ2*λ3)/(λ2 - λ3)
(*define effective refractive index for pump at β=θ+α*)
neff[λ_] := Sqrt[(nx[λ]^2*nz[λ]^2)/(Sin[β]^2*nx[λ]^2 + Cos[β]^2*nz[λ]^2)];
(* Plot[{{nx[λ]},{ny[λ]},{nz[λ]},{neff[λ]}},{λ,0.2,2},PlotRange→{1.7,2}] *)
nIdler[λ3_, λ2_] := ny[λ1[λ3, λ2]];
(*use idler wavelength λ1[λ3,λ2] to calculate refractive index of idler: nIdler.
    nIdler is now a function as nIdler[λ3,λ2] *)
(*ContourPlot[nIdler[λ3,λ2],{λ3,0.5,0.9},{λ2,1.4,2},
 Contours→25,ClippingStyle→Automatic,PlotRange→Automatic]*)
(*ContourPlot[λ1[λ3,λ2],{λ3,0.5,0.9},{λ2,1.4,2},Contours→25,
 ClippingStyle→Automatic,PlotRange→Automatic]*)
Δk[λ3_, λ2_] := 2000000 Pi*((COS*neff[λ3]/λ3 - ny[λ2]/λ2)*
        (1 - (1/Sqrt[(neff[λ3]/λ3)^2 + (ny[λ2]/λ2)^2 - 2*(neff[λ3]/λ3)*(ny[λ2]/λ2)*COS]*
            nIdler[λ3, λ2]/λ1[λ3, λ2]));
(*ContourPlot[Abs[(2/Pi)*L*Δk[λ3,λ2]],{λ3,0.7,0.9},{λ2,1.4,2},Contours→50,
 ClippingStyle→Automatic,PlotRange→Automatic]*)


OPAintensity[λ3_, λ2_] := (Sinc[0.5*L*Δk[λ3, λ2]])^2;
dplot1 = DensityPlot[If[λ3 == .7, 1, OPAintensity[λ3, λ2]], {λ3, 0.7, 0.9}, {λ2, 1.1, 2.5},
    PlotPoints → 50, ColorFunction → "Rainbow", ClippingStyle → Automatic, PlotRange → {0, 1}];
(*dplot1*)
(*ContourPlot[Abs[(2/Pi)*L*Δk[λ3,λ2]],{λ3,0.7,0.9},
 {λ2,1.4,2},Contours→50,ClippingStyle→Automatic,PlotRange→Automatic]*)


pp2[λ3_] := Table[λ3 == nm, {nm, 0.75, 0.82, 0.07}];
cplot1 = ContourPlot[Evaluate[pp2[λ3]], {λ3, 0.7, 0.9}, {λ2, 1.1, 2.5},
    Contours → 10, ContourStyle → Black, ClippingStyle → Automatic, PlotRange → Automatic];
(*cplot1*)


Show[{dplot1, cplot1}]
```
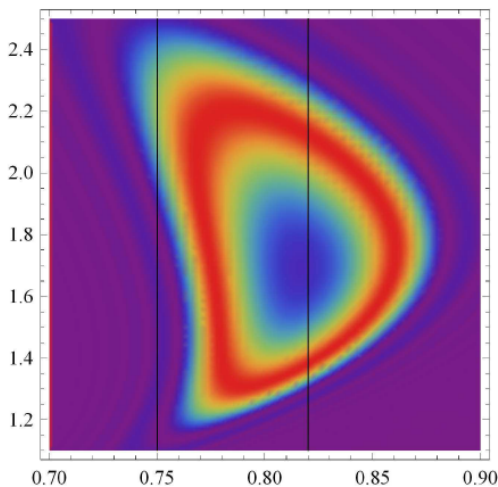
APPENDIX C- COPYRIGHT PERMISSION

**NATURE PUBLISHING GROUP LICENSE
TERMS AND CONDITIONS**

Oct 03, 2017

This Agreement between Jie Li ("You") and Nature Publishing Group ("Nature Publishing Group") consists of your license details and the terms and conditions provided by Nature Publishing Group and Copyright Clearance Center.

License Number	4201540549430
License date	Oct 03, 2017
Licensed Content Publisher	Nature Publishing Group
Licensed Content Publication	Nature Photonics
Licensed Content Title	The generation, characterization and applications of broadband isolated attosecond pulses
Licensed Content Author	Michael Chini, Kun Zhao, Zenghu Chang
Licensed Content Date	Feb 28, 2014
Licensed Content Volume	8
Licensed Content Issue	3
Type of Use	reuse in a dissertation / thesis
Requestor type	academic/educational
Format	electronic
Portion	figures/tables/illustrations
Number of figures/tables/illustrations	1
High-res required	no
Figures	figure 1
Author of this NPG article	no
Your reference number	
Title of your thesis / dissertation	GENERATION AND CHARACTERIZATION OF ISOLATED ATTOSECOND PULSE IN THE SOFT X-RAY REGIME
Expected completion date	Jan 2018
Estimated size (number of pages)	100
Requestor Location	Jie Li 4000 central Florida Blvd CREOL, UCF ORLANDO, FL 32816 United States Attn: Jie Li
Billing Type	Invoice
Billing Address	Jie Li 4000 central Florida Blvd CREOL, UCF ORLANDO, FL 32816

96

American Physical Society
Reuse and Permissions License
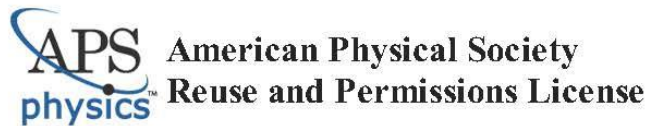
22-Mar-2018

This license agreement between the American Physical Society ("APS") and Jie Li ("You") consists of your license details and the terms and conditions provided by the American Physical Society and SciPris.

Licensed Content Information

License Number:	RNP/18/MAR/002517
License date:	22-Mar-2018
DOI:	10.1103/PhysRevA.65.011804
Title:	Dramatic extension of the high-order harmonic cutoff by using a long-wavelength driving field
Author:	Bing Shan and Zenghu Chang
Publication:	Physical Review A
Publisher:	American Physical Society
Cost:	USD $ 0.00

Request Details

Does your reuse require significant modifications: No

Specify intended distribution locations:	United States
Reuse Category:	Reuse in a thesis/dissertation
Requestor Type:	Academic Institution
Items for Reuse:	Figures/Tables
Number of Figure/Tables:	1
Figure/Tables Details:	figure 5
Format for Reuse:	Electronic

Information about New Publication:

University/Publisher:	UCF
Title of dissertation/thesis:	GENERATION AND CHARACTERIZATION OF ISOLATED ATTOSECOND PULSE IN THE SOFT X-RAY REGIME
Author(s):	Jie Li
Expected completion date:	Jun. 2018

License Requestor Information

Name:	Jie Li
Affiliation:	Individual
Email Id:	lijie430@knights.ucf.edu
Country:	United States

This Agreement between Jie Li ("You") and Springer Nature ("Springer Nature") consists of your license details and the terms and conditions provided by Springer Nature and Copyright Clearance Center.

License Number	4314410273510
License date	Mar 22, 2018
Licensed Content Publisher	Springer Nature
Licensed Content Publication	Nature Photonics
Licensed Content Title	Photonic streaking of attosecond pulse trains
Licensed Content Author	Kyung Taec Kim, Chunmei Zhang, Thierry Ruchon, Jean-François Hergott, Thierry Auguste et al.
Licensed Content Date	Jul 7, 2013
Licensed Content Volume	7
Licensed Content Issue	8
Type of Use	Thesis/Dissertation
Requestor type	academic/university or research institute
Format	electronic
Portion	figures/tables/illustrations
Number of figures/tables/illustrations	1
High-res required	no
Will you be translating?	no
Circulation/distribution	<501
Author of this Springer Nature content	no
Title	GENERATION AND CHARACTERIZATION OF ISOLATED ATTOSECOND PULSE IN THE SOFT X-RAY REGIME
Instructor name	Zenghu Chang
Institution name	UCF Department of Physics
Expected presentation date	Jun 2018
Portions	Figures 1
Requestor Location	Jie Li 4000 central Florida Blvd CREOL, UCF ORLANDO, FL 32816 United States Attn: Jie Li
Billing Type	Invoice
Billing Address	Jie Li 4000 central Florida Blvd CREOL, UCF ORLANDO, FL 32816 United States Attn: Jie Li
Total	0.00 USD

Terms and Conditions

American Physical Society
Reuse and Permissions License

22-Mar-2018

This license agreement between the American Physical Society ("APS") and Jie Li ("You") consists of your license details and the terms and conditions provided by the American Physical Society and SciPris.

Licensed Content Information

License Number:	**RNP/18/MAR/002518**
License date:	22-Mar-2018
DOI:	10.1103/PhysRevLett.105.173901
Title:	Bright, Coherent, Ultrafast Soft X-Ray Harmonics Spanning the Water Window from a Tabletop Light Source
Author:	M.-C. Chen et al.
Publication:	Physical Review Letters
Publisher:	American Physical Society
Cost:	USD $ 0.00

Request Details

Does your reuse require significant modifications: No

Specify intended distribution locations:	United States
Reuse Category:	Reuse in a thesis/dissertation
Requestor Type:	Academic Institution
Items for Reuse:	Figures/Tables
Number of Figure/Tables:	1
Figure/Tables Details:	figure 1
Format for Reuse:	Electronic

Information about New Publication:

University/Publisher:	UCF
Title of dissertation/thesis:	GENERATION AND CHARACTERIZATION OF ISOLATED ATTOSECOND PULSE IN THE SOFT X-RAY REGIME
Author(s):	Jie Li
Expected completion date:	Jun. 2018

License Requestor Information

Name:	Jie Li
Affiliation:	Individual
Email Id:	lijie430@knights.ucf.edu
Country:	United States

REFERENCES

1.   Maiman, T.H., *Stimulated optical radiation in ruby.* nature, 1960. **187**(4736): p. 493-494.

2.   Maiman, T.H., R. Hoskins, I. d'Haenens, C.K. Asawa, and V. Evtuhov, *Stimulated optical emission in fluorescent solids. II. Spectroscopy and stimulated emission in ruby.* Physical Review, 1961. **123**(4): p. 1151.

3.   McClung, F. and R. Hellwarth, *Giant optical pulsations from ruby.* Applied Optics, 1962. **1**(101): p. 103-105.

4.   Lamb Jr, W.E., *Theory of an optical maser.* Physical Review, 1964. **134**(6A): p. A1429.

5.   Strickland, D. and G. Mourou, *Compression of amplified chirped optical pulses.* Optics communications, 1985. **55**(6): p. 447-449.

6.   Nuernberger, P., G. Vogt, T. Brixner, and G. Gerber, *Femtosecond quantum control of molecular dynamics in the condensed phase.* Physical Chemistry Chemical Physics, 2007. **9**(20): p. 2470-2497.

7.   Gessner, O., A. Lee, J.P. Shaffer, H. Reisler, S.V. Levchenko, A.I. Krylov, J.G. Underwood, H. Shi, A.L. East, and D. Wardlaw, *Femtosecond multidimensional imaging of a molecular dissociation.* Science, 2006. **311**(5758): p. 219-222.

8.   Seifert, F., V. Petrov, and M. Woerner, *Solid-state laser system for the generation of midinfrared femtosecond pulses tunable from 3.3 to 10 μm.* Optics letters, 1994. **19**(23): p. 2009-2011.

9.   ZEWAIL, A., *Laser femtochemistry.* Science, 1988. **242**(4886): p. 1645-1653.

10.   Paul, P.M., E. Toma, P. Breger, G. Mullot, F. Augé, P. Balcou, H. Muller, and P. Agostini, *Observation of a train of attosecond pulses from high harmonic generation.* Science, 2001. **292**(5522): p. 1689-1692.

11.   Corkum, P.B., *Plasma perspective on strong field multiphoton ionization.* Physical Review Letters, 1993. **71**(13): p. 1994.

12.   Maine, P., D. Strickland, P. Bado, M. Pessot, and G. Mourou, *Generation of ultrahigh peak power pulses by chirped pulse amplification.* IEEE Journal of Quantum electronics, 1988. **24**(2): p. 398-403.

13. Goulielmakis, E., M. Schultze, M. Hofstetter, V.S. Yakovlev, J. Gagnon, M. Uiberacker, A.L. Aquila, E. Gullikson, D.T. Attwood, and R. Kienberger, *Single-cycle nonlinear optics.* Science, 2008. **320**(5883): p. 1614-1617.

14. Sansone, G., E. Benedetti, F. Calegari, C. Vozzi, L. Avaldi, R. Flammini, L. Poletto, P. Villoresi, C. Altucci, and R. Velotta, *Isolated single-cycle attosecond pulses.* Science, 2006. **314**(5798): p. 443-446.

15. Mashiko, H., S. Gilbertson, C. Li, S.D. Khan, M.M. Shakya, E. Moon, and Z. Chang, *Double optical gating of high-order harmonic generation with carrier-envelope phase stabilized lasers.* Physical review letters, 2008. **100**(10): p. 103906.

16. Chang, Z., *Controlling attosecond pulse generation with a double optical gating.* Physical Review A, 2007. **76**(5): p. 051403.

17. Gilbertson, S., H. Mashiko, C. Li, S.D. Khan, M.M. Shakya, E. Moon, and Z. Chang, *A low-loss, robust setup for double optical gating of high harmonic generation.* Applied Physics Letters, 2008. **92**(7): p. 071109.

18. Kim, K.T., C. Zhang, T. Ruchon, J.-F. Hergott, T. Auguste, D. Villeneuve, P. Corkum, and F. Quéré, *Photonic streaking of attosecond pulse trains.* Nature Photonics, 2013. **7**(8): p. 651-656.

19. Zhao, K., Q. Zhang, M. Chini, Y. Wu, X. Wang, and Z. Chang, *Tailoring a 67 attosecond pulse through advantageous phase-mismatch.* Optics letters, 2012. **37**(18): p. 3891-3893.

20. McPherson, A., G. Gibson, H. Jara, U. Johann, T.S. Luk, I. McIntyre, K. Boyer, and C.K. Rhodes, *Studies of multiphoton production of vacuum-ultraviolet radiation in the rare gases.* JOSA B, 1987. **4**(4): p. 595-601.

21. Ferray, M., A. L'Huillier, X. Li, L. Lompre, G. Mainfray, and C. Manus, *Multiple-harmonic conversion of 1064 nm radiation in rare gases.* Journal of Physics B: Atomic, Molecular and Optical Physics, 1988. **21**(3): p. L31.

22. Keldysh, L., *Ionization in the field of a strong electromagnetic wave.* Sov. Phys. JETP, 1965. **20**(5): p. 1307-1314.

23. Bellini, M., C. Lyngå, A. Tozzi, M. Gaarde, T. Hänsch, A. L'Huillier, and C.-G. Wahlström, *Temporal coherence of ultrashort high-order harmonic pulses.* Physical Review Letters, 1998. **81**(2): p. 297.

24.   Gaarde, M.B., F. Salin, E. Constant, P. Balcou, K. Schafer, K. Kulander, and A. L'Huillier, *Spatiotemporal separation of high harmonic radiation into two quantum path components.* Physical Review A, 1999. **59**(2): p. 1367.

25.   Doumy, G., J. Wheeler, C. Roedig, R. Chirla, P. Agostini, and L. DiMauro, *Attosecond synchronization of high-order harmonics from midinfrared drivers.* Physical review letters, 2009. **102**(9): p. 093002.

26.   Kim, K.T., C.M. Kim, M.-G. Baik, G. Umesh, and C.H. Nam, *Single sub− 50− attosecond pulse generation from chirp-compensated harmonic radiation using material dispersion.* Physical Review A, 2004. **69**(5): p. 051805.

27.   Hassan, M.T., T.T. Luu, A. Moulet, O. Raskazovskaya, P. Zhokhov, M. Garg, N. Karpowicz, A. Zheltikov, V. Pervak, and F. Krausz, *Optical attosecond pulses and tracking the nonlinear response of bound electrons.* Nature, 2016. **530**(7588): p. 66.

28.   Jullien, A., T. Pfeifer, M.J. Abel, P. Nagel, M. Bell, D.M. Neumark, and S.R. Leone, *Ionization phase-match gating for wavelength-tunable isolated attosecond pulse generation.* Applied Physics B: Lasers and Optics, 2008. **93**(2): p. 433-442.

29.   Chini, M., K. Zhao, and Z. Chang, *The generation, characterization and applications of broadband isolated attosecond pulses.* Nature Photonics, 2014. **8**(3): p. 178-186.

30.   Corkum, P., N. Burnett, and M.Y. Ivanov, *Subfemtosecond pulses.* Optics letters, 1994. **19**(22): p. 1870-1872.

31.   Ivanov, M., P. Corkum, T. Zuo, and A. Bandrauk, *Routes to control of intense-field atomic polarizability.* Physical review letters, 1995. **74**(15): p. 2933.

32.   Chang, Z., *Single attosecond pulse and xuv supercontinuum in the high-order harmonic plateau.* Physical Review A, 2004. **70**(4): p. 043802.

33.   Chang, Z., *Chirp of the single attosecond pulse generated by a polarization gating.* Physical Review A, 2005. **71**(2): p. 023813.

34.   Oron, D., Y. Silberberg, N. Dudovich, and D.M. Villeneuve, *Efficient polarization gating of high-order harmonic generation by polarization-shaped ultrashort pulses.* Physical Review A, 2005. **72**(6): p. 063816.

35.   Sola, I., E. Mével, L. Elouga, E. Constant, V. Strelkov, L. Poletto, P. Villoresi, E. Benedetti, J.-P. Caumes, and S. Stagira, *Controlling attosecond electron dynamics by phase-stabilized polarization gating.* Nature physics, 2006. **2**(5): p. 319.

36. Tcherbakoff, O., E. Mével, D. Descamps, J. Plumridge, and E. Constant, *Time-gated high-order harmonic generation.* Physical Review A, 2003. **68**(4): p. 043804.

37. Li, J., X. Ren, Y. Yin, Y. Cheng, E. Cunningham, Y. Wu, and Z. Chang, *Polarization gating of high harmonic generation in the water window.* Applied Physics Letters, 2016. **108**(23): p. 231102.

38. Ivanov, M.Y., M. Spanner, and O. Smirnova, *Anatomy of strong field ionization.* Journal of Modern Optics, 2005. **52**(2-3): p. 165-184.

39. Shan, B., S. Ghimire, and Z. Chang, *Generation of the attosecond extreme ultraviolet supercontinuum by a polarization gating.* Journal of modern optics, 2005. **52**(2-3): p. 277-283.

40. Möller, M., Y. Cheng, S.D. Khan, B. Zhao, K. Zhao, M. Chini, G.G. Paulus, and Z. Chang, *Dependence of high-order-harmonic-generation yield on driving-laser ellipticity.* Physical Review A, 2012. **86**(1): p. 011401.

41. Chang, Z., A. Rundquist, H. Wang, M.M. Murnane, and H.C. Kapteyn, *Generation of coherent soft X rays at 2.7 nm using high harmonics.* Physical Review Letters, 1997. **79**(16): p. 2967.

42. Rundquist, A., C.G. Durfee, Z. Chang, C. Herne, S. Backus, M.M. Murnane, and H.C. Kapteyn, *Phase-matched generation of coherent soft X-rays.* Science, 1998. **280**(5368): p. 1412-1415.

43. Popmintchev, T., M.-C. Chen, A. Bahabad, M. Gerrity, P. Sidorenko, O. Cohen, I.P. Christov, M.M. Murnane, and H.C. Kapteyn, *Phase matching of high harmonic generation in the soft and hard X-ray regions of the spectrum.* Proceedings of the National Academy of Sciences, 2009. **106**(26): p. 10516-10521.

44. Shan, B. and Z. Chang, *Dramatic extension of the high-order harmonic cutoff by using a long-wavelength driving field.* Physical Review A, 2001. **65**(1): p. 011804.

45. Chen, M.-C., P. Arpin, T. Popmintchev, M. Gerrity, B. Zhang, M. Seaberg, D. Popmintchev, M. Murnane, and H. Kapteyn, *Bright, coherent, ultrafast soft x-ray harmonics spanning the water window from a tabletop light source.* Physical Review Letters, 2010. **105**(17): p. 173901.

46. Franken, e.P., A.E. Hill, C.e. Peters, and G. Weinreich, *Generation of optical harmonics.* Physical Review Letters, 1961. **7**(4): p. 118.

47.   Boyd, R.W., *Nonlinear optics*. 2003: Academic press.

48.   Petrov, V., M. Ghotbi, O. Kokabee, A. Esteban‑Martin, F. Noack, A. Gaydardzhiev, I. Nikolov, P. Tzankov, I. Buchvarov, and K. Miyata, *Femtosecond nonlinear frequency conversion based on BiB3O6.* Laser & Photonics Reviews, 2010. **4**(1): p. 53-98.

49.   Baltuška, A., T. Fuji, and T. Kobayashi, *Controlling the carrier-envelope phase of ultrashort light pulses with optical parametric amplifiers.* Physical review letters, 2002. **88**(13): p. 133901.

50.   Fuji, T., A. Apolonski, and F. Krausz, *Self-stabilization of carrier-envelope offset phase by use of difference-frequency generation.* Optics letters, 2004. **29**(6): p. 632-634.

51.   Tate, J., T. Auguste, H. Muller, P. Salieres, P. Agostini, and L. DiMauro, *Scaling of wave-packet dynamics in an intense midinfrared field.* Physical Review Letters, 2007. **98**(1): p. 013901.

52.   Ishii, N., K. Kitano, T. Kanai, S. Watanabe, and J. Itatani, *Carrier-envelope-phase-preserving, octave-spanning optical parametric amplification in the infrared based on BiB3O6 pumped by 800 nm femtosecond laser pulses.* Applied physics express, 2011. **4**(2): p. 022701.

53.   Cheriaux, G., B. Walker, L. Dimauro, P. Rousseau, F. Salin, and J. Chambaret, *Aberration-free stretcher design for ultrashort-pulse amplification.* Optics letters, 1996. **21**(6): p. 414-416.

54.   Du, D., C. Bogusch, C.T. Cotton, J. Squier, S. Kane, G. Korn, and G. Mourou, *Terawatt Ti: sapphire laser with a spherical reflective-optic pulse expander.* Optics letters, 1995. **20**(20): p. 2114-2116.

55.   Tournois, P., *Acousto-optic programmable dispersive filter for adaptive compensation of group delay time dispersion in laser systems.* Optics communications, 1997. **140**(4-6): p. 245-249.

56.   Verluise, F., V. Laude, Z. Cheng, C. Spielmann, and P. Tournois, *Amplitude and phase control of ultrashort pulses by use of an acousto-optic programmable dispersive filter: pulse compression and shaping.* Optics letters, 2000. **25**(8): p. 575-577.

57.   Yin, Y., J. Li, X. Ren, K. Zhao, Y. Wu, E. Cunningham, and Z. Chang, *High-efficiency optical parametric chirped-pulse amplifier in BiB 3 O 6 for generation of 3 mJ, two-cycle, carrier-envelope-phase-stable pulses at 1.7 μm.* Optics letters, 2016. **41**(6): p. 1142-1145.

58. Treacy, E., *Optical pulse compression with diffraction gratings.* IEEE Journal of quantum Electronics, 1969. **5**(9): p. 454-458.

59. Kane, D.J. and R. Trebino, *Characterization of arbitrary femtosecond pulses using frequency-resolved optical gating.* IEEE Journal of Quantum Electronics, 1993. **29**(2): p. 571-579.

60. Kane, D.J. and R. Trebino, *Single-shot measurement of the intensity and phase of an arbitrary ultrashort pulse by using frequency-resolved optical gating.* Optics letters, 1993. **18**(10): p. 823-825.

61. Itatani, J., F. Quéré, G.L. Yudin, M.Y. Ivanov, F. Krausz, and P.B. Corkum, *Attosecond streak camera.* Physical Review Letters, 2002. **88**(17): p. 173903.

62. Chini, M., S. Gilbertson, S.D. Khan, and Z. Chang, *Characterizing ultrabroadband attosecond lasers.* Optics express, 2010. **18**(12): p. 13006-13016.

63. Bradley, D., B. Liddy, and W. Sleat, *Direct linear measurement of ultrashort light pulses with a picosecond streak camera.* Optics Communications, 1971. **2**(8): p. 391-395.

64. Lewenstein, M., P. Balcou, M.Y. Ivanov, A. L'huillier, and P.B. Corkum, *Theory of high-harmonic generation by low-frequency laser fields.* Physical Review A, 1994. **49**(3): p. 2117.

65. Kitzler, M., N. Milosevic, A. Scrinzi, F. Krausz, and T. Brabec, *Quantum theory of attosecond XUV pulse measurement by laser dressed photoionization.* Physical review letters, 2002. **88**(17): p. 173904.

66. Mairesse, Y. and F. Quéré, *Frequency-resolved optical gating for complete reconstruction of attosecond bursts.* Physical Review A, 2005. **71**(1): p. 011401.

67. Gagnon, J., E. Goulielmakis, and V.S. Yakovlev, *The accurate FROG characterization of attosecond pulses from streaking measurements.* Applied Physics B: Lasers and Optics, 2008. **92**(1): p. 25-32.

68. Mairesse, Y., A. De Bohan, L. Frasinski, H. Merdji, L. Dinu, P. Monchicourt, P. Breger, M. Kovačev, R. Taïeb, and B. Carré, *Attosecond synchronization of high-harmonic soft x-rays.* Science, 2003. **302**(5650): p. 1540-1543.

69. Bizau, J. and F. Wuilleumier, *Redetermination of absolute partial photoionization cross sections of He and Ne atoms between 20 and 300 eV photon energy.* Journal of electron spectroscopy and related phenomena, 1995. **71**(3): p. 205-224.

70.   Zhang, Q., K. Zhao, and Z. Chang, *High resolution electron spectrometers for characterizing the contrast of isolated 25 as pulses.* Journal of Electron Spectroscopy and Related Phenomena, 2014. **195**: p. 48-54.

71.   Chini, M., H. Mashiko, H. Wang, S. Chen, C. Yun, S. Scott, S. Gilbertson, and Z. Chang, *Delay control in attosecond pump-probe experiments.* Optics express, 2009. **17**(24): p. 21459-21464.

72.   Gagnon, J. and V.S. Yakovlev, *The robustness of attosecond streaking measurements.* Optics express, 2009. **17**(20): p. 17678-17693.

73.   Wuilleumier, F. and M. Krause, *Photoionization of neon between 100 and 2000 eV: Single and multiple processes, angular distributions, and subshell cross sections.* Physical Review A, 1974. **10**(1): p. 242.

74.   Schultze, M., M. Fieß, N. Karpowicz, J. Gagnon, M. Korbman, M. Hofstetter, S. Neppl, A.L. Cavalieri, Y. Komninos, and T. Mercouris, *Delay in photoemission.* science, 2010. **328**(5986): p. 1658-1662.